MECHANICS OF FIRE ANT AGGREGATIONS: AN EXPERIMENTAL STUDY OF ACTIVE MATTER

A Dissertation
Presented to
The Academic Faculty

By

Michael J. Tennenbaum

In Partial Fulfillment
of the Requirements for the Degree
Doctor of Philosophy in the
School of Physics

Georgia Institute of Technology

August 2019

MECHANICS OF FIRE ANT AGGREGATIONS: AN EXPERIMENTAL STUDY OF ACTIVE MATTER

Approved by:

Dr. Alberto Fernández-Nieves, Advisor
School of Physics
Georgia Institute of Technology

Dr. Flavio Fenton
School of Physics
Georgia Institute of Technology

Dr. Guillermo Goldsztein
School of Mathematics
Georgia Institute of Technology

Dr. Harold Kim
School of Physics
Georgia Institute of Technology

Dr. Peter Yunker
School of Physics
Georgia Institute of Technology

Date Approved: June 11, 2019

Beim Menschen ist es wie beim Velo.

Nur wenn er faehrt, kann er bequem die Balance halten.

Albert Einstein

Life is like riding a bicycle.

To keep your balance you must keep moving.

Translation by Walter Isaacson

To the fire ants who gave their lives for science.

ACKNOWLEDGEMENTS

There are always a litany of people to thank for all of their help over the years. It is both a great thing that I am a product of their support and a funny thing that my memory is limited.

To my Advisor, Professor Alberto Fernandez-Nieves I am most grateful. Your dedication to weekly group meetings (sometimes more) fostered a community in the lab. This broadened my understanding of science and was excellent practice in using storytelling to better explain science. I appreciate your attention to detail and know that this dissertation and the research contained within have benefited greatly from it.

To my committee, Professor Peter Yunker, Professor Harold Kim, Professor Guillermo Goldztein, and Professor Flavio Fenton I am appreciative of your roles in the shaping of me as a scientist and product of Georgia Tech. Professor Yunker, Professor Kim, and Professor Fenton were valuable members of the Physics of Living Systems community, which was an integral part of my time at Georgia Tech. To Professor Kim, I enjoyed being your Teacher's Assistant for Statistical Mechancis, a class I enjoyed as a student, while auditing, and as a TA.

To my lab mates, Perry, Caleb, John, Alex, Jonas, Winnie, Josefa, and everyone else from the Soft Condensed Matter Lab. I know I learned a lot and enjoyed doing it in large part thanks to all of you.

To all of the research assistant students in their undergraduate and high school years who have worked with me in the lab: Tae, Zongyang, Lily, Xiaochen, Sruti, Pablo, Christian, and Nilai. I found that our time together helped me learn to talk about science more clearly. You also helped me see mentoring relationships from the other side. I hope you are all off doing great things.

To all of my funding sources, the School of Physics, the Center for Education Teaching and Learning, the National Science Foundation (PoLS and other grants), the Army Re-

search Laboratory, the Sam Nunn School of International Affairs, and the Center for the Science and Technology of Advanced Materials and Interfaces/ Soft Matter Institute. This would not have happened without your financial support. Thank you to Vicki for keeping it all organized. We always made it work somehow.

To the two main people and their organizations that helped broaden my thinking of the roles of science in society, I am deeply changed by our experiences together. I was a fellow in the Sam Nunn Security Program run by Professor Margret Kosal, where grad students in science and policy across Georgia Tech worked to see how our fields interact in a new light. I was also a teaching fellow in CETL's GoSTEM program run by Susan Belmonte where I practiced teaching physics and math in the local Maynard Jackson High School.

To all of the people who helped me take care of my physical and mental health while attending Georgia Tech. Thank you to Dr. Charles Fox, Yvette Cianfaglione, Dr. Mack Rachal, Lenice Metelo, PA Kimberly Orleck, and PA Stephen Terry. Working with biological systems is tough and I appreciate your efforts.

Science is not done in a vacuum. The completion of this project would not have been possible for me without the love and support of my friends and family. The School of Physics incoming class of 2012 was full of brilliant and kind people who made our first year not just possible but enjoyable, too. To Starter Bikes, the bicycle cooperative at Georgia Tech, thank you for providing me with solvable problems and giving me something to look forward to every Friday. To my parents, Iris Kotovsky Tennenbaum and Dan Tennenbaum, Ph.D., thank you for your consistent support over the many years it took to get me into and out of this graduate program. To my partner Charley, your support means more to me than you can know.

And to everyone else whom I have failed to remember: my apologies and thank you.

TABLE OF CONTENTS

LIST OF TABLES

LIST OF FIGURES

CHAPTER 1
INTRODUCTION AND BACKGROUND

Active matter is composed of collections of particles which are themselves out of equilibrium and are, in many cases, self propelled. The mechanics of active systems have only recently begun to be studied experimentally. Since energy is added at the individual particle level instead of to the whole system, the material response might be different. Statistical mechanics has over the past century or so developed theories to treat equilibrium systems, nonequilibrium systems, and active systems. However, up until recently, there have been very few experimental systems that were able to test these theories. Most experimental work in statistical mechanics so far has focused on systems in equilibrium. Systems that are out of thermal or mechanical equilibrium or both, display global properties not found in equilibrium systems. Similarly to how nonlinear science has been compared to "calling the bulk of zoology the study of non-elephants" [1], nonequilibrium systems are a much broader class than those in equilibrium. Here we will explore an active system experimentally.

To do that we first need to understand what sets active matter apart from inactive matter. All active matter is out of thermal equilibrium but not all thermally out of equilibrium systems are active. We also need to have an idea of the varied types of active matter and what are the similarities/ differences between them.

1.1 Thermal Equilibrium

Thermal equilibrium is defined by every part of the system having the same temperature, i.e. no heat flow. This temperature is related to the average kinetic energy of the particles that make up the system. Since this kinetic energy is nonzero for systems above absolute zero, the particles move. Their movement set the global mechanical and thermal properties

of the system [2, 3]. However, the temperature is based on the average kinetic energy, higher and lower local kinetic energies are possible. These locally different energies create fluctuations in position and in momentum which allows the system to relax.

A moving particle in a fluid feels a resistance from the fluid based on the collisions of the fluid particles with the particle. This is characterized by the viscosity of the fluid. Conversely, the collision of jiggling fluid particles with a larger particle in the fluid will cause the particle to undergo Brownian motion. The fluctuation-dissipation theorem links the viscosity of the fluid with the Brownian motion of a particle in the fluid. This is only true when detailed balance is obeyed. Fluids can have more than one microscopic state which has the same macroscopic properties. The states are called microstates. Detailed balance says that at equilibrium the transition rates of switching between microstates are equal and opposite [3]. One directional transitions are not allowed. At equilibrium, detailed balance is obeyed and the system is the same under time reversal, i.e. it looks the same forwards and backwards in time. This means that it is not possible for constituents to bunch up in one state due to fluctuations, i.e. fluctuations cannot change the average state of the system.

One way to prevent a system from being in thermal equilibrium is to attach the system to two heat baths at different temperatures. With one heat bath it is possible to reach thermal equilibrium with the bath but with two baths at different temperatures it is no longer possible. Heat will flow from the bath at a higher temperature through the system and into the lower temperature bath. Together the three parts of the system can reach a steady state with the higher temperature bath acting as a source, the lower temperature bath acting as a sink, and the system then acting to transfer energy between the two. This inability to reach equilibrium is captured by looking at the detailed balance of the system [4]. Detailed balance is broken in the two temperature bath example because there is flow of energy through the system from one bath to another which means that the transition rates between microstates are not equal because of the heat flow.

1.2 Mechanical Equilibrium

Systems that are out of mechanical equilibrium are not in the lowest mechanical energy state. Glasses, both polymer and colloidal, as well as athermal systems, like granular media, are all out of mechanical equilibrium. In these systems particles can be mechanically trapped leading to a breakdown of the equipartition theorem. These mechanical inhomogeneities lead to difficulties in defining a temperature. In these systems temperature can no longer be defined globally for the system though in some cases it can still be defined locally and it is still possible to measure a temperature empirically. The other possibility is athermal systems where temperature is well defined but not meaningful. In a pile of sand the mechanical properties are not dependent on the temperature of the individual sand particles. Gravitational energy is larger than thermal energy and so the particles do not move thermally. System out of mechanical equilibrium are usually blocked from reaching a lower energy state since the fluctuations due to temperature are not strong enough to rearrange the system.

1.2.1 Glasses

Glasses are a class of systems that are out of mechanical equilibrium. They are not ergodic and energy cannot be moved between different microstates because glasses are mechanically arrested. These are solids that do not have positional order as a crystal system would. They do not have the ability to rearrange like a liquid though and so even if there is a mechanical state with a more uniform distribution of energy it is not possible for the system to relax into it.

Glass forming systems come in several flavors including: molecular, polymer, and colloidal glass formers. All are characterized by a diverging relaxation timescale and the accompanying zero frequency solid behavior but the length scale of the constituents is very different and the parameter that controls the glass transition is different.

For molecular glass formers temperature is the key parameter needed to make a glass, in particular the rate of temperature decrease. As a molecular liquid is cooled its specific volume, inverse density, decreases. If the system is cooled slowly, i.e. there is plenty of time for rearrangement, and below a certain temperature the system will crystallize. If the system is cooled at a faster rate it avoids this transition and becomes first a supercooled liquid and then a glass. The exact temperature at which it becomes a glass depends on the rate of cooling [5]. This temperature where the system becomes a glass, T_g, is usually taken when the viscosity reaches a value of $10^{11}\ Pa \cdot s$ and corresponds to a relaxation time of $\approx 100\ s$ [6]. Another way of identifying the transition is by measuring the heat capacity of the system. This works because the heat capacity is discontinuous from molecular liquid to the glass. The discontinuity in the heat capacity is a hallmark of a second order phase transition.

For polymer glass formers one of the mechanisms that traps the polymers out of equilibrium is entanglements. At higher temperatures polymers jiggle enough to be able to slide past one another but as temperature is decreased the polymers are no longer able to move past each other and the length of the polymers prevents rearrangements. Rearrangements can also be prevented through crosslinking of the polymer chains. This creates a polymer network which is solid, however it does not create a glass as crosslinked systems are too dilute The crosslinks can shift a little but are not able to rearrange and so the network is stuck in whatever configuration it was in when it was crosslinked [7].

For colloidal glasses the important parameter is the volume fraction, rather than temperature. For colloids which interact only through hard sphere repulsion, changing temperature will change the overall jiggling of the particles but it will not cause or prevent the system from forming a glass. The volume fraction, ϕ, is the fraction of the system volume occupied by the colloids: $\phi = V_{colloids}/V_{system}$. Increasing volume fraction rapidly will cause the system to become a glass, changing it slowing allows for crystalization. For hard spheres spheres below $\phi = 0.494$ the colloids are a fluid and will be crystalline at

$\phi = 0.545$ if ϕ is changed slowly and the spheres are monodisperse [8, 9]. Crystallization can be avoided by either changing the volume fraction rapidly or by introducing a polydispersity of at least 10% [10, 11]. Polydispersity is a parameter that is not possible to change in atomic systems. If crystallization is avoided colloidal systems will supercool at $\phi = 0.494$ and then form a glass between $\phi \approx 0.58$ and random close pack, $\phi_{rcp} \approx 0.64$ [8].

The difference in positional order between a colloidal fluid or glass and a crystal can be seen in the pair distribution function, $g(r)$, of the system [6, 12] which is defined as:

$$g(r) = \frac{1}{\rho}\left\langle \sum_i \delta(r - r_i) \right\rangle. \tag{1.1}$$

ρ is the density of particles, r_i is the position of each particle, $\langle\rangle$ is the ensemble average. Since $\int_V \sum_i \delta(r - r_i) = N - 1$, $g(r)$ is dimensionless [12]. Essentially starting from a particle in the system, how many particles are a distance r away normalized by the overall density of the system and averaged over all particles. The pair correlation function measures the probability of finding another particle a distance r away. In crystals, $g(r)$ will have sharp peaks whose separation is related to the lattice spacing. In fluids, $g(r)$ has a nearest neighbor peak and maybe other peaks of decreasing height for larger r but quickly drops to 1. Glasses have pair correlation functions that are similar to fluids, reinforcing their lack of positional order.

To see the difference between a colloidal fluid and a glass we need to look at the dynamics of the colloids in the system. The root mean squared displacement is a measure of how far a colloid will move in certain amount of time on average. A single colloid in a fluid will experience Brownian motion, and as such, the slope of the mean squared displacement versus time for long times gives the diffusion coefficient of the particle. As the density is increased the mean squared displacement becomes sub diffusive and eventually flat as the particles become caged. Individual colloids become trapped or caged by their neighbors and can no longer move larger distances. One model for the glass transition, the Adams-

Gibbs model, says that it then takes more and more particles moving collectively for any of them to move [13]. Once the number of particles moving collectively reaches the system size, no particle can move and the system becomes a glass.

1.2.2 Granular Materials and Athermal Systems

Another way of making a system insensitive to temperature is to make the particles large enough that they cannot be moved around by thermal energy. Without a way to find mechanical equilibrium, the system can be stuck in a mechanical energy state that is not the lowest without a path to get to the lowest energy state. The system has no way of relaxing to a lower mechanical energy state without an external perturbation since thermal energy is not large enough to jiggle the particles into a lower mechanical energy state. For example a pile of sand is insensitive to temperature and is not stable because if you perturb the sand the system will rearrange and come to rest in a new configuration [14–17]. This is not to say that a sand pile will rearrange at the slightest perturbation, friction and hard core repulsion give elasticity to the system. These forces can be traced through the system by looking at the contact points between particles and the lines of force, or force chains, throughout the system. Particles feel forces from their neighbors and these chains can extend to the boundaries of the system. These chains are evidences by the sand pile holding its shape against gravity or through the clogging of a hopper.

One way of finding mechanical equilibrium in a granular system is to continuously perturb the system usually by shaking or pumping in a fluid [18]. Shaking a hopper containing a granular media will prevent the formation of force chains at the opening which would have lead to clogs [19]. Shaking also works to thermalize two dimensional granular systems. A single disk on a shaking plate undergoes Brownian motion where without the shaking it will simply sit in one spot [20]. Starting from the single shaken disk more disks can be added until there is a granular gas and then a liquid and then either a crystal or a glass depending on the boundary conditions and how the density is increased [21, 22],

similar to colloidal systems.

Fluidized systems are granular particles that have been suspended by an upwardly moving current of either air or water [18, 23]. In these systems the constituent particles are jostled around by the moving fluid. The jostling allows the granular particles to find a minimum mechanical energy state similar to the jiggling of colloidal particles by the surrounding fluid. It is possible to define a viscosity of the fluidized granular system [24, 25] and to see bubbles, spaces where there are not particles that propagate upwards through the system [26, 27]

Instead of forcing granular particles apart it is also possible to have them stick together. Cohesion is the ability to stick together and become a larger whole. Similar to how polymers can become entangled, granular system become cohesive through entanglement. This is done by changing the shape of the particles to be u shaped, like a staple, for example. This is a geometric effect of the particles themselves, spheres will not entangle as their shape is uniform, staples or other u shapes will entangle if the density is high enough [17, 28, 29]. A collection of staples poured into a tube will hold its shape after the tube is removed [28]. When shaken the column collapses and the time of collapse decreases with increasing acceleration of the shaker, analogous to higher temperature.

1.2.3 Active Matter

Active matter is another type of nonequilibrium system which is characterized by continuous energy input to the system at the particle level. This breaks detailed balance because there is a microscopic energy source. This energy input at the particle level be realized by biology (cell aggregations, dense animal collectives) or by design (colloids, robots, shaken granular systems). In 3D systems the energy source cannot be global but in a 2D system the energy source can be global as long as it does not affect the particle's direction. This can be done by something in the third dimension, like shaking or electric or magnetic fields [30–34] as long as the constituents each have their own direction that is not affected

by the external force. For 3D systems this energy has to be internal to the particles (e.g. biological systems) or generated at the particle level (e.g. active colloidal systems). This means that a shaken granular system in 2D can be active as the particles can be made to have an individual preferred direction but that fluidized 3D granular systems are not active.

Another important aspect of active matter is directionality. Active particles need to have an individual preferred direction to their motion. Not having a preferred direction leads to Brownian motion. For biological systems this is simple as organisms move in a direction that is either internally decided with the potential for input from their neighbors. Colloids can be made into Janus particles which do not have the same surface characteristics in different locations. Shaken granular systems in 2D can be made nonuniform so that each particle has its one preferred direction.

Because we are looking at similarities between systems as diverse as colloids, cells, robots, and ants, and treating them all as active matter, commonalities between them can then be of relevance to all of these larger fields. Active matter can be used to infer: the properties necessary to make self healing materials [35–38], the mechanics of robotic swarms [39–41], and the mechanics of biological systems from cells to humans [42–48]. It is also of interest from the physics perspective as active systems are inherently out of equilibrium. Collective motion has been studied by biologists for a long time but it is only relatively recently that it has been taken up by physics starting with theorists [49, 50]. New experiments allow us to test these theories and to propose new avenue of work.

1.3 Overview of the Current State of Active Matter

Active matter encompasses a large class of systems. Within experimental active matter one possible division that can be made is between synthetic and biological systems. Synthetic active matter covers self propelled colloids [32, 33, 51–54], robots [55], vibrated granular systems [56], and active liquid crystalline materials [57], while biological active matter covers cells [45, 58–60] up to organismal level biological systems [48, 61–68]. There are

several important features of active matter that will help classify systems, source of energy, interaction range, strength, and type, and density.

Density is characterized by the volume fraction, ϕ. The volume fraction is the ratio between the amount of space taken up in a system by the things of interest and the system size itself: $\phi = V_{Interest}/V$, where V is the system volume and $V_{Interest}$ is the volume of the thing being examined. This can be calculated by summing over the volume of each particle in the system $\phi = \frac{1}{V}\sum_{i=1}^{N} V_i$, where N is the number of particles, each with volume V_i. For monodisperse particles $\phi = N \times V_{particle}/V$, with $V_{particle}$ the volume of one particle.

The interaction range determines the distance over which interparticle forces play a role. Particles need to be close enough to one another to be able to feel effects from each other. This can be as short as the particle diameter for systems that only interact though hard core repulsion. The interaction range can also be larger if there are other forces acting between the particles, either repulsive or attractive forces.

The source of energy can either be internal to the particles as in biological samples which convert stored chemical energy into some form of work or can be generated externally for synthetic samples. External generation can be done with changing electric or magnetic fields, catalysts, or by shaking. The particles themselves have to be made anisotropic in some way so that the external generation has a preferential direction. This preferential direction for the force acts as a self propulsion, since each particle moves at a similar speed but in its own direction.

One other important feature to look for is self-organization and collective motion. These only happens above a certain density as the interaction range and the interparticle distance become comparable. Collective motion is common in biological systems; it happens for example in flocks of birds, schools of fish, swarms of insects, and cell aggregations. Collective motion in flocks, schools, and swarms all include "coherent motion of large numbers of self-propelled 'particles' " [69]. Aggregations are the same but with a cohesive element, since individual 'particles' can adhere one onto another. This can occur

in cellular and insect collectives.

1.4 Modeling and Simulation of Active Matter

1.4.1 Modeling of Active Matter

There are two main approaches to modeling active matter: particle-based models and continuum models. The main particle based model is the Vicsek model which considers individual particles separately and from the individual builds up to collective motion [50, 70]. The main continuum model is the Toner-Tu model which captures similar collective behavior but comes at it from a continuum viewpoint [61]. There are also hydrodynamic models that have been proposed to include interactions based through a surrounding fluid [71, 72].

The Vicsek model considers a collection of self-propelled particles that move with a constant speed but that tend to align with the average direction of motion of the particles close to them. The orientation of the particles is based on the particles within a distance $r_{interaction}$ of it and a noise term. For small $r_{interaction}$ or large noise there is no alignment and the particles behave similar to a gas. For larger $r_{interaction}$ and small noise there are transitions from a gas-like state to a liquid-like state and from a liquid to a a swarming state [50]. Having high alignment promotes flocking at lower densities than would be seen otherwise since the particles tend to group together. This is similar to how bird flocks or herds of animals form and stay together even when the space available is much larger than the flock.

This model is similar in spirit to the two dimensional XY-model first proposed by Kosterlitz and Thouless in 1973 [73]. The XY-model consists of interacting spins on a lattice in 2D. At zero temperature the spins are all aligned. However, the standard XY-model cannot have long range order at nonzero temperature, the fluctuations and noise forbid it. In contrast, the Vicsek model does show long range order at nonzero temperature; the difference being nonequilibrium processes, active motion and alignment. The Vicsek model explicitly does not conserve momentum or energy. The self propulsion prevents

energy conservation and the alignment interaction prevents momentum conservation. In this context, flocking represents a nonequilibrium phase transition into a dense correlated phase.

This transition is also captured by the Toner-Tu model which is a continuum model of a similar system to the Vicsek model [49, 61]. This model does not deal with individual particles but instead treats the whole system as a continuum that has properties like degree of alignment, local velocity, and density. It treats the density and the velocity as continuous variables. These properties evolve in time and as such the distribution of densities, velocities, and orientations can be studied in time. Because these properties are treated as continuous variables, hydrodynamic theories can be used to treat the dynamics of the variables. [71]. This hydrodynamic description leads to long range interactions.

Discrete and continuum models of active particles have expanded to include a wider range of interactions like soft interactions and longer range interactions [74, 75]. This area is also being explored through simulation of active particles. One way of generating collective motion is to have short range repulsion and long range attraction [76]. This groups the constituents together but also keeps them from getting too close and preventing others from moving.

There has also been work done trying to expand the understanding of equilibrium systems to nonequilibrium systems by looking for state variables in active matter. State variables, such as temperature and pressure, are familiar in thermodynamics. The knowledge of state variables provides complete macroscopic knowledge of the system, without any reference to its history. For example the pressure of an ideal gas is dependent on the temperature and the density of particles but does not depend on the individual trajectories of the particles themselves [3].

Currently there is disagreement over whether there are or can even be defined state variables for active systems. There are arguments that quantities like pressure can be found from the level of activity of the particles [77–80] and others say it cannot [81] or that it can

only be the case at low volume fractions [82]. So far there is far more theoretical work tan experimental work.

1.4.2 Simulation of Active Matter

Simulation allows for tuning parameters like activity level (e.g. self-propulsion), density, attraction/repulsion, and alignment, both strength and distance of interaction, over a wide range of parameters systematically. Most simulations follow the same scheme as Molecular dynamics simulations [83]. At each time step the forces between particles are calculated, the velocities updated, and then the positions updated. This repeats for however long the simulation is run. This can be done with friction, so that there is damping in the system. Some are even done with a viscous fluid surrounding the particles to increase the damping or add hydrodynamic interactions [84].

Typically the level of activity is defined by the level of self propulsion. This is sometimes quantified via a Péclet number [85], the ratio of the time it takes to move the particle diameter based on its self-propulsion to the time it takes to diffuse the same distance. The response of the system to changes in the level of activity can be observed in both two and three dimensions [85–90].

For so called active Brownian particles there is a set speed (activity) at each time step but the orientation of the particle is Brownian [87–89]. The orientation of active Brownian particles changes at each time step by letting the orientation diffuse. For small rotational diffusion, particles travel mostly in straight lines while for the highest rotational diffusion the particles recover Brownian motion. At high enough density active Brownian particles cluster even in the absence of cohesion between the particles [85, 86, 91–93]. This is due to the difference in rates of particles leaving the cluster and entering the cluster. For a particle to enter the cluster it has to be pointed at the cluster and run into it, this is proportional to the density of free particles and the speed of the particles. For it to then leave the cluster it has to rotationally diffuse around far enough to be able to escape. As density increases

the likelihood of entering a cluster becomes larger than of leaving and the system phase separates. Once clusters form, the system phase separates with a dense cluster of particles and a low density region of more motile particles outside the cluster. Phase separation does not change the velocity that the particles want to move at but it does change local density and therefore the space available to them, thus affecting the resultant motion of the particles in the cluster.

Another type of particles are called run and tumble particles [94]. These particles move in a straight line for a certain time (run) and then undergo a random reorientation (tumble) before setting off in the new direction. Long run times gives ballistic like motion and really short run time again recovers Brownian motion.

Particles can also be made attractive [85] or can have alignment rules added [95]. Cohesion causes clustering to happens at lower densities, and it changes both the density of the cluster and the lifetime of the cluster [85, 86, 96]. Clusters that form from activity but without cohesion have a lower volume fraction and more volatile edges.

Another parameter that is possible to tune in simulation is the degree of Vicsek-like alignment between particles locally [97]. In this way *in silico* flocks can be observed as a function of the level of alignment. Simulations focused on alignment use less dense systems since alignment based flocking transitions occur at lower overall densities.

It is also possible to make bigger particles out of many smaller active particles confined within a boundary [98]. This internal control of the particle allows for a variety of cell-like behaviors from the big particles. Changing the boundary conditions changes how the internal active particles move which changes how the larger particle moves.

1.5 Synthetic Active Matter

There are different types of synthetic active matter from colloids to robots. They differ by energy source and size and can exist at a range of volume fractions. Active colloidal systems have the largest range of interparticle forces but are usually dilute so the forces

have less of an effect.

1.5.1 Colloids

There are many different ways of inducing activity in colloidal particles [99]. All of them require particles with anisotropic interactions, so as to provide a force imbalance. This also sets a preferential direction of motion for each individual particle. Methods for inducing activity include changing electric and magnetic fields [32, 33, 54, 100, 101], self diffusiophoresis [52, 53], and bubble generation [102]. 3D active suspensions are usually at dilute volume fraction because of current limitations in providing activity. However, it is possible to create dense colloidal systems in 2D [34, 100, 103]. A table of current types of synthetic active matter is shown in Tab. 1.1.

Activating colloids using electric and magnetic fields works by creating a potential difference across the particle. This can be done by using Janus particles with a core of one material and then coating half the particle in another material. For example, coating polystyrene latex spheres on one side with gold which is conductive causes the particles to move away from the gold side in the presence of an AC electric field [54], Fig. 1.1 (a). The electric field is perpendicular to the motion of the particle and the particles move via induced-charge electrophoresis. The greater amount of charge on the gold side leads to the fluid movement on that side larger than the polystyrene side which causes a pressure imbalance and motion away from the gold coated side of the particle. Since the electric field does not bias the particle to a certain direction as long as it stays in a plane perpendicular to the field, this technique could be used to generate dense 2D active colloidal systems.

Self diffusiophoresis again uses Janus particles but instead of having a conductor on one half and a dielectric on the other, it uses a catalyst on one half or different catalysts on both. One such system is made from coating polystyrene spheres on one side with platinum. The platinum is a catalyst for the chemical reaction of hydrogen peroxide becoming water and oxygen. The oxygen bubbles that form from this reaction only happen on the

platinum side which causes a local osmotic pressure difference which in turn causes The particle to move away from the platinum side [52], Fig. 1.1 (b). This particular system was used to demonstrate that this active system can be steered by boundary effects [104]. Hydrodynamic interactions with a wall can trap the particles near the wall leading to directed motion of the particles. It has also been used to look at the sedimentation of active particles [105]. Brownian particles show a gradient in density that is due to gravity and the temperature. Repeating this experiment with an active system allows for measurement of an effective temperature which could be used to compare the active system to the passive one.

A similar system was made by Paxton et al. using bimetallic rods, again using the conversion of hydrogen peroxide to water and oxygen as the fuel. However, in this system the platinum side converts the hydrogen peroxide to hydrogen and oxygen and electrons while the gold side uses the electrons to convert hydrogen peroxide to hydrogen and water. This causes a flow of electrons from the platinum side to the gold side which induces fluid motion around the particle causing the particle to move towards the platinum side [53, 106], Fig. 1.1 (c). This type of system work with spheres just as well as nanorods.

Other systems utilize a similar reaction but use the bubbles to push instead of pull. Conical microtubles comprised of a bilayer with polyaniline on the outside and platinum on the inside. Bubbles are generated inside the cone and are then forced out the back pushing the particle forward [102], Fig. 1.1 (d). Both types of motion based on catalysis of hydrogen peroxide do not work well for dense systems. The limitation comes from the fuel, since the particles consume it to move and do not generate it so it must be provided. Getting new fuel into the center of the system and ensuring there are not unwanted fuel gradients is still a challenge. There are also hydrodynamic effects which link the motion of the particles together as well as the fuel.

There have also been attempts made to mimic the motion of bacteria more closely using colloids. Using magnetic particles linked together by a flexible polymer, Dreyfus et

al. were able to create flagellated motion [107]. The flagella is driven by a time varying magnetic field. Since the particles want to align with the field it creates motion as the field rotates. This is an interesting way of mimicking the motion of bacteria but because of the way particle motion is generated swimmers can only move in one direction set by the motion of the magnetic field. This means that while these particles are active they will not be able to be used to study the dynamics of more than one swimmer at a time without changing the mechanism of flagellation.

In some of the previous active colloidal systems the level of activity or self propulsion can be tuned by the amount of hydrogen peroxide in the system. However, this is a finite resource that needs to be added to the system in order for the system to be active. Several systems have been developed that use an external source of light as the source of activity. This is done by using Janus particles which have one side that absorbs the lights which heats up the local fluid. This localized heating is used to propel the particles. This type of system has been made with hematite cubes embedded into a TPM polymer sphere [34], with graphite coated gold capped silica particles [108], and with graphite coated silica [103]. Because these systems use light to generate activity they do not work well in 3D but in 2D they can be used to investigate denser systems and without the problem of running out of fuel. The light intensity can also be tuned which mediated the activity level of all of the particles uniformly. Clustering has been seen in 2D and it is reversible, turn the light off and the clusters go away only to return when the light is turned back on.

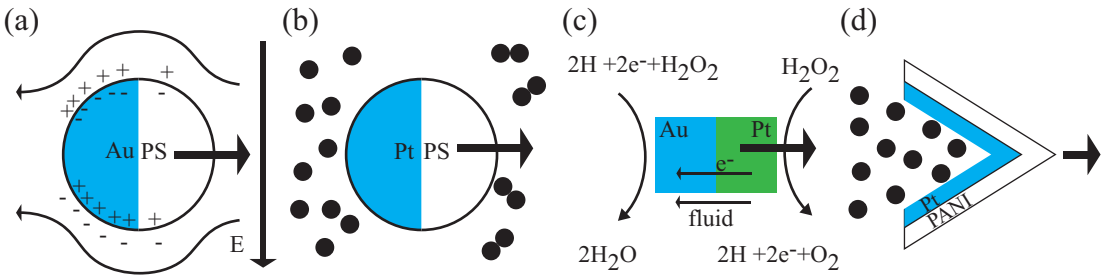

Figure 1.1: Examples of active colloidal mechanisms. (a) Polystyrene-Gold Janus particles that move under an AC electric field via induced-charge electrophoresis [54] (b) Polystyrene sphere on one side with platinum. The platinum is a catalyst for the chemical reaction of $2H_2O_2 \rightarrow 2H_2O + O_2$ which causes a local osmotic pressure difference which in turn causes the particle to move [52]. (c)Bimetallic rods made from platinum and gold. The platinum side converts the $2H_2O_2 \rightarrow 2H^+ + 2e^- + O_2$ while the gold side uses the electrons to convert $2H^+ + 2e^- + H_2O_2 \rightarrow 2H_2O$ The electrons flowing through the rod induced a flow in the surrounding fluid which moves the particle [53, 106]. (d) Conical microtubles comprised of a bilayer with polyaniline on the outside and platinum on the inside. The platinum is a catalyst for the chemical reaction of $2H_2O_2 \rightarrow 2H_2O + O_2$ which causes bubbles to be generated inside the cone which are then forced out the back pushing the particle forward [102].

Table 1.1: Table of existing active colloidal particles.

Type of Particle	2D/3D	Source of Motion	Conditions
Spinners [100]	2D	Rotating magnetic field	Dense
Rollers [32, 33]	2D	Electric field	Intermediate
Rollers [34]	2D	Light activated	Intermediate
Janus Particles [52, 53]	3D	Self-diffusiophoresis via H_2O_2	Dilute
Nano-propeller [101]	3D	Rotating magnetic triaxial field	Single particle
Rockets [102]	3D	O_2 microbubbles	Single particle
Metal Janus particles [54]	3D	AC electric field	Dilute

1.5.2 Athermal Systems

Active systems can also be realized in athermal systems. Shaken granular media or robots both can be activated either through the shaking of the particles or through batteries and

motors in robots. Currently, both types of systems only show activity in 2D, though there has been some initial work into aerial robotic swarms [109]. Beyond activity, collective motion can also be observed with both systems [30, 41, 55]

Granular particles in two dimensions can be shaken to stimulate motion. If the particles have no preferential direction of motion, shaking them produces effects analogous to Brownian motion. The introduction of anisotropy in the particles which gives them a preferred direction of motion is used to create an active system [20, 30]. This can be done by giving the particles bristles with a direction or by weighting the particles anisotropically. Both of these introduce symmetry breaking that is necessary for directed motion. Tuning the type of anisotropy can induce different motions in the particles.

Vibrated weighted disks can show polar ordering as all of the particles move together with self propulsion coupled with hard polar particles driving alignment [30]. Increasing the volume fraction of the disks leads to liquid and subsequently crystalline phases [110, 111]. In confined spaces the pressure of the active disks can be compared to the pressure exerted by Brownian disks [20]. The pressure from the active disks is much higher as evidenced by fewer active particles needed to balance a movable barrier between a region of active disks and a region of passive disks. Whether this pressure can be designated as a state function is yet to be seen [77, 81].

Vibrated rods can show nematic order as a possible state depending on density [31, 56, 112]. This system does not show polar ordering because the rods are symmetric, there is no difference between a front and back of a rod. When the rods are confined to two dimensions they show nematic order but when that confinement is removed the rods start to bounce out of plane. In systems that allow out of plane motion there are clusters of nematic order that coexist with regions of vertical rods [56]. This rod system can also be made to show polar order by changing the mass distribution similar to active disks [112]. At lower densities these active rods have a tendency to get stuck along the walls of the container similar to active colloids. At higher densities the rods show nematic order that is not constant in time.

Defects in the nematic order appear, move, and disappear.

The vibrated rod system is similar to a robotic system, bristlebots, that is also made of rod like particles in 2D but instead of having the vibration be global (from the whole apparatus shaking), each bristlebot has a battery and an eccentric motor that vibrates the individual robot [55]. The bristles on the bottom of the bot are asymmetric so each time the bot vibrates it moves along its axis. The angle of the bristles can also be changed and changes the behavior of the bot. Bristles that are close to vertical, perpendicular to the body, cause the bot to spin while shallower attachment angles cause the bot to walk along its axis. Both spinners and walkers show collective motion, either clustering or flocking respectively, as density is increased.

Other robotic systems have been made that are more goal orientated. A termite inspired robot has been designed that can build 3D structures using only local rules [113], i.e. there is no controller watching and directing. There is kilobot, a thousand robot swarm that can create specified patterns/structures in 2D, again using only local rules [41]. Kilobot is of interest because it is the first physical robotic swarm that approaches the size of an insect swarm or bird flock.

1.5.3 Active Liquid Crystals

Recent work has sparked interest in the motion of active liquid crystals [57, 114–117]. This system is made up of microtubule fiber bundles and is activated with kinesin or myosin motors. The activity is then provided by ATP, the level of which can be tuned. One of the nice aspects of this system is the ease of tuning the level of activity. This is one of only a few systems for which activity can be finely tuned beyond on or off. The individual fibers and fiber bundles are pushed together by the addition of polyethylene glycol (PEG) via depletion. PEG can also deplete the system to an interface so that it is 2D.

The 2D active liquid crystal shows nematic ordering but the nematic order is not static in time. Defects in the order are created, move, and are destroyed, as the fiber bundles

buckle, rupture, and move past each other. The defects can also interact hydrodynamically through the liquid crystal leading to another level of order [57]. This has been seen on flat sheets of liquid crystal, and can be stabilized using a magnetic field so that the motion of the defects persists over longer distances, on the order of millimeters [117]. The shear viscosity can also be measured by using different viscosity oils for the oil water interface and measuring the motion of the active liquid crystal at fixed ATP concentrations [116]. The defect creation and annihilation has also been studied on curved surfaces where topology sets the number of defects and curvature can set a preferred direction of motion of the defects [114, 118].

The microtubule systems have also been looked at in 3D instead of depleting it to a surface. In 3D, it is no longer nematic but an active gel [114]. This active gel was examined at a range of microtubule, PEG, and ATP concentrations. With low ATP, tracer particles suspended in the gel move subdiffusively. As ATP is increased the tracer particles become diffusive and eventually superdiffusive. The motion of the tracer particles can be used to gauge the level of activity of the gel. It is difficult to measure bulk material properties in the gel because microtubules tend to adhere to interfaces including solid-liquid interfaces. In addition the microtubules are suspended and so the whole system would be predominantly viscous if it could be measured. Work has also been done on actin myosin gels [119].

Instead of extensional fiber bundles, it is also possible to create contractile bundles using myosin motors instead of kinesin motors [119–121]. With this actin myosin system it is possible to change the rigidity of the filaments, something which has not been done with microtubule systems. The stiffer the actin is able to support higher stresses and as such needs higher levels of activity to overcome. The stiffness and the level of activity can also be used to tune how the defects interact with other defects. Hierarchical ordering is seen in the actin myosin system as with the kinesin microtubule system with defects aligning based on other nearby defects [121].

1.6 Biological Active Matter

Biological systems are inherently active as each constituent particle has it own store of chemical energy that it can then turn into kinetic energy. These types of systems range in size from cells [45, 58–60] to insects [65–68] to larger animals [48, 61–64].

1.6.1 Cells

Cells have evolved to be able to move in many diverse environments in both 2D and 3D, using a variety of motions [122–124]. These different types of actualizing self propulsion and environments mean that there is a wide variety of motion beyond Brownian that cells display. In 3D cells, two class of motion are pushers and pullers. Pushers have a flagella at the back of the cell that it uses to propel itself forward (e.g *E. Coli*) whereas pullers have flagella towards the front or sides m that they use to pull liquid past themselves (e.g. algae cells) [124, 125]. Pushers tend to run and tumble [125–127], pullers do as well though the hydrodynamics of their motion is different [128, 129].

The motion of cells is also dependent on the density of cells in the surrounding fluid [130]. As the cells swim they change the motion of the fluid around them, leading to an increase in their velocity at moderate density since the flow fields can align and make it easier to swim. At high densities the system is too crowded and the swimming speed drops back down since cells cannot travel far without running into other cells.

Cells can also effect the viscosity of the bulk fluid [131, 132]. Adding dead cells to a fluid increases the viscosity. Live puller cells increase the viscosity of the fluid even more so than was seen with the addition of dead. This effect is larger with increasing density [131]. Pushers, on the other hand, can decrease the viscosity of the fluid [132, 133]. In dilute cases pushers can lower the viscosity to essentially zero, a superfluid like state.

Some cells are phototactic, meaning that they are attracted to light. This allows for the directed motion of the active cells and for observing the transition from directed to random

motion [134]. Cells will also move along chemical gradients which can also be designed to direct their motion [135]. *E. Coli* have the tendency to turn right when moving down a channel which can be used to sort them [125].

On solid substrates some types of cells can move in both two and three dimensions. In 3D this amounts to movement through materials like an extracellular matrix, a linked network with a pore size large enough for the cells to move through. In 2D cells are able to walk along surfaces mediated by cell substrate adhesions [136–140]. These adhesion forces between cells and substrates is not necessarily the same for individual cells as for aggregates of cells [137].

Individual cell behavior changes as density is increased. For example in 2D, the interactions of the cells can generate spontaneous flows when confined [43], and if confluency is reached can display glassy dynamics [42]. Confluency is the point at which no more cells can fit into a 2D layer. Once dense these cell aggregations can either stay as separate cells or can link together through chemical linkages, for example, E-cadherin molecules [141]. These bonds can take different forms, each of which has its own binding ability [136, 139, 140] but all of which bring elasticity to the cell aggregate [142, 143]. This elasticity comes from the linkages but also comes from the elasticity of the cells themselves [144, 145]. While in aggregations it is still possible for cells to move and rearrange [45, 146]. In spindle shaped cells in 2D when the cell density gets to confluency it is possible to see nematic order in the aggregations [44, 147, 148].

1.6.2 Large Animal Collectives

While cells comprise the small end of the size spectrum of biological active matter, there has also been work done on collectives of larger animals; fish, birds, herds, and humans. In all of these types of collectives it is not necessary for the individuals to be in physical contact for the group to stay together. For example, starlings regulate the distance between themselves within the flock by observing the motion of the nearest neighbors but only out

to a distance of about two birds away [62–64, 149]. Schools of fish are similar but can add hydrodynamic interactions since they are in water [71, 150].

This desire to maintain a set distance with their neighbors acts as a repulsive force between constituents. For biological reasons they do not want to be too far from their neighbors because there is a benefit to being in the collective. Preventing predation, mating, foraging, and improving transportation efficiency are all reason to want to stay with the collective. These goals of staying together but not getting too close lead to long range attraction and short range repulsion. This can lead to a solid-like behavior which has been seen in bird flocks [63] but mostly leads to cohesiveness without significant elasticity. A school of fish is more likely to go around an obstacle than bounce off.

Birds and fish exist primarily in three dimensions, though it is possible to confine fish to 2D with shallow water and there are flightless birds. Humans and herds of animals are confined to two dimensions normally. Since 2D is one less degree of freedom of motion, the first active matter theories were based on the motion of herds [49, 50]. This collective motion can even be seen in humans [46, 48, 151]. The flow of human crowds can display topological interactions, vortices of humans coalesce with the same rules as fluid vortices [48]. Though more work has been done into how pedestrians move along paths [46, 151] since this has practical applications in the design of city infrastructure. This has also been extended to include cars driven by humans as a form of active matter [152].

1.6.3 Bugs and Ants

In the middle between large animal collectives and cells, lie insects. Lots of insect species show collective behavior. Classic examples being fly swarms, termites, locusts, bees, and ants. Midge swarms in a laboratory environment form at a size that is related to their number in order to keep the same inter-insect spacing similar to how birds or fish exhibit short range repulsion [153]. Termites show both swarming behavior and the ability for termite groups to build mounds which would not be possible for an individual. Both of

these behaviors can be modeled using robots [65, 113].

Bees show multiple types of swarming behavior. In flight bee swarms behave similar to flies or birds, maintaining distance and going in the direction of their neighbors [154]. However if the swarm lands somewhere without a nest the bees can land on top on one another forming an aggregation [66]. Bee aggregations show both a solid-like and a liquid-like response. The aggregation can stay together and hold its shape but is also dynamic and can dissipate energy. For example when the tree branch the aggregation is on shakes, the bees are able to hold shape and to the branch while dissipating the energy so no bee is flung off or crushed. These collective behaviors are very different from what an individual bee will do either in a colony or searching for food [155, 156].

Like bees, ants display collective behavior that is more than what an individual can do. Individual ants can perform a specific search pattern when looking for food or other ants [157, 158]. They tend to turn left [159]. Individuals are more likely to be continually active in their search whereas once there are enough ants together some become lazy and many ants will stay in place, not moving [160, 161]. The level of activity in individuals and in the colony is not constant. Ants go through many sleep cycles per day [162] and colony go through day/night, seasonal, and short term cycles [163–165].

Some species of ant are able to perform large scale collective motion and build structures [165–167]. Army ants will mill, which is the whole group all moving in a circle [168]. They also forage without establishing a nest. A foraging colony can be 10^5 foragers and be $100\ m$ long [169]. They do not establish a permanent nest but do build temporary ones out of themselves. They also use the same ability to grab onto one another to form bridges along the raiding lane as a way of improving the efficiency of a route [170].

Fire ants, *Solenopsis invicta*, are also able to link their bodies together in order to form rafts, towers, bridges, and other structures [165, 171–175]. This ability to form rafts and to create structures out of themselves, in addition to being alive and so transforming internal energy into motion, allows us to use ants to explore active matter [67, 68]. Groups of

ants together as a material are called aggregations since they are active collectives with the addition of cohesiveness. These aggregations move on timescales measurable with rheology and through real space imaging. They are dense, they percolate space at raft densities and can be packed in tighter, allowing us to probe effective volume fractions from ~ 1 to 4.4. The effective volume fraction of a system is a generalization of the volume fraction for particles based on an effective volume, often larger than their physical volume: $\phi_{eff} = \frac{N \times V_{eff}}{V}$, with N the number of particles and V_{eff} the effective volume of one particle. For the ants we use a sphere with a diameter related to the interant distance.

We cannot measure ant aggregations with ϕ_{eff} below $\phi_{RCP} = 0.64$ because below this value ants do not percolate the system. At $\phi_{eff} \approx 1$ fire ant aggregations are viscoelastic, exhibiting both solid-like and liquid-like responses. An example elastic response is shown in Fig. 1.2 where an aggregation compressed between two petri dishes elastically returns to the original shape when the top petri dish is removed. The liquid-like response can be demonstrated by dropping a disk through a vertical 2D aggregation, Fig. 1.3. We see that the ants flow around the disk allowing it to pass. The combination of these two responses encompass the viscoelasticity of the system.

This mechanical response is not constant in time however. The ant aggregation undergoes cycles of activity. These cycles allow us to probe the aggregation when it is in different activity states. This is one of the first experiments where we have a multiple measurable activity levels.

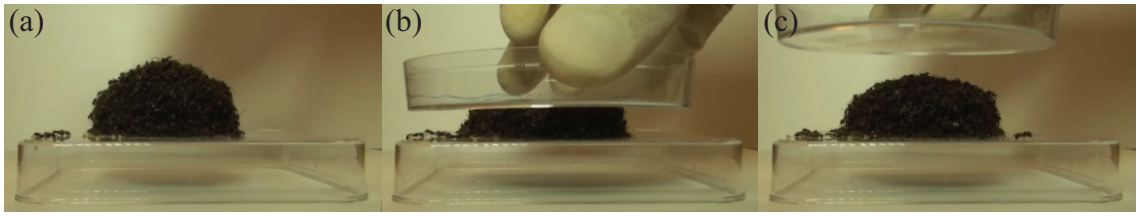

Figure 1.2: (a-c) A petri dish compresses an ant aggregation, which is then left unperturbed. The time lapse between images is $0.2\ s$. This experiment exemplifies the elastic nature of the ant aggregation in two ways: (i) the aggregation returns to its original shape after being compressed and (ii) the aggregation maintains a specific shape.

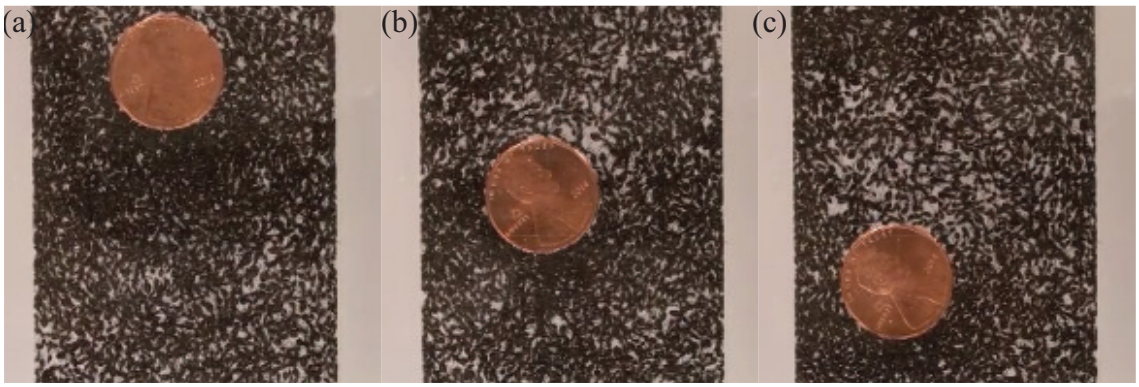

Figure 1.3: (a-c) A penny is placed on top of a 2D ant aggregation confined between acrylic sheets. The aggregation is vertical and as such the penny feels the pull of gravity. As time passes, the penny falls through the aggregation. The time lapse between images is $90\ s$. The ants flow around the penny allowing it to fall at a speed, $u \approx 2 \times 10^{-3}\ cm/s$, exemplifying the viscous nature of the ant aggregation.

1.7 Outline

In chapter 2 we discuss the methods and materials used in this body of work. We cover fire ant biology as it pertains to this work, including descriptions of how to acquire and maintain fire ant colonies in the lab. We discuss the modifications made to the rheometer in order to work with ants and the inherent limitations of the machine. A theoretical background in rheology is established here as well.

In chapter 3 we discuss linear oscillatory rheology of ant aggregations. We find that ant aggregations are equally viscous and elastic within the frequency range we probe at ϕ_{eff} close to the density of ant rafts. We find that the frequency dependent viscoelastic response is consistent with the Kramers-Kronig relations and that the aggregation "equally" stores and dissipates energy. We correlate the normal force exerted by the aggregation with the level of activity and monitor how the activity changes the rheological response of the aggregation. We track these activity cycles in the rheometer and through 2D real space imaging. We then construct a kinetic model of these activity cycles where the activity is related to the number of active ants in the system. We find that the transition rates between active and inactive is not constant in time, meaning that the more ants that are active the more

that can become active. For active ants, when volume fraction is increased the aggregations become predominantly elastic and approach the elasticity of to dead ants. This happens first because of crowding and then at high volume fraction the ant aggregations jam. The maximum density predicted by the observed jamming is close to the density of chitin which is what comprises the ants exoskeletons.

In chapter 4 we discuss creep experiments. When applying a constant stress to ant aggregations we find that depending on the magnitude of the applied stress the aggregations are able to resist the applied stress or simply flow. This transition from simply flowing to resisting the applied stress comes from the activity of the ants and we correlate this with the normal force. At applied stress below this transition we observe cycles in the level of the activity of the aggregation. These are most pronounced at zero applied stress where there is measurable motion even though no stress within the limits of the rheometer is applied. This is unseen for equilibrium materials. We correlate the values of the normal force and hence the activity with the creep experiments. We also calculate viscosities based on these tests.

In chapter 5 we discuss controlled shear rate experiments, an intrinsically nonlinear rotational test. We find ant aggregations shear thin when forced to flow. At the lowest shear rates that we measure we find viscosities similar to peanut butter. This behavior remains essentially unchanged when we repeat the experiment with dead ants, meaning that the response is not based on activity. We link the shear thinning behavior to the mechanics of the ants' bodies themselves and connect to the results from creep experiments.

In chapter 6 we discuss nonlinear oscillatory rheology. We determine the nonlinear response of the aggregation to oscillatory shear strains by looking at the waveform of the resultant stress at high strain amplitude. We use a theoretical foundation put forward by Ewoldt et al. to describe the nonlinear response. This formulation is illustrated using attractive and repulsive emulsions as an example system. We find that ant aggregations shear thin and strain stiffen at large strains and strain rates within one oscillation. This means that

at the largest strains ($\gamma = \gamma_0$) within one cycle the stress is higher than would be expected from linear response and the highest strain rates ($\gamma = 0$) the stress is lower than expected. This deviation from linear response we measure as the level of nonlinearity. At high strain amplitude there is no difference in the degree of nonlinearity between active and inactive aggregations consistent with controlled shear rate experiments where we saw the same nonlinear viscous behavior with live and dead aggregations. At intermediate strains there is a dependence on activity of the level of viscous nonlinearity that is not there at low or high strains. We repeat this measurement at a higher ϕ_{eff} within the crowding regime. We find that the level of elastic nonlinearity does not change but the level of viscous nonlinearity changes with both density and activity. We understand the change in the viscous nonlinearity by discussing the linking and unlinking events in the aggregation. On average the number of linking and unlinking events is the same which means that the network does not change and so the level of elastic nonlinearity does not change between active and inactive aggregations. However, the number of events does change and increasing the number of linking/unlinking events decreases the level of viscous nonlinearity. This can be done both by switching from an inactive to an active aggregation and by increasing the density within the crowding regime.

Overall, we learn that the level of activity affects the mechanics of the system. The activity level changes naturally in ant aggregations in time which allows us to measure the mechanics at different activity levels. We show that it is possible to overwhelm an active system through external perturbations such that the activity does not play a role in the mechanics. However, within the realm where the activity plays a role, it can be used to tune the material properties of the system without changing the structure of the system itself.

CHAPTER 2
METHODS AND MATERIALS

2.1 The System: Fire Ants

Fire ants, *Solenopsis Invicta*, are native to South America, originally the Panatal region of Paraguay and Brazil [165]. They came to the United States via boats starting in the early 1900s [165, 176] where from a few starting ports they have colonized much of the southern United States. Fire ants are an interesting species because of their ability to link together to form rafts and other structures [165, 166, 173, 174, 177]. They evolved to have this ability as a way for colonies to survive annual flooding in their native region.

In these dense states, fire ants have outgoing connections from all six legs and their mandibles [178], and can have incoming connections anywhere on their bodies [173]. The ants' tarsi, feet, have sticky pads on them that allow them to attach anywhere on neighboring ants. The sticky pads also allow them to walk on almost all surfaces in any direction, except for Teflon and surfaces coated in talcum powder. Fire ants also have hooks on their tarsi at the ends of their legs [166]. Connections via linked hooks form the strongest link that ants can form; it takes $2\ mN$ forces to break these connections, about 200 ant weights [38]. The ants exoskeleton is made of chitin which has a density between 1.31 and $1.41\ g/cm^3$ and in its crystalline α-chitin form has an elastic modulus of $\sim 50\ GPa$ [179, 180].

Fire ants colonies can be maintained in a laboratory environment but it is not possible for new colonies to form as the specific weather conditions necessary for mating flights are not feasible in the lab. To perform experiments in the lab we must first collect and subsequently maintain fire ant colonies. These are collected from roadsides around Atlanta, GA, using the drip float method [67, 165, 181]. This method involves digging up the entire

colony as well as the surrounding dirt, which are then placed into five gallon buckets. The bucket's side walls are coated in talcum powder prior to adding the colony. To separate the dirt and the ants once the buckets are brought to the lab, we drip water into the buckets at a rate of about one drop per second using tubing with inner diameter $(4.4 \pm 0.2)\ mm$. This is done until the water level is at least an inch higher than the dirt. Since fire ants are able to form rafts, they float to the surface, Fig. 2.1 (a). We remove the floating ants and place them into a long term storage bin. The bins are open at the top but the sides are coated with talcum powder or Fluon, both of which prevent the ants from escaping. Fluon is a suspended fluoropolymer that when painted onto the bin dries forming a layer on the bin which is too slippery for the ants to walk on.

The bins contain synthetic nests made from upside down Petri dishes covered in black tape. The tape is to prevent light from getting in. After the colony has been in the bin for a couple days they will have moved all of the eggs and the queen(s) into the nest as they normally nest underground. Most of the time the males stay in the nest as well. Ants used in experiments are collected from the edges of the bin to make sure that no eggs or queens are included in experiments. Males sometimes get collected but they are removed and placed back in the colony, thus only worker ants are used in experiments. New colonies were given a week to acclimate to the lab before being used in experiments [177]. Despite fire ants being omnivorous and able to eat a variety of things, in the lab we feed them high protein baby food, and occasionally wet cat food. Water is available all the time in vials plugged with cotton balls, Fig. 2.1 (b).

(a)  (b) 

Figure 2.1: (a) 5 gallon buck with an ant raft floating above dirt. This is the last in bucket step before the ants are moved to their storage bin. The block of wood is used to keep the drip tubing centered in the bucket. The walls are coated with talcum powder. (b) Storage bin of an ant colony. This image was take the same day that the ants were added to the bin and they have not yet moved into the nest. The nest is in the top right. There is food in the top left. Water filled tubes are on the right in front of the nest.

Fire ant workers range in size from one to six millimeters and can be found at all lengths in between [165]. This is unlike many ant species that have only a few distinct sizes of ants in the colony. Measured distributions of lengths from three representative colonies are shown in Fig. 2.2. There is a main peak of smaller ants as there are more of them in colony [165] and a second much smaller peak of larger ants. To estimate the ant mass, we divide the mass of a group of ants by the number of ants. We find an average ant mass and length in a typical aggregation we use of $m_{ant} = (0.7 \pm 0.1)\ mg$ and $l = (3.2 \pm 0.3)\ mm$.

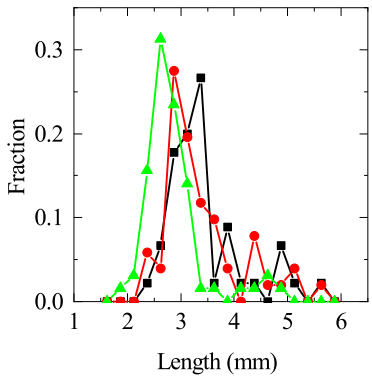

Figure 2.2: Typical distributions of the length of individual ants for three colonies. N = 45, 51, and 61. The average and standard deviation are, $l = (3.4 \pm 0.7)\ mm$, $l = (3.4 \pm 0.7)\ mm$, and $l = (2.9 \pm 0.6)\ mm$ respectively. For each distribution there is one main peak and then a few larger ants.

For experiments with dead ants we kill the ants with liquid nitrogen right before the start of the experiment. Fire ants keep their dead in piles and so it is also possible to collect dead ants from the bins. However, the dead bodies dry out and decay and so are not comparable to inactive live ants, whereas the freshly frozen dead ants are comparable.

2.2 Rheology

Rheology is the study of how materials behave. It provides a framework that can be used to inquire about the properties of simple liquids to soft solids. The motto of the Society of Rheology is "$\pi\acute{\alpha}\nu\tau\alpha\ \rho\epsilon\acute{\iota}$",that is "Everything Flows". Importantly however, everything does not flow at the same timescale. The Deborah number, a dimensionless time which relates the timescale of relaxation τ_0 and the timescale of deformation τ_D, $De = \tau_0/\tau_D$ [182] is used to characterize whether to expect flow. While for measurement timescales faster than the system can relax the system behaves solid-like, $De > 1$, for longer measurement timescales the system flows exhibiting liquid-like behavior, $De < 1$. Materials which exhibit a solid-like response at short times and a liquid-like response at long times are called viscoelastic.

In general the mechanical response of a material is described using the total stress tensor $\boldsymbol{T} = \boldsymbol{\sigma} - p\boldsymbol{I}$, where p is the pressure, $\boldsymbol{I}$ is the identity tensor, and $\boldsymbol{\sigma}$ is the extra stress tensor. This means that the stress on a material is given by the extra stress tensor up to the addition of an isotropic pressure. Since $\boldsymbol{\sigma}$ is symmetric in the linear regime with only σ_{11}, σ_{22}, σ_{33}, σ_{12}, σ_{13}, and σ_{23} being non-zero and non-redundant. The strain also has a similar symmetric tensorial form. Simple shear is defined by a material sandwiched between two plates which experiences motion of the top plate along one axis, Fig. 2.3. For simple shearing flow the only relevant term in the strain tensor is $\gamma_{12} = \gamma_{21}$. In the stress tensor there is one off diagonal term σ_{12} and the diagonal terms which give normal force relations. Since we are concerned with shear we can reduce from the tensorial form to a scaler form with the stress, σ, in place of σ_{12} and the strain, γ, instead of γ_{12} [182–185].

Outside of the linear regime the stress tensor is assumed to still be symmetric.

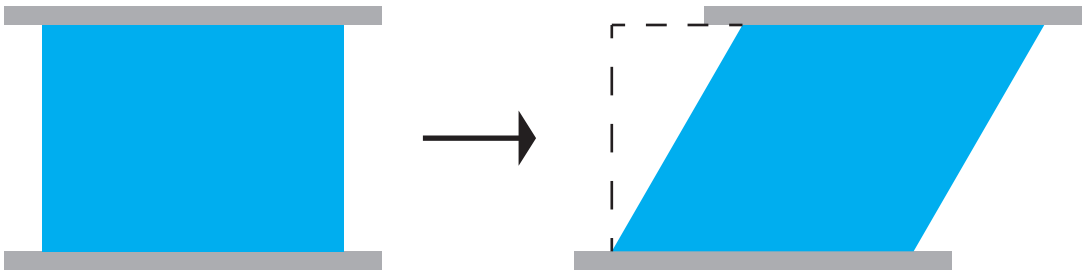

Figure 2.3: Schematic of simple shear.

For an applied step stain, the relaxational modulus is defined as $G(t) = \sigma(t)/\gamma_0$, with γ_0 being the magnitude of the step strain. Small changes in stress are related to small changes in strain by $d\sigma = G(t)d\gamma$. This can also be written as $d\sigma = G(t)(d\gamma/dt)dt$, where $d\gamma/dt$ is the strain rate $\dot{\gamma}$. By integration we then see that the stress is dependent of the relaxational modulus and the history of previous strains,

$$\sigma(t) = -\int_{-\infty}^{t} G(t-t')\dot{\gamma}(t')dt'. \tag{2.1}$$

This history dependence is built up from many infinitesimal strains and their responses. For a simple purely elastic material, $G(t) = G_0$ and so follows Hooke's Law, $\sigma = G_0\gamma$, where G_0 is an elastic modulus. For a viscous material the stress is related to the shear rate, $\dot{\gamma}$, by the viscosity, η, via $\sigma = \eta\dot{\gamma}$.

There are two main simple models used in rheology to describe viscoelastic materials: the Maxwell model for a viscoelastic fluid, and the Kelvin-Voight model for a viscoelastic solid [182–186]. The Maxwell model describes a system that has short time elasticity but flows like a liquid over long timescales. The Kelvin-Voight model describes a system that is elastic over long timescales but flows at short times. Other models include the Bingham model for plastic behavior, where a material undergoes unrecoverable strain; the Cross or Carreau models for shear thinning, materials where the viscosity decreases with increasing

strain rate; the power law model which describes a generalized Newtonian fluid, this model can describe the full spectrum of shear thinning through Newtonian to shear thickening; the Herschel-Bulkley model which is the power law model with a yield stress, yield stress materials are elastic below a certain stress and flow like a liquid for larger stresses; and more.

The Maxwell model can thought of as being made up of an elastic component in series with a viscous component, shown in Fig. 2.4 (a). The total strain is the sum of the strains of the two elements: $\gamma = \gamma_{elastic} + \gamma_{viscous}$. Combining the equations for the viscous and elastic strains we get:

$$\dot{\gamma} = \frac{\dot{\sigma}}{G_0} + \frac{\sigma}{\eta}. \tag{2.2}$$

The Kelvin-Voight model has the elastic element in parallel with the viscous element, Fig. 2.4 (b). The spring in parallel generates the long time solid response. For this system the strain is the same for both elements but the stress is not and so the total stress is represented by the sum of the stress elements, $\sigma = \sigma_{elastic} + \sigma_{viscous}$. Combining the viscous and elastic stresses yields:

$$\sigma = G_0\gamma + \eta\dot{\gamma}. \tag{2.3}$$

These two models are often used to interpret the rheology of materials [67, 187, 188]. Here we will use them to exemplify typical responses to standard rheological experiments.

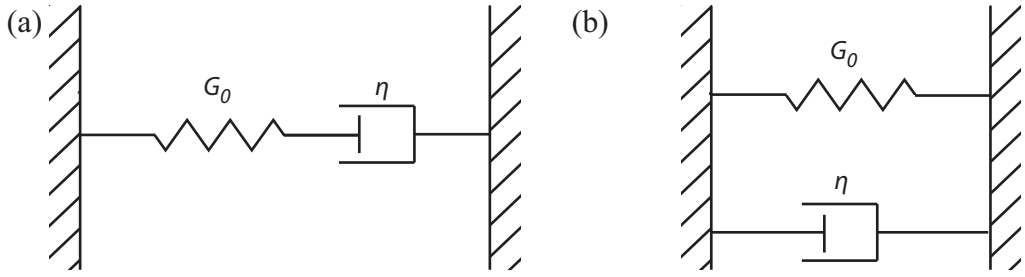

Figure 2.4: (a) Maxwell model for a viscoelastic fluid. It is comprised of a viscous dashpot with viscosity η and an elastic spring with spring constant G_0 in series. (b) Kelvin-Voight model for a viscoelastic solid. It is comprised of a viscous dashpot with viscosity η and an elastic spring with spring constant G_0 in parallel.

There are three different classes of rheological tests with monotonic strains: creep, controlled shear rate (CSR), and stress relaxation. They vary based on what is applied and what is measured. Creep tests apply a step stress and measure strain as a function of time. Controlled shear rate tests apply a step shear rate and measure the stress necessary to maintain it. Stress relaxation tests apply a step strain and measure stress as a function of time.

2.2.1 Creep

Creep tests apply a constant stress, σ_0, starting at $t = 0$, Fig. 2.5 (a), and then measure the strain as a function of time. First lets apply this test to the Maxwell model. Constant stress implies $\dot{\sigma} = 0$. Using Eq. 2.2 gives the steady state behavior $\dot{\gamma} = \sigma_0/\eta$. Integrating the shear rate and using that $\gamma(t = 0) = \sigma_0/G_0$ due to the short time elastic response gives that

$$\gamma(t) = \frac{\sigma_0}{\eta}t + \frac{\sigma_0}{G_0} = \sigma_0 J_{c,Maxwell}(t), \tag{2.4}$$

where $J_{c,Maxwell}(t)$ is the creep compliance in Maxwell's model. We see that at short times the material responds elastically and then flows as a viscous liquid for long times, Fig. 2.5 (b).

For the Kelvin-Voight model, Eq. 2.3, a constant stress implies that $\sigma_0 = G_0\gamma + \eta\dot{\gamma}$. We can then solve for γ using that $\gamma(t = 0) = 0$ since the viscous component of the system cannot respond instantaneously, we find

$$\gamma(t) = \frac{\sigma_0}{G_0}(1 - e^{-t/\tau}), \tag{2.5}$$

with $\tau = \eta/G_0$. There is flow at short time but the strain plateaus to a value of σ_0/G_0 because the spring and dashpot are in parallel and eventually the spring dominates getting up to a constant strain value, Fig. 2.5 (c).

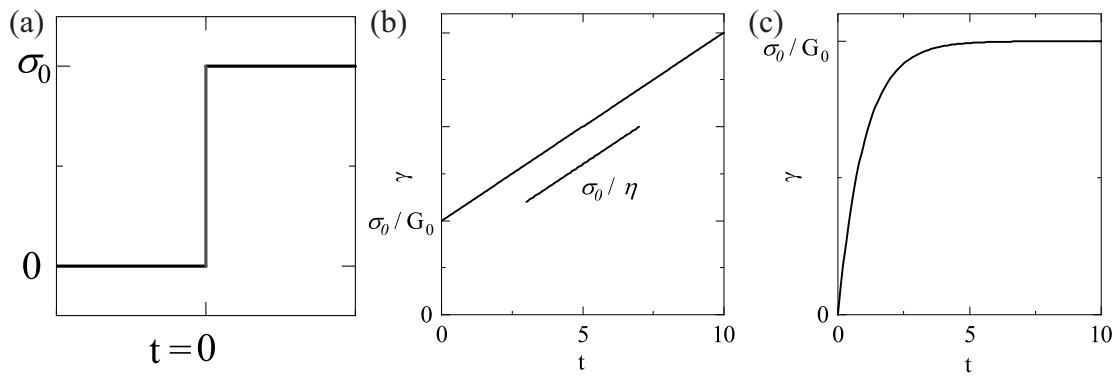

Figure 2.5: (a) Stress as a function of time for a creep experiment. At $t = 0$, the stress turns on to a set value of σ_0. (b) The Maxwell model under constant applied stress, σ_0. The strain jump at $t = 0$ to σ_0/G_0 is indicative of the short time elasticity of the system. For long times the system flows under the applied stress with a constant shear rate of σ_0/η. (c) The Kelvin-Voight model under constant applied stress, σ_0. Since the elastic and viscous components in this model are in parallel, the elastic component eventually dominates leading to an approach to a finite strain.

2.2.2 Controlled Shear Rate

For controlled shear rate tests a constant shear rate is applied and the stress necessary to maintain that shear rate is measured. Since the system is being forced to flow this is an inherently non-linear test and as such neither the Maxwell or Kelvin-Voight models are completely valid. Ignoring the elastic component in both models, $\dot{\sigma}/G_0$ in the Maxwell model and $G_0\gamma$ in the Kelvin Voight model, yields the same response, $\sigma = \eta\dot{\gamma}$. Both models however only have a single Newtonian viscosity. While true in the linear regime or for Newtonian fluids, when forced to flow the viscosity often depends on the shear rate at which it is flowing, $\eta(\dot{\gamma})$. The stress can then be generalized as: $\sigma = \eta(\dot{\gamma})\dot{\gamma}$.

The behavior of $\eta(\dot{\gamma})$ then tells us first whether the fluid is Newtonian or non-Newtonian, and if it is non-Newtonian whether it is shear thinning or shear thickening. Shear thinning materials have a viscosity that goes down with increasing shear rate, while shear thickening material's viscosity increases with increasing shear rate.

Creep tests can be used to corroborate the results from controlled shear rate experiments for viscoelastic fluids. At long times the shear rate from a creep test is constant for a

viscoelastic fluid, Fig. 2.5 (b). This shear rate and the applied stress give one point on a stress vs shear rate or viscosity vs shear rate plot. Because there is short time elasticity and long time flow, we need to make sure when performing a controlled shear rate test that we are waiting for a long enough time to measure the flow behavior. Multiple creep tests combined with a controlled shear rate test tells us whether we are waiting for long enough times for the data to be meaningful when running the test.

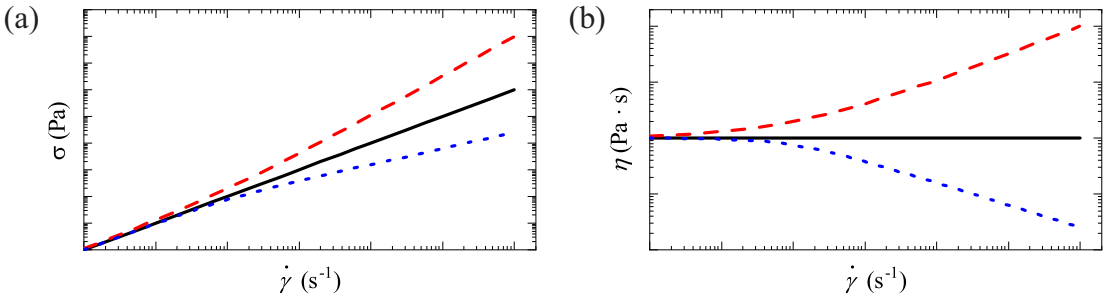

Figure 2.6: (a) Stress versus shear rate for a Newtonian system (black), a shear thinning system (blue), and a shear thickening system (red). (b) Viscosity versus shear rate for the same systems in (a). It is found from $\eta = \sigma/\dot{\gamma}$.

2.2.3 Stress Relaxation

Stress relaxation tests apply a constant strain, γ_0, starting at $t = 0$, Fig. 2.7 (a), and then measure the stress as a function of time. First lets apply this test to the Maxwell model. Constant strain implies $\dot{\gamma} = 0$. Using Eq. 2.2 we get the differential form: $\dot{\sigma} = -(G_0/\eta)\sigma$. Integrating the shear stress and using that $\sigma(t = 0) = G_0\gamma_0$ due to the short time elastic response gives that

$$\sigma(t) = G_0\gamma_0 e^{-(G_0/\eta)t}. \tag{2.6}$$

We see that at short times the material responds elastically and then the stress relaxes with a characteristic timescale of G_0/η, Fig. 2.7 (b).

For the Kelvin-Voight model, Eq. 2.3, a constant strain implies that $\sigma = G_0\gamma_0$. Because the viscous and elastic components are in parallel a constant strain causes a constant stress since there is no way for the stress to relax.

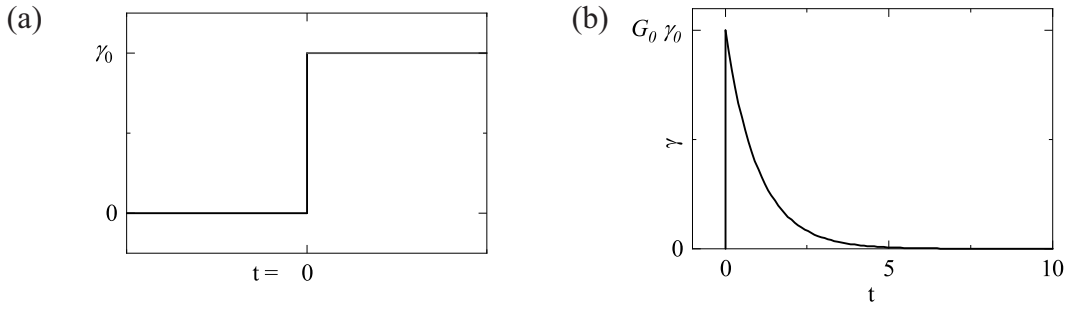

Figure 2.7: (a) Strain versus time for a stress relaxation test. (b) Stress versus time for the Maxwell model subject to the strain shown in (a).

2.2.4 Small Amplitude Oscillatory Shear

In addition to tests with monotonic strains there are also oscillatory tests. These are done by applying an oscillatory strain, $\gamma(t) = \gamma_0 \sin(\omega t)$ and measuring the stress response, $\sigma(t)$, where γ_0 is the strain amplitude and ω is the frequency of oscillation. Small Amplitude Oscillatory Shear is done at small strains where the stress is linear with the strain and so the stress can also be described by a single sinusoid. The regime where this is true is called the linear regime. This regime can be found by repeating an oscillatory measurement with one frequency and different strains and locating the region where the moduli are independent of stain amplitude. It is also the region of a stress strain plot where Hooke's law and Newtons law of viscosity are valid; the strain is not large enough to cause nonlinear deformation or deformation rate and the test as a result does not change the material.

In the linear regime the stress is a single sinusoid like the strain but with a phase difference, $\sigma(t) = \sigma_0 \sin(\omega t + \delta)$, Fig. 2.8 (a). This phase lag means that the stress can be decomposed into a sine and a cosine term $\sigma(t) = \sigma' \sin(\omega t) + \sigma'' \cos(\omega t)$ with $\sigma' = \sigma_0 \cos(\delta)$ and $\sigma'' = \sigma_0 \sin(\delta)$ via trigonometric summation identity. The sine term is in-phase with the strain and characterizes the elastic response and is represented by the Storage modulus, $G' = \sigma'/\gamma_0 = \sigma_0 sin(\delta)$. The cosine term is out-of-phase with the strain and characterizes the viscous response, represented by the Loss modulus, $G'' = \sigma''/\gamma_0 = \sigma_0 cos(\delta)$. The two moduli can also be related to the phase lag by $tan(\delta) = G'/G''$.

The waveforms of an applied strain and the resultant stress for an example viscoelastic material with $\delta = \pi/4$ are shown in Fig. 2.8 (a). We can also represent the result by plotting the stress versus the strain in a Lissajous-Bowditch curve, Fig. 2.8 (b). In this representation a perfectly elastic material would be a line with a slope equal to G_0, and a perfectly inelastic material would be a circle. More generally, viscoelastic materials show an ellipse, since they are both viscous and elastic. For any material the area enclosed by the loop is related to the Loss modulus. The area within the ellipse is given by

$$\int_{-\gamma_0}^{\gamma_0} \sigma(t) d\gamma = \int_{0}^{2\pi/\omega} \sigma(t)\dot{\gamma}(t) dt. \tag{2.7}$$

Introducing the shear rate and the general form of the stress, we obtain

$$\int_{0}^{2\pi/\omega} (\sigma' \sin(\omega t) + \sigma'' \cos(\omega t))(\gamma_0 \omega \cos(\omega t)) dt$$
$$= \gamma_0 \omega \Big[(\sigma'(-\frac{1}{2\omega}\cos^2(\omega t)) + \sigma''(\frac{t}{2} + \frac{\sin(2\omega t)}{4\omega}) \Big]_0^{2\pi/\omega} = \sigma'' \gamma_0 \pi. \tag{2.8}$$

Therefore the relation between the area and the Loss modulus is: $G'' = (1/(\pi\gamma_0^2)) \int \sigma\dot{\gamma} dt$. The slope of the in-phase stress σ'/γ_0, is the Storage modulus, G'. The slope of the major axis is the magnitude of the complex modulus, $|G^*|$ [189]. The complex modulus combines the Storage and Loss moduli into one modulus that has real and imaginary components, $G^* = G' + iG''$ with magnitude, $|G^*| = \sqrt{G'^2 + G''^2}$ in the linear regime. It is also the one-sided Fourier transform of the relaxational modulus, $G^* = \mathcal{F}\langle G(t)\rangle$. The storage modulus can also be found from $G' = (\sigma(\gamma_0) - \sigma(-\gamma_0))/(2\gamma_0)$ or from the slope of the stress as it reaches $\gamma = 0$, $G' = d\sigma/d\gamma|_\gamma = 0$. Frequency sweeps at constant strain can then be performed to measure the frequency dependence of the Storage and Loss moduli.

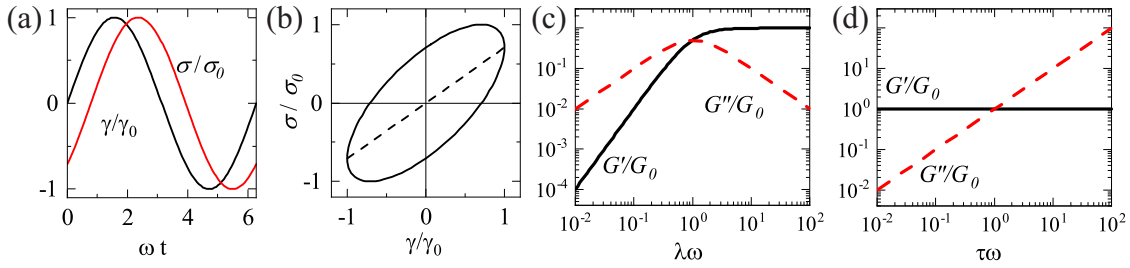

Figure 2.8: (a) Normalized strain (black) and stress (red) vs dimensionless time, ωt. The strain has the form of $\gamma(t) = \gamma_0 sin(\omega t)$ and since this is in the linear regime the stress has a similar form but with a phase lag, $\sigma(t) = \sigma_0 sin(\omega t + \pi/4)$. (b) Lissajous-Bowditch plot of the stress versus the strain in the linear regime. G' is represented by the dashed line. (c) Frequency sweep of the Maxwell model. The model is more elastic at low frequency and more viscous at high frequency. The crossover occurs at $\tau\omega = 1$. (d) Frequency sweep of the Kelvin-Voight model. Since the Storage modulus is constant and the Loss modulus is increasing, the model is more viscous at low frequency and more elstic at high frequency. The crossover occurs at $\tau\omega = 1$. In (c) and (d) the Storage modulus, G', is the solid black line and the Loss modulus, G'', is the dashed red line.

We can find this frequency dependence by representing the strain as complex functions. The strain as $\gamma = \gamma_0 e^{i\omega t}$ and the stress as $\sigma = \sigma_0 e^{i\omega t+\delta}$ which is similar in form to the strain but with a phase lag. Since we can relate δ to the storage and loss modulus we can plug these representations of the stress and the strain into the Maxwell model and the Kelvin-Voight model to determine the frequency response of each model.

Using the Maxwell model, Eq. 2.2, the strain, the stress, and the time derivative of the stress we get,

$$i\omega\gamma_0 e^{i\omega t} = \frac{i\omega\sigma_0 e^{i\omega t+\delta}}{G_0} + \frac{\sigma_0 e^{i\omega t+\delta}}{\eta}. \tag{2.9}$$

We can then cancel $e^{i\omega t}$ from both sides and rearrange to isolate $\sigma_0 e^{i\delta}/\gamma_0$ and introduce $\tau = \eta/G_0$, the relaxation timescale,

$$\frac{\sigma_0}{\gamma_0} e^{i\delta} = i\omega(\frac{i\omega}{G_0} + \frac{1}{\eta})^{-1} = G_0 \frac{\tau^2\omega^2 + i\tau\omega}{1+\tau^2\omega^2}. \tag{2.10}$$

The real component is the Storage modulus, $G'(w) = G_0 \frac{\tau^2\omega^2}{1+\tau^2\omega^2}$ and the imaginary component is the Loss modulus, $G''(w) = G_0 \frac{\tau\omega}{1+\tau^2\omega^2}$. For frequencies above τ the system responds

elastically, $G' \to G_0$ and $G''\ \omega^{-1}$. For low frequencies when the system has time to relax, $G' \sim \omega^2$ and $G' \sim \omega$, it flows since $G'' > G'$ at long times, Fig. 2.8 (c). The frequency at which the system crosses over from being predominantly viscous to predominantly elastic happens at $\omega_c = 1/\tau = G_0/\eta$.

To examine the Kelvin-Voight model we use, Eq. 2.3, and the strain, the shear rate, and the stress from above to obtain,

$$\sigma_0 e^{i\omega t+\delta} = G_0\gamma_0 e^{i\omega t} + \eta i\omega\gamma_0 e^{i\omega t}. \tag{2.11}$$

We can then cancel $e^{i\omega t}$ from both sides and again solve for $\sigma_0 e^{i\delta}/\gamma_0$,

$$\frac{\sigma_0}{\gamma_0} e^{i\delta} = G_0 + \eta i\omega. \tag{2.12}$$

Thus, for the Kelvin-Voight model, $G'(\omega) = G_0$, and $G''(\omega) = \eta\omega$. The Storage modulus is constant, but the Loss modulus is frequency dependent. At low frequencies the model is elastic and then there is a crossover at $\omega_c = G_0/\eta$ from being predominantly elastic to predominantly viscous, Fig. 2.8 (d).

Models can also be constructed by combining Maxwell and/or Kelvin Voight models either in series or in parallel. This allows for systems to have a spectrum of relaxation timescales which in the continuum limit is given by $H(\tau)$ where τ are timescales. Integrating $H(\tau)$ gives the relaxational modulus:

$$G(t) = \int_0^\infty \frac{H(\tau)}{\tau} e^{-t/\tau} d\tau. \tag{2.13}$$

There are several different response functions discussed here: $G(t)$, $J_c(t)$, $G^*(\omega)$, and this list is not exhaustive of all possible response functions. All of these response functions are interrelated in the linear regime, for example the complex modulus is the Fourier transform of the relaxational modulus. Which one you chose to measure depends on what

information you want from the system and also one which will be possible to measure. Some are easier to measure and/or interpret than others.

2.2.5 Large Amplitude Oscillatory Shear

For large amplitude oscillatory shear (LAOS) the stress is no longer linear with the applied strain. As such the stress can no longer be represented by a single sinusoid even though a sinusoidal strain is applied. In Fig. 2.9 (a) we see an example strain and stress. the strain is a single sinusoid but the resultant stress is not. To decompose the stress into an in-phase component and an out-of-phase component, $\sigma = \sigma' + \sigma''$, we now can use a Fourier series. Alternatively, we can represent the stress using Chebyshev functions of the 2nd kind, T_n [189],

$$\sigma'(t) = \gamma_0 \sum_{n \text{ odd}} G'_n \sin(n\omega t) = \gamma_0 \sum_{n \text{ odd}} e_n T_n(x), \tag{2.14a}$$

$$\sigma''(t) = \gamma_0 \sum_{n \text{ odd}} G''_n \cos(n\omega t) = \dot{\gamma}_0 \sum_{n \text{ odd}} v_n T_n(y), \tag{2.14b}$$

where $x = \gamma/\gamma_0$, $y = \dot{\gamma}/\dot{\gamma}_0$. We use the x and y normalization because the Chebyshev decomposition is only valid over $[-1, 1]$. The coefficients for the Fourier series are G'_n and G''_n, and the coefficients for the Chebyshev series' are e_n and v_n. The first few Chebyshev functions are show in Table 2.1, though it is only the odd functions that contribute. The stress is negative or zero when the strain is negative or zero and vice versa for positive strains. Since the even Chebyshev functions are even functions they do not contribute.

Table 2.1: Table of Chebyshev functions, T_n, and the recursion relation.

T_0	1
T_1	x
T_2	$2x^2 - 1$
T_3	$4x^3 - 3x$
$T_{n+1}(x)$	$2xT_n(x) - T_{n-1}(x)$

The practicality of the Chebyshev series is easiest to see when plotting the stress versus the strain or shear rate, Fig. 2.9 (b, c). Since $T_1(x) = x$, any deviation from linear of the stress is immediately captured by e_3 or v_3, the coefficients for $T_3(x)$. A positive e_3 describes an increase in stress above linear at the highest strains, this is in-cycle strain stiffening. In-cycle strain softening corresponds to negative e_3 where the stress is lowered at the highest strain. v_3 being positive describes in-cycle shear thickening where the stress increases at high shear rate. Negative v_3 describes in-cycle shear thinning where the stress decreases at high shear rate. In Fig. 2.9 (c) this is seen by the stress represented by the solid black line being lower than linear at large shear rate. The level of non-linearity as well as the type is then characterized by e_3/e_1 and v_3/v_1, to leading order, since e_1 and v_1 are always positive. In the linear regime $e_1 = G'$ and $v_3 = G''/\omega$.

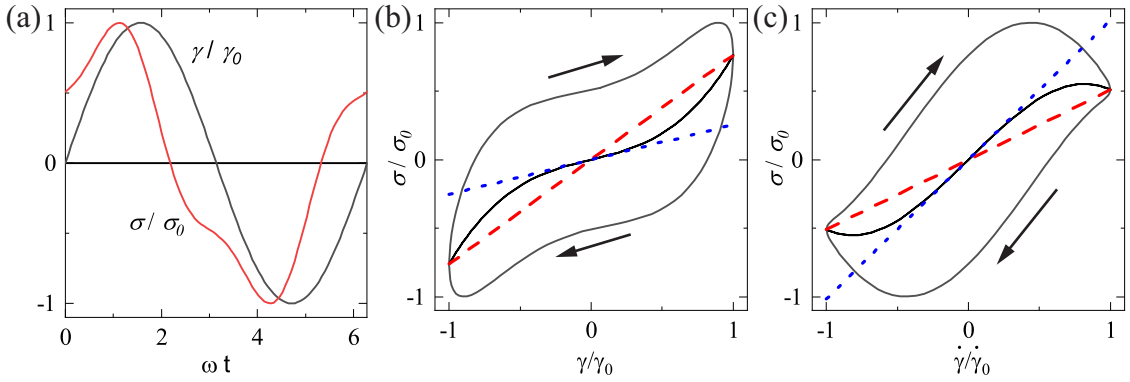

Figure 2.9: (a) Waveforms of the strain, $\gamma = \gamma_0 sin(\omega t)$, (black), and stress, $\sigma(t) = (1/\sqrt{2})sin(\omega t) + (1/\sqrt{2})cos(\omega t) - (0.2/\sqrt{2})sin(3\omega t) - (0.2/\sqrt{2})cos(3\omega t)$ (red) plotted versus dimensionless time, ωt. The level of nonlinearity for this system is $e_3/e_1 = 0.2$ and $v_3/v_1 = -0.2$. (b) The stress plotted versus the strain for the waveforms in (a). The black solid line is σ', the blue dotted line is G'_M, and the red dashed line is G'_L. (c) The stress plotted versus the shear rate for the waveforms in (a). The black solid line is σ'', the blue dotted line is η'_M, and the red dashed line is η'_L.

Because there is not a single slope for the in-phase component of the stress plotted versus the strain or the out-of-phase component of the stress plotted versus shear rate, we no longer have a single elastic modulus or a single viscous modulus. We now define two elastic moduli: the minimum strain elastic modulus, G'_M, and the large strain elastic modulus, G'_L. G'_M is the slope of the in-phase stress when the strain is zero, the blue dotted line in Fig. 2.9 (b). It can be found from either the Fourier or Chebyshev coefficients.

$$\begin{aligned} G'_M = \frac{d\sigma}{d\gamma}\Big|_{\gamma=0} = \frac{d\sigma}{dt}\frac{dt}{d\gamma}\Big|_{\gamma=0} &= \Big[\Big(\gamma_0 \sum_n G'_n n\omega \cos(n\omega t)\Big)\Big(\frac{1}{\gamma_0 \omega \cos(\omega t)}\Big)\Big]_{t=0} \\ &= \Big[\Big(\gamma_0 \sum_n e_n \frac{dT_n(x)}{dx}\Big)\Big(\frac{1}{\gamma_0}\Big)\Big]_{x=0}. \end{aligned} \tag{2.15}$$

The derivative of the Chebyshev functions is non-trivial to find a general relation for since the relation for T_n involves the previous two functions. Instead we can use the relationship between the Chebyshev coefficients and the Fourier coefficients. This is found from the identity: $T_n(\cos(\theta)) = \cos(n\theta)$. From here we find that $T_n(\sin(\theta)) = \sin(n\theta)(-1)^{(n-1)/2}$ [189].

Then from comparing terms in Eq. 2.14 we find that for n odd:

$$\begin{aligned} e_n &= G'_n(-1)^{(n-1)/2}, \\ v_n &= \frac{G''_n}{\omega}. \end{aligned} \tag{2.16}$$

and

$$G'_M = \frac{d\sigma}{d\gamma}\Big|_{\gamma=0} = \sum_{n\ \mathrm{odd}} nG'_n = \sum_{n\ \ odd} ne_n(-1)^{(n-1)/2}. \tag{2.17}$$

G'_L is the slope of the line connecting the stress at the minimum strain to the stress at the maximum strain. This is represented by the red dashed line in Fig. 2.9 (b).

$$\begin{aligned} G'_L = \frac{\sigma}{\gamma}\Big|_{\gamma=\pm\gamma_0} = \frac{\sigma(\gamma_0)-\sigma(-\gamma_0)}{2\gamma_0} &= \frac{\gamma_0 \sum\limits_{n\ \mathrm{odd}} G'_n \sin(n\frac{\pi}{2}) - \gamma_0 \sum\limits_{n\ \mathrm{odd}} G'_n \sin(n\frac{3\pi}{2})}{2\gamma_0} \\ &= \frac{\gamma_0 \sum\limits_{n\ \mathrm{odd}} e_n T_n(1) - \gamma_0 \sum\limits_{n\ \mathrm{odd}} e_n T_n(-1)}{2\gamma_0}. \end{aligned} \tag{2.18}$$

Using Eq. 2.16, we get that:

$$G'_L = \frac{\sigma}{\gamma}\Big|_{\gamma=\pm\gamma_0} = \sum_{n\ \mathrm{odd}} G'_n(-1)^{(n-1)/2} = \sum_{n\ \ odd} e_n. \tag{2.19}$$

We can also define two viscous moduli in a similar way from σ'' and the shear rate, with a minimum shear rate viscous modulus, η'_M, and a large shear rate viscous modulus, η'_L.

$$\eta'_M = \frac{d\sigma}{d\dot{\gamma}}\Big|_{\dot{\gamma}=0} = \frac{1}{\omega}\sum_{n\ \mathrm{odd}} nG''_n = \sum_{n\ \mathrm{odd}} nv_n(-1)^{(n-1)/2}, \tag{2.20a}$$

$$\eta'_L = \frac{\sigma}{\dot{\gamma}}\Big|_{\dot{\gamma}=\pm\dot{\gamma}_0} = \frac{1}{\omega}\sum_{n\ \mathrm{odd}} G''_n(-1)^{(n-1)/2} = \sum_{n\ \mathrm{odd}} v_n. \tag{2.20b}$$

We can then define the level of non-linearity by comparing G'_M to G'_L and η'_M to η'_L. In the linear regime, $G'_M = G'_L = G'$ and $\eta'_M = \eta'_L = G''/\omega$. Outside of the linear regime if $G'_L > G'_M$ the stress has increased above linear at large strains and so there is in-cycle strain stiffening. In-cycle strain softening has $G'_L < G'_M$. The level of elastic non-linearity,

S, is defined by $S = (G'_L - G'_M)/G'_L$ and is zero in the linear regime, positive for strain stiffening systems, and negative for strain softening. If we expand the moduli in terms of the Chebyshev coefficients,

$$S = \frac{G'_L - G'_M}{G'_L} = \frac{\sum\limits_{n\,\text{odd}} e_n - \sum\limits_{n\,\text{odd}} n e_n (-1)^{(n-1)/2}}{\sum\limits_{n\,\text{odd}} e_n} = \frac{4e_3 + ...}{e_1 + e_3 + ...} \sim \frac{e_3}{e_1}, \tag{2.21}$$

we can see that S is essentially determined by e_3/e_1 since e_3 is always less than e_1.

For the viscous moduli $\eta'_L > \eta'_M$ implies shear thickening since at large shear rates the stress is higher than liner and $\eta'_L < \eta'_M$ implies shear thinning. T is the level of viscous nonlinearity defined by $T = (\eta'_L - \eta'_M)/\eta'_L$ and is zero in the linear regime, positive for shear thickening systems, and negative for shear thinning systems. It is also proportional to v_3/v_1 for $v_3 \ll v_1$. Either S and T or e_3/e_1 and v_3/v_1 can be used to quantify the level of non-linearity in a system.

2.3 Description of the Rheometer

Experimental shear rheological measurements can be made using several different geometries: parallel-plate, cone-plate, Couette, and double Couette. These can be seen in Fig. 2.10 (a-d). Each has their own advantages and disadvantages. For both parallel-plate and cone-plate the strain is related to the deflection angle by $\gamma = R\phi/h$, the arc length divided by the height, with R the radius, ϕ the deflection angle, and h the height, Fig. 2.10 (e). For parallel-plate configurations the height is constant throughout the sample chamber; as such the strain is not constant throughout the sample and increases linearly with r, the polar coordinate. The edge strain is the conventionally reported strain because it is proportional to the torque [182, 184, 190]. Cone-plate configurations have a height that is dependent on r, $h = rsin(\beta)$, with β the angle of the cone, see Fig. 2.10 (b). The strain is then independent of position: $\gamma = \phi/sin(\beta)$. However, cone-plate configurations have a fixed sample volume whereas parallel-plate configurations can be put at an arbitrary height. This

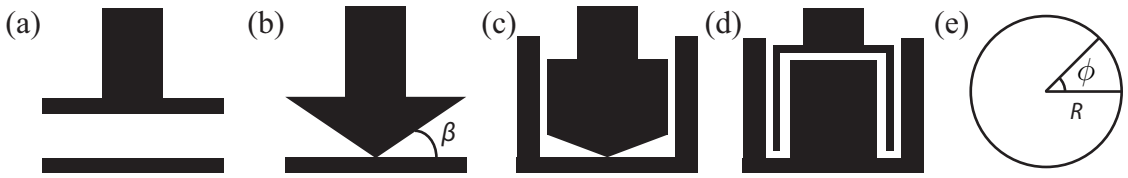

Figure 2.10: (a) Parallel-plate geometry. (b) Cone-plate geometry [191]. (c) Couette geometry. (d) Double Couette geometry. (e) Top view of the rheometer shwoing the radius of the top tool, R, and the angle of rotation, ϕ.

is an advantage of parallel-plate, as it allows for versatility in the types of samples that can be used. Couette and double Couette configurations are used with samples with small response functions. These two geometries have much higher surface areas and as such are more sensitive to small responses and so can measure smaller viscosities and elastic moduli. The disadvantage is that they require a larger, fixed sample volume.

For Couette and double Couette the stress is linear with the torque, T which is related to the surface area of the tool, $\sigma = T/(2\pi R^2 L)$, where $2\pi RL$ is the surface area of the cylinder [182, 184]. For Cone-plate and parallel plate geometries the torque is related to the stress via

$$T = \int_0^R \sigma(r) 2\pi r dr \cdot r, \tag{2.22}$$

and for linear response $\sigma(r) = (r/R)\sigma_{edge}$, with σ_{edge} being the stress at the edge of the top tool. Evaluating the integral we get that the torque is proportional to the stress at the edge of the top plate, $T = \sigma_{edge}\pi R^3/2$ [182]. Since the stress is taken over the entire sample out to the edge and the stress and strain are proportional in the linear regime, the maximum strain, i.e. the strain at the edge, is taken as the strain.

To investigate the mechanical properties of fire ant aggregations we use a parallel plate geometry in an Anton Paar MCR 501. The cone plate geometry has a gap at the bottom so that the top tool does not touch the bottom plate. Multiple particles in the sample need to be able to fit in this gap which is $\sim 50\ \mu m$. Since the ants are significantly larger than this we would have to move the top tool higher but the advantage of cone-plate having the same strain everywhere is only true if the tip of the cone essentially touches the bottom plate. As

such, we use a parallel plate geometry because ants have finite size they cannot fill a cone without gaps whereas by controlling the height we can leave the ants enough space to fill space.

The MCR 501 is a stress controlled shear rheometer which uses a feedback loop to approximate "true" strain control [192]. A torque is applied to the top plate with a brushless EC motor, the resultant rotation is measured with an optical encoder, and then the torque is updated. If this is done fast enough, the machine is able to replicate a strain control experiment.

Torque is applied using a brushless electronically commutated (EC) motor [193], Fig. 2.11 (a). Normally brushes are used to transmit current to electromagnets mounted to the shaft with the fixed magnets around the electromagnets, Fig. 2.11 (b). This has the advantage of not needing the electromagnets to be controlled electronically as they can be controlled mechanically by the contact patches controlling the electromagnets on the shaft. A brushless motor has the fixed magnets attached to the shaft and the electromagnets around them, Fig. 2.11 (b). This has the advantage of not adding any drag to the system as there are no brushes connecting the outer motor assembly to the shaft but has the disadvantage of needing the electromagnets to be externally controlled. The fixed magnets and the electromagnets interact causing torque on the shaft. The electromagnets currents are changed to control the torque applied to the shaft. The motor assembly can be seen in relation the encoder and bearings in Fig. 2.11 (e)(ii).

The position/ rotation sensor is a based around an optical encoder, Fig. 2.11 (c). It works by shining a light through the encoder and then using a photodiode detector on the other side of the encoder to read the changes in light intensity. The light bulb, lens, encoder, and detector can be seen in Fig. 2.11 (d) with the bulb on the bottom and the detector on the top. The lens focuses the light so that the area illuminated on the encoder is small which is how it is able to achieve an angular resolution of $0.012\ \mu rad$. The encoder can be seen in relation to the other components in Fig. 2.11 (e)(i).

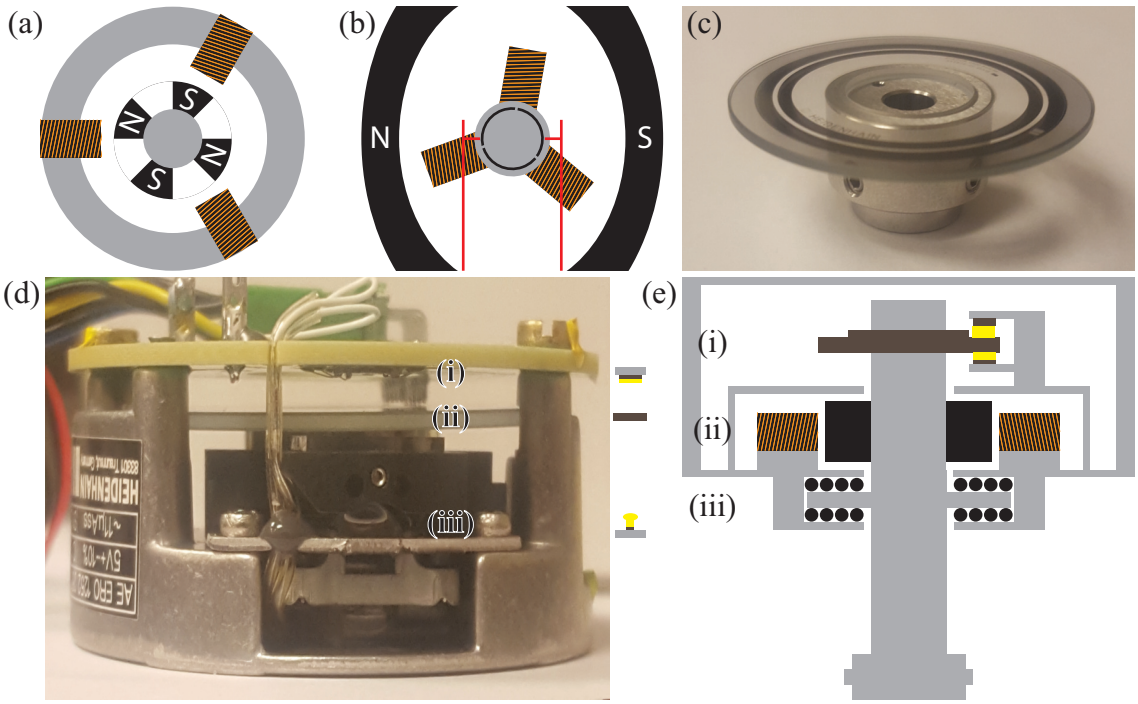

Figure 2.11: (a) Brushless EC motor. (b) Brushed electric motor. The brushes are in red. In (a), (b), and (e) the permanent magnets are black with white lettering and the electromagnets are represented by black with gold wire wrappings. (c) Optical encoder grating. (d) Optical encoder and reader. The light source (i) is on the bottom and the photo cell (iii) is above the encoder (ii). (e) Rheometer head assembly with: (i) The diffraction grating for position sensing, (ii) The brushless EC motor for applying torque, and (iii) The air bearings to support the system with minimal drag.

The fixed magnets, position sensor, and top plate are all supported by air bearings which keep drag to a minimum, Fig. 2.11 (e)(iii). The air for the bearing is provided by an oil free air compressor. We lower the dew point of the air by drying the air with an in-line desiccant dryer in order to prevent water from getting into the bearings and contributing to the drag. This lowers the dew point to $-60°C$. We regulate the output pressure so that it maintains the $85\ psi$ necessary for the air bearings.

For our experiments we use plates that are $50.0\ mm$ in diameter and we have made two major modifications to the rheometer that allow us to perform ant experiments. First, we add Velcro to both the top and bottom plates of the setup to allow the ants to grab onto it and ensure the no slip boundary condition [67]. The Velcro can be seen as black rectangles on the top and bottom plate in Fig. 2.12. The distance between the two plates is defined

by h_{plate}, Fig. 2.12 (a). The distance between the two pieces of Velcro is h_{Velcro}. Because Velcro is compressible having h_{Velcro} the same for two experiments does not guarantee that h_{plate} will be the same, however, this is not relevant as what we are sure about is having the same gap between experiments.

One of the assumptions made when making a rheological measurement is that the top of the sample is moving with the top plate and the bottom of the sample is fixed at the stationary bottom plate in our experiments [184, 185, 194]. For every rheological measurement, the no slip condition must be met for the measurement to have meaning [195]. To assure the no slip condition is met when using ants we have added Velcro to the top and bottom plates, Fig. 2.12 (c). Either the hook or the loop side can be used as the ants can grab either of them [68]. For either type of Velcro we are assured that the no-slip boundary condition is met because the ants can grab the Velcro with a force that is approximately 100 times their body weight [38, 173] and they also entangle with the Velcro as evidenced by having to forcibly remove ants from the Velcro after every experiment. Both of these together mean that the top and bottom of the ant aggregation adheres to the top and bottom plates, respectively.

In addition to being able to adhere to the surface the slip length must be small compared to the mean free path of the particles in the system. In molecular gases, this slip length is relatively large since the particle density is typically small in this case. In contrast, for molecular liquids, the slip length is comparable to the mean inter-particle distance, which is much smaller than in gases [195]. Since the ant aggregations in our experiments are dense, the mean distance traveled by an ant before it hits another ant is small. Hence, the slip length in these ant aggregations is also small. Based on the smallness of the ant mean free path and the adherence of the ants to the Velcro, assuming no-slip conditions at the rheometer plates is reasonable.

Second, we use a containment cylinder to keep the ants within the measurement space, Fig. 2.12 (b). These were made out of either glass or metal depending on whether we

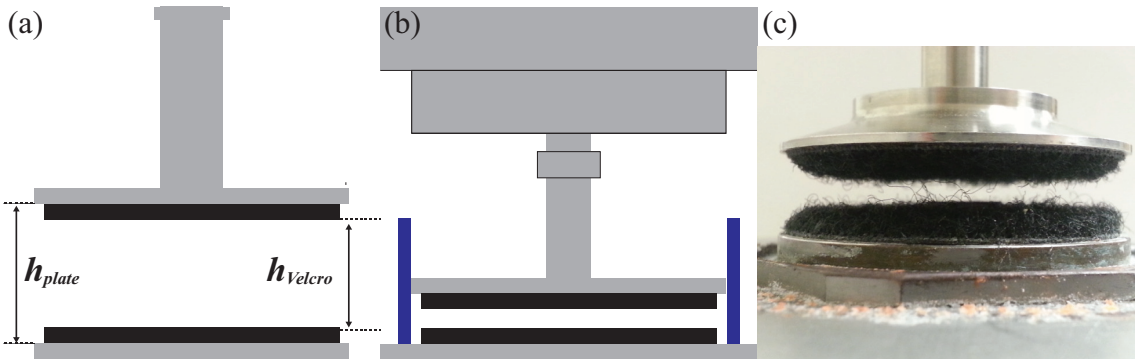

Figure 2.12: (a) Schematic of the experimental cell of the rheometer with parallel pate geometry and Velcro. The distance between plates is h_{plate}. The gap height is h_{Velcro}. (b) Sideview schematic overview of the rheometer including the containment cylinder and Velcro. The containment cylinder is blue. The Velcro is black in both (a) and (b). (c) Loop side Velcro on the top and bottom plate. $h_{Velcro} = 4.5\ mm$.

wanted to visualize the exterior ants or not. The metal cylinder has an inner diameter of $50.2\ mm$, and the glass cylinder is slightly wider with a diameter of $50.4\ mm$. This means there is an average gap between the top plate and the cylinder of $0.1\ mm$ for the metal cylinder and $0.2\ mm$ for the glass cylinder. Neither gap is large enough for ants to escape around the top plate. The Velcro is slightly smaller than the top plate with a diameter of $47\ mm$ but the threads overhang the edges of the Velcro on the loop side so that its effective diameter is larger than its attachment footprint and covers the plate, as seen in Fig. 2.12 (c). If fit to the plate the overhanging threads cause friction with the containment cylinder, reducing the sensitivity.

2.4 Limits of the Rheometer

To account for the modifications made to the system, calibration measurements were performed before each experiment. This was of particular importance because the Velcro changed from day to day from being pulled to get ants off and the subsequent trimming of the Velcro to remove stray fibers. Even the hook side changes slightly because of the process of taking the ants out of the rheometer. The Velcro is also compressible and its state can change form experiment to experiment.

To start an experiment the first step is to measure the motor inertia without the top tool in place. The rheometer does this by oscillating the at fixed frequencies and measuring the energy This prepares the rheometer for whichever top tool you are going to use.

2.4.1 Setting the Zero Gap

The next step is to add the top tool and reset the normal force. The normal force is the measured force along the shaft, in vertical direction with positive being upward. To measure normal forces generated by the sample it is necessary to subtract the weight of the top tool. We then measure the zero gap by moving the top plate down until it is in contact with the bottom tool and registers a normal force of $1\ N$.

To measure the influence of Velcro in our measurements, we first measure the normal force, F_N, as a function of plate-plate distance, shown in Fig. 2.12 (a), as we move the top plate down and subsequently up. This measurement is performed with both the hook side and the loop side of the Velcro. The hook side in Fig. 2.13 (a) shows no hysteresis and has a sharp slope once there is a measurable normal force. In contrast, results using the loop side of Velcro exhibit hysteresis, as shown in Fig. 2.13 (b). Note that the range of values of h_{plate} where we detect a measurable normal force is considerably larger in Fig. 2.13 (b), where we use the loop side of Velcro, than in Fig. 2.13 (a), where we use the hook side; this reflects that the loop side is fuzzier than the hook side and that it has strands sticking out into the gap between the plates. In addition, the larger normal force measured in Fig. 2.13 (b) as h_{plate} decreases compared to when h_{plate} increases, indicates that the Velcro gets compressed as the top plate moves down and does not fully decompress as the top plate is moved subsequently up. Whether we use the hook or loop side of Velcro, the zero gap is set when the normal force measured is $1\ N$. This corresponds to an h_{Velcro}, defined in the schematic in Fig. 2.12 (a), of zero. From these measurements, we see that vertical space occupied by the Velcro, when using its hook side is considerably smaller, than when using its loop side. By subtracting the value of h_{plate} when F_N is $1\ N$ and $0.1\ N$, we find that the

loop side of Velcro has an extent of $\sim 1.3\ mm$, while for the hook side it has an extent of $\sim 0.06\ mm$. This further confirms that the loop side is fuzzier than the hook side.

From the compression of the loop side of Velcro, we can further estimate a characteristic penetration depth of the ants into the Velcro. We do this by subtracting the value of h_{plate} in the descending and ascending curves in Fig. 2.13 (a) for $F_N = 0.1$ N, as this is representative of the largest amount the Velcro can compress, which we take as an estimate of the vertical space that might be available for the ants to penetrate through the Velcro. This distance is equal to ~ 0.5 mm. Since both the top and bottom plates have Velcro, the penetration depth is ~ 0.25 mm [67]. Similar results are obtained if we compare the values of h_{plate} for other values of F_N within the region where the hysteresis of the curves in Fig. 2.13 (b) is largest.

Importantly, we emphasize that irrespective of the side of Velcro we use, the gap is always set when $h_{Velcro} = 0$, which corresponds to a value of h_{plate} where $F_N = 1$ N. In addition, since we set the gap in every experiment, the amount of space available to the ants is always consistent even if the exact value of h_{plate} is not always identical.

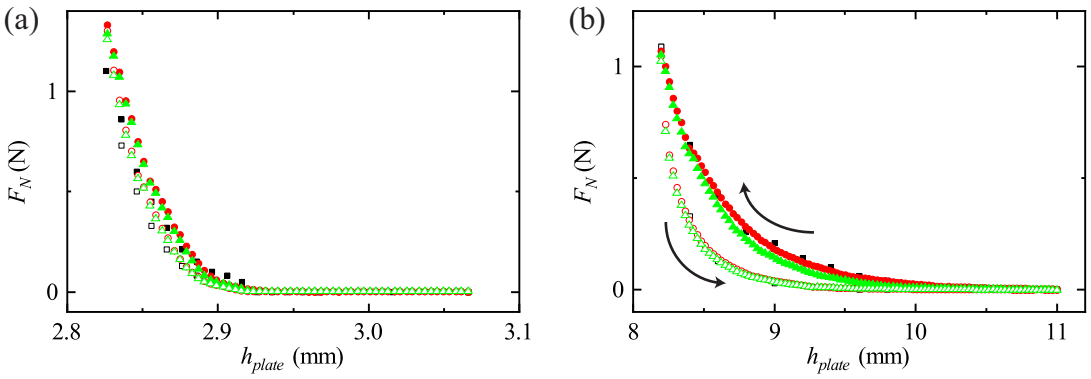

Figure 2.13: (a) Compressional test of hook Velcro. The closed symbols are descending and the open symbols are ascending. The black squares were first followed by the red circles and lastly the green triangles. (b) Compressional test of loop Velcro. The closed symbols are descending and the open symbols are ascending. The black squares were first followed by the red circles and lastly the green triangles.

2.4.2 Tool Inertia and Motor Calibration

The next step is to move the top tool up and measure its inertia. The inertia of the motor and of the top tool are used in determining how much torque to apply and in separating how much of the torque is needed to move the tool itself and how much is affecting the sample. We then calibrate the motor controller so that the electrical signal applied to the EC motor is set to a known motion of the top tool. The motor is a synchronous motor meaning that the motor shaft rotates at the same speed as the stator field, the electromagnetic field generated by the stationary electromagnets. The motor calibration adjusts the stator current, the current though the electromagnets, to be linear with the electromagnetic torque. This is done to improve the speed of response of the motor and to minimize overshoot of the applied torque [192]. Since the rheometer is designed to work with different top tools which have different inertias the electromagnets in the motor need to be tuned for each different top tool. Since the Velcro changes day to day we have to do this calibration for every experiment.

2.4.3 Torque Limits

Next, the containment cylinder is added to the setup and the top plate is moved into the measurement position in order to measure the torque limit for that day. Anton Paar quotes a torque limit of $0.1\ \mu Nm$ for steady-state experiments and $0.02\ \mu Nm$ for oscillatory experiments [192]; this sets the lower value of the torque where the signal to noise ratio is sufficiently high for the measurements to be reliable. However, with the modifications we have made, we expect a higher torque limit. To quantify this, we measure the torque required to rotate the tool at a constant angular frequency of $0.6\ r.p.m$ as a function of angle. We do this for two full revolutions and in the absence of sample. For the hook side of Velcro, we find the torque is less than $0.2\ \mu Nm$ and independent of whether the test is performed at $h_{Velcro} = 3\ mm$ or $h_{Velcro} = 4.5\ mm$, as shown with dashed and solid lines, respectively, in Fig. 2.14 (a). Hence the torque limit is comparable to what is expected for

the rheometer in the absence of our modifications. In contrast, for the loop side of Velcro, we find a torque limit of 3 μNm at $h_{Velcro} = 4.5\ mm$, and 20 μNm at $h_{Velcro} = 3\ mm$, as shown with solid and dashed lines, respectively, in Fig. 2.14 (b); these values are higher than the value expected in the absence of our modifications, reflecting that the dangling strands of the loop side of Velcro contribute to the torque appreciably. This contribution is more significant for smaller values of h_{Velcro}.

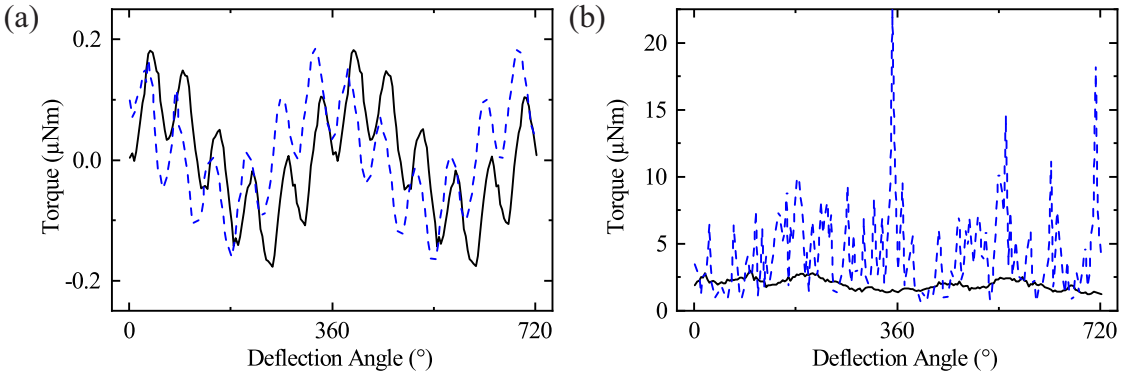

Figure 2.14: Torque as a function of deflection angle for (dashed blue) $h_{Velcro} = 3$ mm and (solid black) $h_{Velcro} = 4.5$ mm. (a) Hook side of Velcro. (b) Loop side of Velcro.

We then perform oscillatory rheology in the absence of sample by applying a small harmonic strain and measuring the resultant stress. We take the magnitude of the complex modulus, $|G^*|$, as an overall measure of the Velcro response. Frequency sweeps of the hook side of Velcro were beneath the torque limit, as expected. In contrast, frequency sweeps of the loop side at $h_{Velcro} = 3$ mm and $h_{Velcro} = 4.5$ mm, shown in Fig. 2.15 with open symbols, are above the torque limit. Note that $|G^*|$ is essentially frequency independent. For experiments with ants we will need to correct for the influence of the Velcro unless the response is significantly larger.

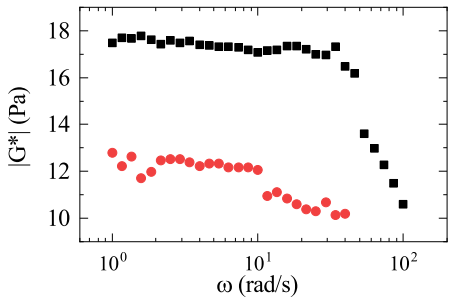

Figure 2.15: Complex modulus, G^*, measured with the loop Velcro for (black squares) $h_{Velcro} = 3$ mm and (red circles) $h_{Velcro} = 4.5$ mm, and with hook Velcro at $h_{Velcro} = 4.5$ mm. The hook side does not appear because the torque in these experiments was below the torque limit.

2.4.4 Post Experiment

After experiments, the ants are removed from the system, disentangled from the Velcro and returned to their colony. We make sure that for experiments done with living ants, they are still alive after the experiment. This is of particular importance since dead ants obviously are not active. Unless we are preforming a test with freeze killed dead ants, no ants die during experiments.

2.5 Effective Volume Fraction

We determine an effective volume fraction of the ant aggregation as, $\phi_{eff} = (N_{ants} * V_{eff})/V_{rheometer}$, with N_{ants} the number of ants, V_{eff} the effective volume of an ant, and $V_{rheometer}$ the available space in the rheometer. The number of ants is found from the mass of the aggregation and the mass of a single ant, $N_{ants} = m/m_{ant}$. The volume of the rheometer is given by, $V_{rheometer} = \pi R^2 h_{Velcro}$ and $V_{eff} = (4/3)\pi(\ell)^3$ with ℓ calculated from the inter-ant spacing taken when they are in their raft state at a density of $(0.20 \pm 0.04)\ g/cm^3$ [171]. If we then assume that at this density the ants are filling space at $\phi_{eff} = 0.64$, corresponding to random close packing [196], then $V_{eff} = 0.64\, m_{ant}/\rho_{raft}$

and

$$\ell = \sqrt[3]{\Big(\frac{3}{4\pi}\Big)\frac{0.64\, m_{ant}}{\rho_{raft}}}. \tag{2.23}$$

Putting in our value for the mass of an ant and the raft density gives $\ell = (0.8 \pm 0.1)\ mm$. This means the diameter of the sphere is about half the length of an ant. Combining all of these elements we get that

$$\phi_{eff} = \frac{N_{ants} V_{eff}}{V_{rheometer}} = \frac{(m/m_{ant})(\frac{4}{3}\pi l^3)}{\pi R^2 h_{Velcro}} = \Big(\frac{0.64}{\pi R^2 \rho_{raft}}\Big)\frac{m}{h_{Velcro}}. \tag{2.24}$$

Some example effective volume fractions and their corresponding densities and experimental parameters are show in Tab. 2.2.

Table 2.2: Effective volume fraction, density, and experimental parameters for some typical effective volume fractions.

ϕ_{eff}	ρ	$Mass$	$Height$
	g/cm^3	g	mm
1.1	0.34	3 2	4.5 3
1.6	0.51	3	3
2.2	0.68	4	3
3.3	1.02	6	3
4.4	1.36	8	3

2.6 2D Experiments

We can see visually what the exterior ants of an aggregation are doing by using a glass containment cylinder. However, to get an idea of what is happening inside we also look at two dimensional systems of ants. By confining the ants between two acrylic sheets separated by a distance equal to an ant height, $\sim 1.5\ mm$, we are able to visualize a 2D

cell containing a single layer of ants.

We define an effective area fraction $\phi_{s,eff} = N_{ants}\,\pi l^2/A_{cell}$, where $A_{cell} \approx 6500\ mm^2$ is the area of our 2D cell. The aggregation is illuminated either from below or above and imaged using a Sony Handycam CCD camera with a resolution of $1080x1440$.

CHAPTER 3
LINEAR OSCILLATORY RHEOLOGY

We begin our experimental study of the mechanics of ant aggregations by looking at their response to small amplitude oscillatory shear (SAOS). Strain sweeps tell us where the linear regime is while frequency sweeps tell us the frequency dependence of the viscoelastic properties. The frequency dependence reflects the microscopics of the system as the strain is small enough to not affect the system and so the information gleaned is from the system in "equilibrium". We can also see whether the mechanics change in time by monitoring the moduli as a function of time.

It is interesting to see if any of the rheological models presented in Chapter 2 will hold for ant aggregations since ants are not an equilibrium system. There have been studies done on the rheological properties of active matter before but they have been done primarily with cellular aggregates which are predominantly elastic and exhibit very slow dynamics [45, 58–60, 142, 143, 146]. Ants move at much shorter timescales and display both elastici, Fig. 1.2, and viscous behavior, Fig. 1.3. The question we address is what are the mechanical properties of an active system that clearly exhibits both viscous and elastic properties.

3.1 The Effect of the Velcro

We first need to determine to what extent the effects of Velcro are important and if we can separate out its response from the ant aggregation. We have measured the frequency response of the Velcro alone, Fig. 2.15, and we now perform this same measurement with ants in addition to the Velcro. The tests with ants at $\phi_{eff} = 1.1$ results in a $|G^*|$ that is at least an order of magnitude larger than what we measured in the absence of ants, as shown in Fig. 3.1 (a) with closed symbols.

From these measurements, we can then estimate the response of the ants by subtracting

the contribution from the Velcro, similar to the removal of the torque from the inertia of the top tool. We do this since the ants and the Velcro are both subjected to the same strain and can be treated as components of a composite system in parallel. The result is shown in Fig. 3.1 (b) and illustrates that there is essentially no influence of the Velcro, even for $h_{Velcro} = 3\ mm$, which is one of the smallest gaps we use in any of our experiments. We therefore conclude that what we measure in our rheology experiments is the response of the ant aggregation, without any significant influence of the Velcro.

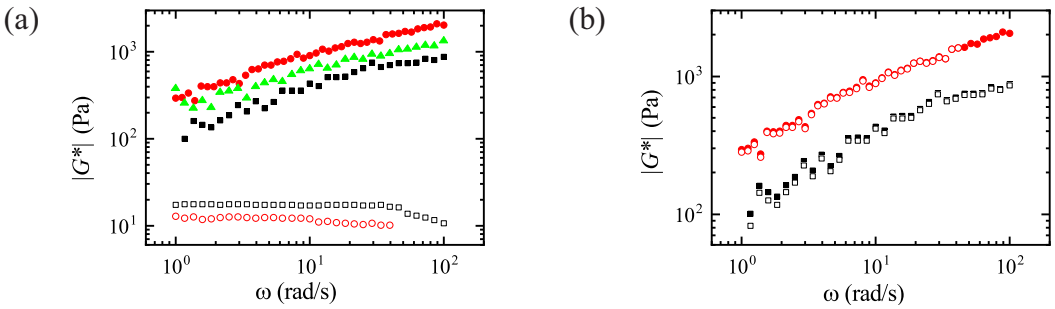

Figure 3.1: (a) Complex modulus, G^*, measured for ants with the loop Velcro for (black squares) $h_{Velcro} = 3$ mm and (red circles) $h_{Velcro} = 4.5$ mm, and with hook Velcro at $h_{Velcro} = 4.5$ mm. The open symbols are the corresponding measurements with only Velcro. The hook side does not appear because the torque in these experiments was below the torque limit. (b) Subtraction of the complex modulus of the Velcro by itself from the complex modulus of the combined Velcro and ants. The solid symbols are used for $G^*_{ants+Velcro}$, while the open symbols are used for $G^*_{ants+Velcro} - G^*_{Velcro}$. The circles symbols are for $h_{Velcro} = 4.5\ mm$, while the square symbols are for $h_{Velcro} = 3\ mm$. All experiments done at $\phi_{eff} = 1.1$.

3.2 Finding the Linear Regime

Now that we are certain that we can measure the rheological properties of the ants we need to find the linear regime. This is done either by performing a strain sweep or by looking at the Lissajous-Bowditch curves. To perform the strain sweep, we fix the frequency to $\omega = 1\ rad/s$ and perform oscillatory experiments with increasing γ_0. We find that for $\phi_{eff} = 1.1$, the linear regime is approximately fulfilled below $\gamma_0 \approx 0.04$, as shown in Fig. 3.2. Above this strain amplitude, both moduli decrease with increasing γ_0 reflecting the onset of the non-linear regime.

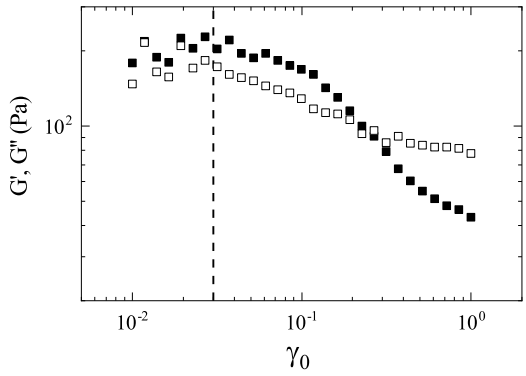

Figure 3.2: G' (closed) and G'' (open) as a function of strain amplitude, γ_0, for a constant frequency $\omega = 1\ rad/s$ and $\phi_{eff} = 1.1$. The cutoff at low strain amplitude was determined by the minimum torque limit in our experiments.

The strain and stress in a typical cycle for $\phi_{eff} = 1.1$ and experimental parameters $\gamma_0 = 0.01$ and $\omega = 1\ rad/s$ are shown in Fig. 3.3 (a). Both waveforms have been fit to $sin(\omega t + \delta)$, shown as solid lines. We can also plot this as a Lissajous-Bowditch curve, Fig. 3.3 (b), where we can see the elliptical shape indicative of a viscoelastic material probed in the linear regime, the solid line is the fit from Fig. 3.3 (a) replotted.

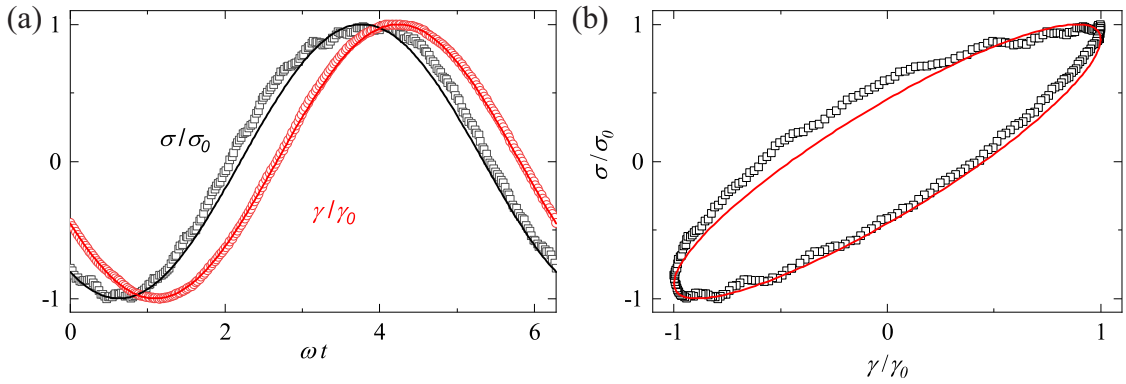

Figure 3.3: (a) Waveforms of the applied strain and measured stress from the linear regime of live ants at $\phi_{eff} = 1.1$ with the corresponding harmonic fits. They have been normalized with respect to corresponding amplitudes. From the fits of the raw waveforms we determine the elastic, G', and viscous, G'', shear moduli. (b) Lissjous-Bowditch plot of the waveforms in (a).

3.3 Frequency Sweeps with Live Ants

We then vary the frequency at a fixed strain amplitude of $\gamma_0 = 0.01$. We find that $G' \approx G''$ throughout the frequency range we are able to span experimentally, as shown in Fig. 3.4. This reflects that (i) the ant aggregation is viscoelastic and that (ii) the aggregation approximately equally stores and dissipates energy. This is markedly different from the behavior observed for other active materials. For example, flocks of birds and fishes are unable to support applied forces, and so simply flow in response to external perturbations [197, 198]. In this case, the birds or the fish are not able to link to each other but rather are always separated from one another. From this perspective, cell aggregations [199, 200] or active liquid crystalline materials [57, 201] could be thought of being closer in behavior to our ant aggregations, since their constituent building blocks are in direct contact with each other and also have the capability to reorganize and assemble into a wide variety of structures. However, once formed, cell assemblies are predominantly elastic, with little or no liquid-like response [142, 199], and active liquid crystals seem predominantly viscous, with a very weak solid-like response [202]. In contrast, we find that fire ant aggregations are characterized by equally important viscous-like and solid-like responses.

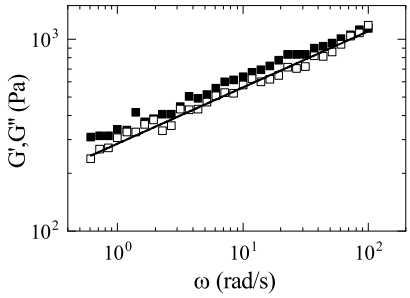

Figure 3.4: Frequency sweep of a live aggregation at $\phi_{eff} = 1.1$.

An additional striking feature of the frequency dependence of the shear moduli is that both G' and G'' scale with frequency as a power law within the frequency range probed: $G' \approx G'' \sim \omega^n$, with $n = 0.39 \pm 0.10$. This is very different from what one observes for a viscoelastic fluid with a single relaxation time as exemplified by the Maxwell model, as

shown in Fig. 2.8. In that case, the crossover between G' and G'' occurs at a frequency reflecting the structural relaxation time, λ, of the material. For $t \gg \lambda$, the material flows like a simple liquid, while for $t \ll \lambda$ the material responds elastically.

The ant aggregation is characterized by a G' that is equal to G'' at all accessible frequencies, which can be thought of reflecting the existence of many different relaxation mechanisms in the material or of no special relaxation time scale. Since the frequency dependence is power law we will postulate that the power spectrum will also be power law: $H(\lambda) \sim \lambda^{-n}$. From there we can calculate the relaxational modulus,

$$G(t) = \int_0^\infty \lambda^{-n} e^{-t/\lambda} \frac{d\lambda}{\lambda} = \Gamma(n)\, t^{-n}. \tag{3.1}$$

From there we can calculate the storage and loss modulus [182, 203],

$$G'(\omega) = \omega \int_0^\infty G(t) sin(\omega t) dt = \omega^n \, \frac{\pi}{2} csc(\frac{n\pi}{2}), \tag{3.2a}$$

$$G''(\omega) = \omega \int_0^\infty G(t) cos(\omega t) dt = \omega^n \, \frac{\pi}{2} sec(\frac{n\pi}{2}). \tag{3.2b}$$

Note that the power law exponent in the power spectrum is the same as the exponent in the moduli. The lack of a single relaxation is consistent with real space imaging, which reveals that ant aggregations exhibit a wide variety of relaxation mechanisms at different timescales: they constantly change the number of attachments with nearest neighbors, perform internal body motions and experience center of mass motion involving rearrangements with nearest neighbors as well as collective rearrangements [67, 173]. All of these motions are expanded by the different sizes of ants and the different activity levels of individual ants, leading to many possible relaxation mechanisms. Fire ant aggregations have many possible ways to relax stress and dissipate energy, ultimately reflecting their inherent activity and their out-of-equilibrium nature. We, nevertheless, note that we cannot rule out the

existence of a crossover between G' and G'', reflective of a long-time structural relaxation, at a frequency below those we are able to probe in our experiments.

3.3.1 Kramers-Kronig Relations

We can rationalize our result in the context of linear response theory with the Kramers-Kronig relations [204, 205], which links the in-phase and out-of-phase components of a response function in the frequency domain [194, 206, 207]. This connection is a result of causality and the physical impossibility of responding to a stress before the stress is actually applied. Mathematically, G' and G'' are then linked as [194]:

$$\frac{G'(\omega)}{\omega^2} = \frac{2}{\pi}\int_0^\infty \frac{G''(x)/x}{\omega^2 - x^2}dx. \tag{3.3}$$

Note that G' at one frequency reflects G'' at all frequencies. If we assume that both G' and G'' are power law as we have seen from experiment,

$$G'(\omega) = G'_c\omega^n \text{ and} \tag{3.4a}$$

$$G''(\omega) = G''_c\omega^m, \tag{3.4b}$$

then

$$\begin{aligned}\frac{G'_c\omega^m}{\omega^2} &= \frac{2}{\pi}\int_0^\infty \frac{G''_c x^n/x}{\omega^2 - x^2}dx, \\ &= G''_c\frac{2}{\pi}\int_0^\infty \frac{1}{\omega^2(1-(x/\omega)^2)}\frac{x^{n-1}}{\omega^{n-1}}\omega^{n-1}dx.\end{aligned} \tag{3.5}$$

Changing variables to $y = x/\omega$, with $dy = dx/\omega$,

$$\frac{G'_c\omega^m}{\omega^2} = G''_c\frac{\omega^n}{\omega^2}\frac{2}{\pi}\int_0^\infty \frac{y^{n-1}}{(1-y^2)}dy. \tag{3.6}$$

Since $\frac{2}{\pi}\int_0^\infty \frac{y^{n-1}}{(1-y^2)}dy = \cot(\frac{n\pi}{2})$, we finialy obtain:

$$G'_c\omega^m = G''_c\omega^n \cot(\frac{n\pi}{2}). \tag{3.7}$$

If additionally the exponents are the same, $m = n$, we find that the relationship between the coefficients of both moduli, and thus of the moduli themselves since the frequency dependence is the same,

$$\frac{G''}{G'} = \frac{G''_c}{G'_c} = \tan(\frac{n\pi}{2}). \tag{3.8}$$

Rearranging, we obtain

$$n = \frac{2}{\pi}\tan^{-1}(\frac{G''}{G'}). \tag{3.9}$$

The ratio of G' to G'' then provides an alternative way to calculate n. As an example we do this point-by-point with the oscillatory data for $\phi_{eff} = 1.1$ and obtain $n = 0.46 \pm 0.02$, consistent with the result obtained from the fits of G' and G'' with ω, Fig. 3.5. Furthermore, since in our experiments, $G' \approx G''$, indicating congruence, the Kramers-Kronig relations require $n = 0.5$, consistent also with what we find experimentally.

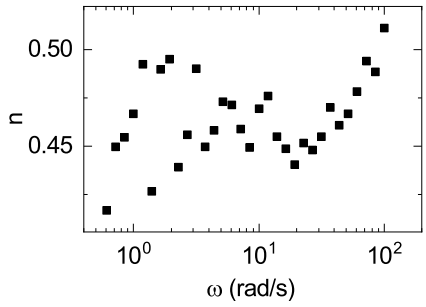

Figure 3.5: n calculated point by point for the frequency sweep done at $\phi_{eff} = 1.1$ in Fig. 3.4.

Interestingly, the observed power law behavior is reminiscent of what is seen for colloidal gels, which are made of small Brownian particles, which in the presence of attractive forces and at high enough concentration, aggregate and eventually percolate through the sample, resulting in a kinetically arrested colloidal gel. Near the gelation point, the elastic

and viscous moduli can both exhibit power law behavior with frequency [208]. This is also seen for polymer gels, where at the critical gelation point both moduli can in addition be comparable in magnitude [60, 209, 210], similar to what we observe for our ant aggregation.

3.3.2 Fractal Nature of the Aggregation

While the power-law behavior of polymer gels at the critical point can be traced back to the fractal structure of the system [211], real space analysis of two-dimensional ant aggregations, as well as of frozen three-dimensional aggregations of live ants analyzed using micro scale computed tomography [167], suggest that the structure of ant aggregations is not fractal.

We quantify the potential fractal structure of the 2D aggregation using the box counting method. For this we take an image of a 2D system of ants and binarize it, to clearly distinguish between the ants (black) and the background (white) pixels, Fig. 3.6 (a). We then take boxes of varying sizes and find the number of boxes it takes to cover every ant. The boxcounting fractal dimension, D, is found from $N_{boxes} \sim l_{box}^{-D}$. For the aggregation shown in Fig. 3.6 (a), D is 2 for boxes larger than $0.66\ mm$, Fig. 3.6 (b). Having a fractal dimension of 2 in 2D implies the system is homogeneous and is not fractal. Below $l_{box} = 0.66\ mm$, $D = 1.75$. However, in this case the boxes are smaller than individual ants, so this dimension does not reflect anything of the aggregation.

For the 3D system we look at $g(r)$ to see if there is a spatial fractal. We calculate $g(r)$, using Eq. 1.1, for a 3D ant aggregation using the center of mass of the ants, obtained from micro CT experiments [173]. The center of mass data is shown in Fig. 3.6 (c) where we can see that the ants fill a space of roughly $1\ cm^3$. $g(r)$ is shown in Fig. 3.6 (d) where we can clearly see that $g(r)$ is not consistent with power law behavior.

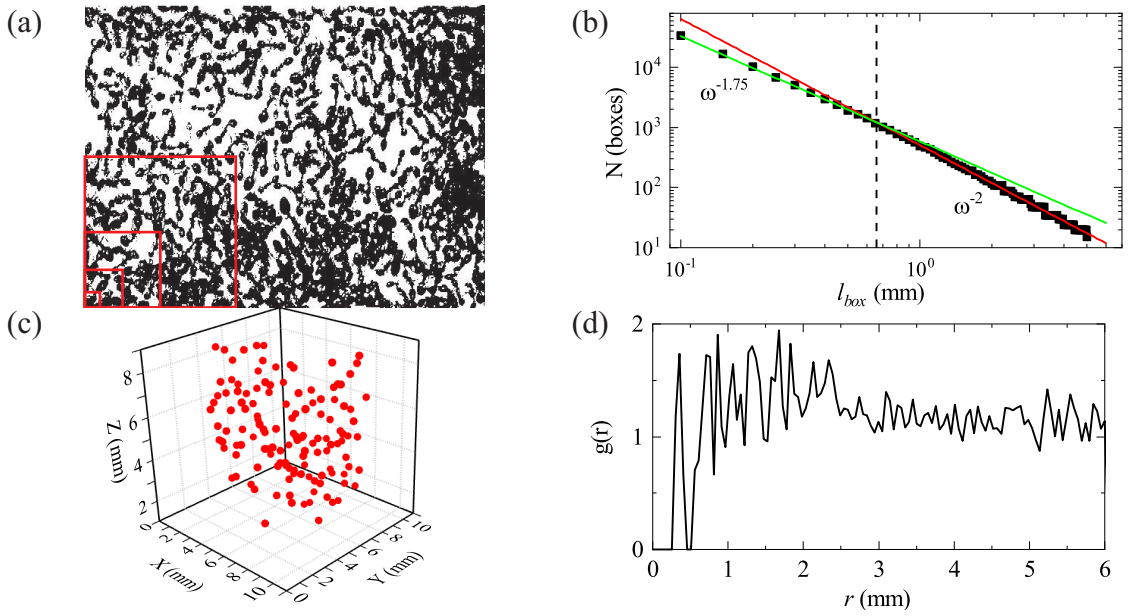

Figure 3.6: (a) Binarized image of ants in 2D. Image is 20 mm by 26 mm. (b) Box accounting plot for the image in (a). For boxes above 0.66 mm^2, the number of boxes scales as l_{box}^{-2}. (c) Center of mass positions of a 3D ant aggregations. Data from Foster et al. [173]. (d) $g(r)$ of the ant aggregation in (c). There is a nearest neighbor peak at 0.5 mm.

Since we see that the ant aggregation is not fractal in space but we see power law rheology, both G' and G'' and the underlying $G(t)$ and $H(\lambda)$ the lack of characteristic scale might result from the dynamics rather than from the structure. The activity of the ants shows itself through movement at many timescales. These many timescales per ant and the aggregation polydispersity, which results in many timescales for ant rearrangement events might then imply no intrinsic timescale in the system within the frequency range probed in our experiments.

3.3.3 Frequency Sweeps with Dead Ants

In contrast, dead ants at $\phi_{eff} = 1.1$ show only weak frequency dependence of the moduli. For these experiments, we freeze a live ant aggregation in a bin using liquid nitrogen [173] and then load it into the rheometer and perform the oscillatory shear experiments in the linear regime. We find that the elastic modulus is always greater than the loss modulus and that both are mostly frequency independent, Fig. 3.7 (a). There is a non zero loss modulus

because of the unstable nature of the pile of dead ants after being loaded into the rheometer. We measure the aggregation immediately after loading the dead ants so any perturbation of the system causes the dead ants to shift and settle leading to a measurable loss modulus.

We can again calculate the exponent from Eq. 3.9, shown in Fig. 3.7 (b). The exponent has an average value of (0.22 ± 0.01) which is half of what it was for live ants. This is another indication that the aggregation is more solid like, since n not only determines the frequency behavior but also G'/G''.

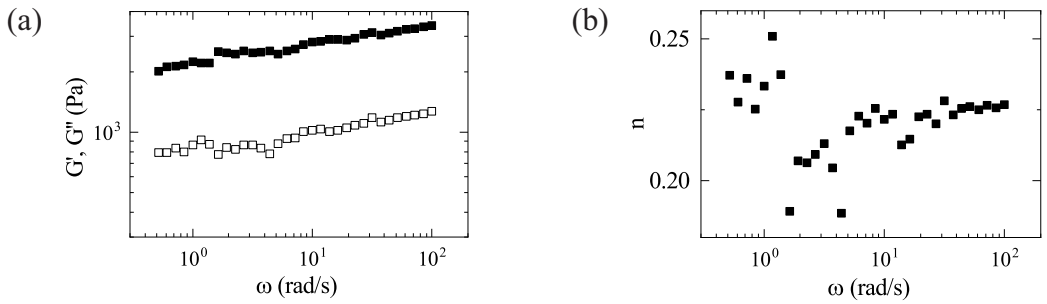

Figure 3.7: (a) Frequency seep of a dead aggregation at $\phi_{eff} = 1.1$. (b) n calculated point by point for each point in (a) using Eq. 3.9.

3.4 Activity Cycles

We now monitor the moduli as a function of time. We do this because we now that ant behavior is not constant in time [162–165] and we are interested in how the level of activity could change the mechanical properties of the aggregation. We have found that $G' \approx G''$ when the ants are active but the moduli separate, $G' > G''$ and then return together again. This happens a few times during the duration of the experiment, Fig 3.8 (a). Vertical lines have been drawn at the locations where the moduli are together.

The mechanical properties of the aggregation correlate with the normal force. The normal force is measured by the rheometer upward from the top plate, thus a positive normal force means that the aggregation would like to expand and is pushing upwards on the top plate. We see a correlation between the linear response of the aggregation and the normal force as a function of time, Fig. 3.8 (a,b). The loss tangent, G''/G', is close

to 1 when the normal force is large, Fig. 3.8 (b). This indicates that the moduli are of comparable value when the normal force is large.

We can also perform short oscillatory rheology measurements in the linear regime right after loading the ants in the rheometer and then later on, at times corresponding to low normal force. When there is high normal force, we find that $G' \approx G''$, and that both approximately scale as $\omega^{1/2}$ within the experimental frequency range of the experiment, Fig. 3.8 (c), consistent with Fig. 3.4. In contrast, when F_N is small, we find that $G' > G''$ and that G' is nearly frequency independent, Fig. 3.8 (d), similar to dead ants. The ant aggregation approximately equally dissipates and stores energy when F_N is large, and it is predominantly elastic and exhibits solid-like behavior when F_N is low.

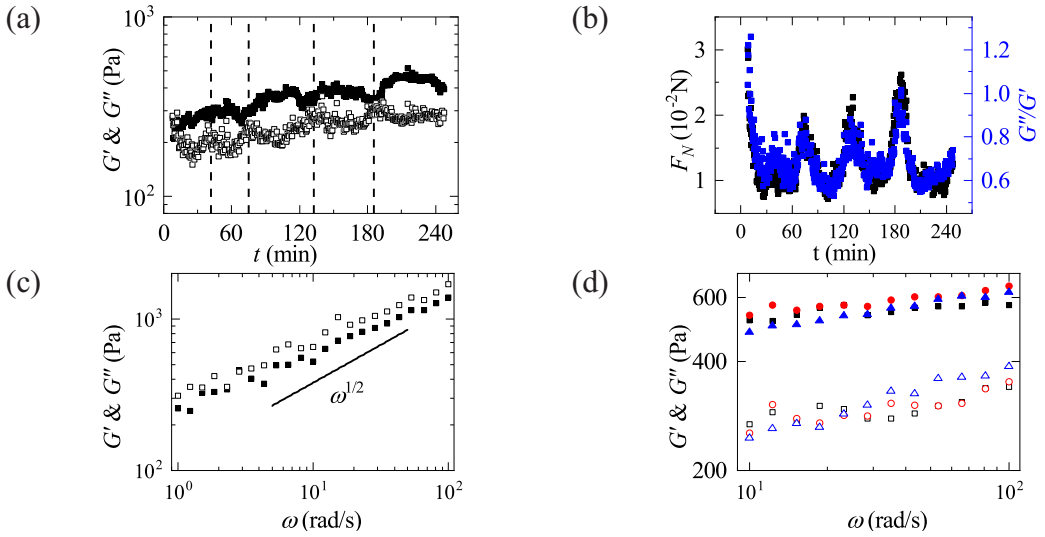

Figure 3.8: (a) Storage and loss moduli as a function of time at $\phi_{eff} = 1.1$ for $\gamma_0 = 0.01$ and $\omega = 10$. (b) Normal force versus time from the experiment in (a). (c) Frequency sweep immediately after loading the ants in the rheometer when the normal force is high. (d) Three representative frequency sweeps taken when the normal force is low.

3.4.1 Visualization

to further inquire about the behavior observed in time, we visually monitor the outside of the ant aggregation in our rheology experiments by using a glass containment cylinder and a CCD camera. We do this as the aggregation goes through a transition from low to high

normal force. Fig. 3.9 (a) is a snapshot corresponding to low normal force while Fig. 3.9 (b) is a snapshot corresponding to high normal force. Though in the images it is hard to tell them apart, by following the dynamics, it is possible to see there is difference in activity by looking at the movement of the antenna that make it through the gap between the top plate and the containment cylinder as well as in the motion of the ants next to the containment cylinder.

F_N for this peak is shown in Fig. 3.9 (c) with arrows indicating where the images in (a) and (b) were taken. The peak in F_N corresponds to a high level of activity, which we identify with an appreciable degree of motion in the video.

To further confirm that the F_N cycles reflect cycles in the overall motion of the ant aggregation, we visualize an ant aggregation confined within a two-dimensional cell. Consistent with the observations through the glass containment cylinder,we see that the aggregation goes through cycles where nearly all or nearly none of the ants move. Representative examples of these two situations are shown in Fig. 3.10 (a-d). In Fig. 3.10 (a,c), most of the ants are inactive and form high density clumps that percolate through the sample. Around these clumps, there are regions of low density, moving ants. Hence, the system in this case exhibits both static and dynamic heterogeneities. In contrast, in Fig. 3.10 (b,d), most of the ants are moving and thus the ant aggregation is extremely active. In this case, the system is much more homogeneous, both statically and dynamically. Importantly, once a peak in activity has passed, the clumps of ants appear in different regions within cell, indicating that the cell walls or other experimental details are not affecting the observed behavior and that it is rather an effect that is intrinsic to the aggregation itself.

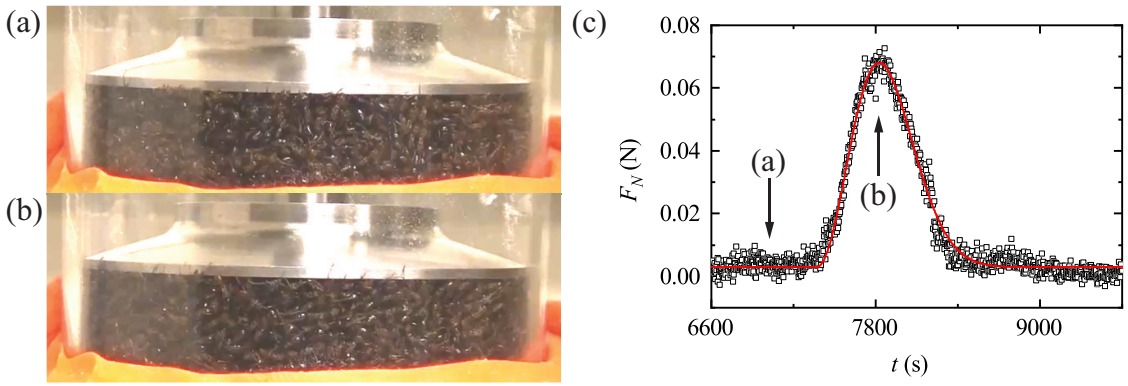

Figure 3.9: (a,b) Ant aggregation at $\phi_{eff} = 1.1$ with low normal force (a), and high normal force (b) viewed through a glass containment cylinder. (c) A single normal force peak. The images in (a,b) are indicated with arrows. The solid red line is a fit to Eq. 3.17b with R and k_a as fitting parameters.

To quantity the changes as the aggregation goes through these activity cycles, we binarize each image using a cutoff value of intensity, and classify each pixel as either part of an ant or not part of an ant; this is shown with black and white, respectively, for one of the snapshots in Fig. 3.10 (e). We also quantify a local density by course graining the image into boxes which are $30\ px$ by $30\ px$ whose value is the average value of the pixels inside. This is shown in Fig. 3.10 (f).

We then determine the time-dependence of the number of black pixels divided by the total number of pixels, which we identify with the area fraction, ϕ_s, occupied by the ants, Fig. 3.11 (a). Similarly to what we found in the rheology experiments, we also observe peaks in this graph. The peaks correspond to situations where the ants are active and the aggregation is most homogeneous, with the ants occupying the largest amount of available space. When most of the ants are inactive, the aggregation is heterogeneous, and the effective area occupied by the ants is small relative to the peak value.

We also calculate an average ϕ_s for each box in an image, Fig. 3.10 (f), and use it to determine a relative-mean-square fluctuation ($RMSF$),

$$RMSF(t) = \left\langle \left(\frac{\phi_s(t) - \overline{\phi_s}}{\overline{\phi_s}} \right)^2 \right\rangle_{allboxes}, \tag{3.10}$$

where $\phi_s = [\Sigma_{t_1}^{t_2}\phi_s(t)]/N$, with N being the number of points in the time interval $\Delta t = t_2 - t_1$, is a moving average that accounts for the fact that the relevant ϕ_s average changes in time as the aggregation moves through the observed activity cycles and for the fact that the clumps formed in the inactive parts of the cycles do not return to the same location after an active period. The value of the $RMSF(t)$ thus provides a measure of the overall activity of the ant aggregation. We use $\Delta t = 480\ s$. Considering smaller values of Δt does not qualitatively affect our results. In contrast, for larger values of Δt, we do see that the qualitative features of the results change. In this case, the ϕ_s average mixes active and inactive periods and is not representative of either of them.

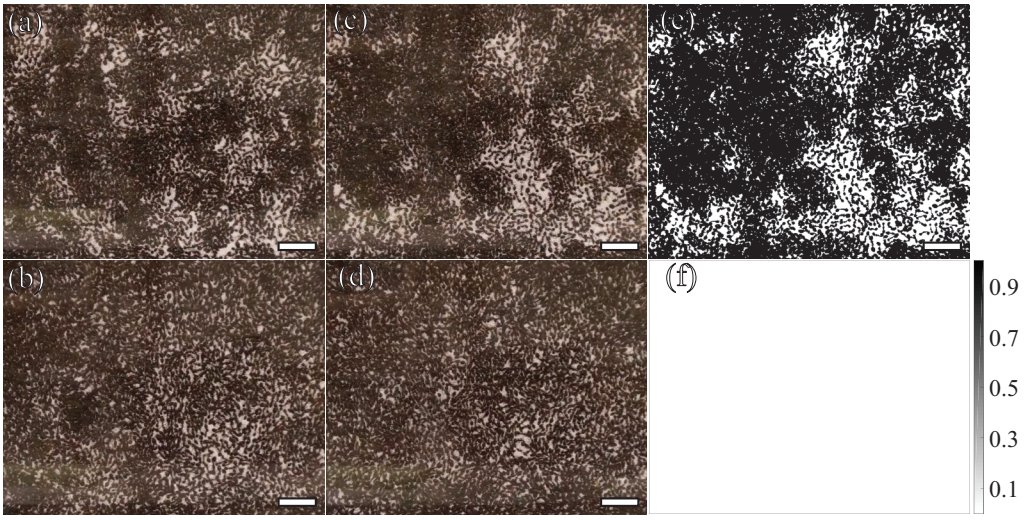

Figure 3.10: Visualization experiments using a two-dimensional apparatus constructed from three stacked sheets of acrylic with a hole cut in the center sheet for the ants. (a-d) Snapshots taken with a CCD camera at different times after loading the ants inside the cell. (e) Binarized version of image (d). Once each image in the timeseries is binarized, the fraction of black pixels, which we take to represent the area fraction occupied by the ants, is found for each image. The scale bar in (a-e) corresponds to 10 mm. (f) Local density, boxes are $30\ px$ by $30\ px$.

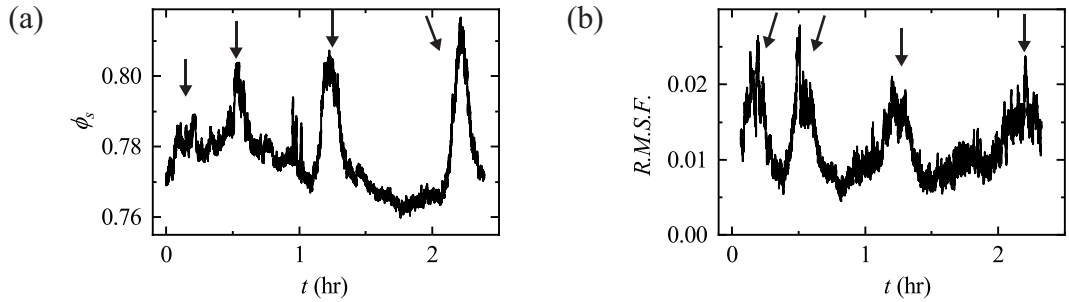

Figure 3.11: (a) Area fraction as a function of time. The snapshots Fig. 3.10 (a-d) correspond to 50min, 1hr 15min, 1hr 45min and 2hr 15min in (a). (b) Average root mean square fluctuations as a function of time.

We then see that activity correlates with the spatial ant-distribution, the normal force, and the mechanical properties of the ant aggregation. A high number of active ants means that the aggregation is spatially homogeneous, that the aggregation is approximately equally solid-like and liquid-like, and that the normal force is high. An aggregation with low number of active ants is more heterogeneous, more solid-like, and generates a lower normal force.

We emphasize that the origin of the spontaneous activity cycles we see are unknown. Known cycles include the day/night cycle [166], the sleep cycles of ants [162], and the "laziness" of some ants [212–214]. The period associated with these cycles do not coincide with what we see in our experiments. Whatever the reason, they nevertheless imply that the activity level of fire ants is not constant, thus enabling quantifying how activity affects the material properties of the aggregation.

3.4.2 Kinetic Model

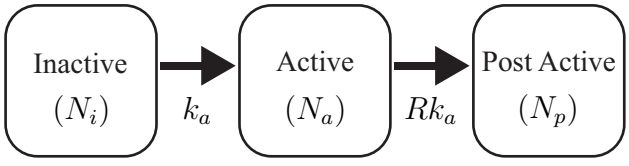

Figure 3.12: Block diagram of the kinetic model for ant activation.

Since all our observations can be traced back to the number of active ants in the system, we construct a kinetic model based on the number of inactive, active, and postactive ants, N_I, N_a, and N_p respectively. The model is meant to describe the behavior before, during, and after, a peak in the normal force. Inactive ants become active with rate constant, k_a, and active ants become postactive with rate constant, Rk_a. The process is one directional and all ants start out inactive. A block diagram of the model is shown in Fig. 3.12. We assume the time-rate of change of ants moving from the inactive state to the active state is proportional to the number of inactive ants. Hence:

$$\frac{dN_I}{dt} = -k_a N_I. \tag{3.11}$$

We also assume that the rate at which ants become postactive is proportional to the number of active ants. As a result:

$$\frac{dN_p}{dt} = +Rk_a N_a. \tag{3.12}$$

Finally, the number of active ants changes as inactive ants become active and active ants become postactive. Hence:

$$\frac{dN_a}{dt} = +k_a N_I - Rk_a N_a. \tag{3.13}$$

Note that

$$\frac{dN_I}{dt} + \frac{dN_a}{dt} + \frac{dN_p}{dt} = 0, \tag{3.14}$$

implying that the total number of ants, $N_I + N_a + N_p = N$, is constant. Solving the system with all ants being inactive at $t = 0$, that is $N_I(0) = N$ and $N_a(0) = N_p(0) = 0$, gives:

$$N_I(t) = Ne^{-k_a t}, \tag{3.15a}$$

$$N_a(t) = N\frac{e^{-k_a t} - e^{-Rk_a t}}{R-1}, \tag{3.15b}$$

$$N_p(t) = N(1 - \frac{Re^{-k_a t} - e^{-Rk_a t}}{R-1}). \tag{3.15c}$$

As an example, we plot $N_I(t)$, $N_a(t)$ and $N_p(t)$ in Fig. 3.13 (a) for $R = 2$ and $k_a = 1$. Notably, the model predicts a sharp turn on, corresponding to a sharp increase in the number of active ants; see solid curve in Fig. 3.13 (a). At some point, N_a peaks and subsequently, at longer times, it decreases, but it does so at a much lower rate compared to the initial increase. At this point, N_I is significantly smaller than $N_I(0)$, while N_p is significantly larger than $N_p(0)$. Both the number of inactive and postactive ants exhibit a monotonic behavior. Overall, the model predicts an asymmetry of the peak in N_a that is not seen in the normal force measurements; F_N is characterized by a rather symmetric shape [see Figs. 3.8 (b) and 3.9 (c)]. The symmetry persists irrespective of the values of R and k_a.

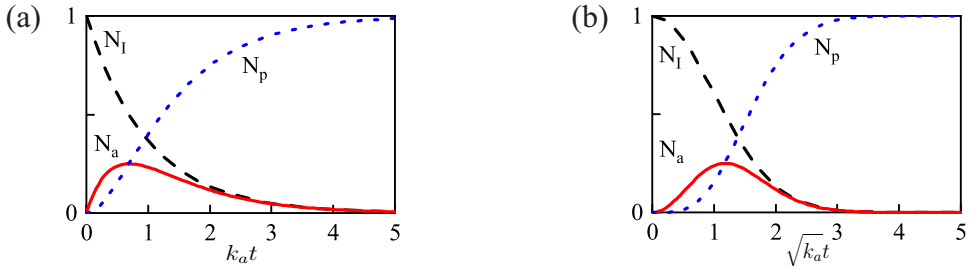

Figure 3.13: (a) Number of inactive ants, N_I, active ants, N_a and postactive ants, N_p, as a function of time in the fixed rate-constant model given by Eqs. 3.15, with $k_a = 1$ and $R = 2$. (b) N_I, N_a and N_p, as a function of time in the time-dependent rate-constant model given by Eqs. 3.17, with $k_a = 1$ and $R = 2$. In both plots, N_I is the black dashed line, N_a is the solid red line, and N_p is the blue dotted line. The results are all normalized by the total number of ants, N.

To account for the observed symmetry in the F_N peak, we consider that the rate of turn on is not constant in time. Instead, we assume that as more and more ants change from inactive to active, the rate of change increases. This is accounted for, in the simplest way possible, by changing the rate constant from k_a to $k_a t$. Note that we also include this

change in the turn off, since as more ants become active, more can also become postactive. The new set of differential equations then becomes:

$$\frac{dN_I}{dt} = -k_a t N_I, \tag{3.16a}$$

$$\frac{dN_a}{dt} = +k_a t N_I - R k_a t N_a, \tag{3.16b}$$

$$\frac{dN_p}{dt} = +R k_a t N_a. \tag{3.16c}$$

Taking the same initial conditions as before, the solutions are:

$$N_I(t) = N e^{-\frac{1}{2}k_a t^2}, \tag{3.17a}$$

$$N_a(t) = N \frac{e^{-\frac{1}{2}k_a t^2} - e^{-\frac{1}{2}k_a R t^2}}{R-1}, \tag{3.17b}$$

$$N_p(t) = N(1 - \frac{R e^{-\frac{1}{2}k_a t^2} - e^{-\frac{1}{2}k_a R t^2}}{R-1}). \tag{3.17c}$$

As before, we plot $N_I(t)$, $N_a(t)$ and $N_p(t)$ in Fig 3.13 (b) for $R = 2$ and $k_a = 1$. In this case, the change in rate constant lowers the rate of initial turn on, making the peak much more symmetrical. A fit of the F_N peak shape to this model, shown in Fig. 3.9 (c), with k_a and R as fitting parameters, correctly describes the data. From the fit, we obtain $R = 1.00 \pm 0.05$ and $k_a = (9 \pm 2) \cdot 10^{-6}\ s^{-2}$. Furthermore, from the value of k_a, we can obtain a characteristic timescale, $k_a^{-1/2} \approx 6\ min$, which is comparable to the typical peak width in our experiments, which have a full width at half max of $(10 \pm 2)\ min$. The value of $R \approx 1$ indicates that the rate of transition from inactive to active is the same as that from active to postactive; we find this is true for every peak we have analyzed.

3.4.3 Discussion of Activity Change

The change of properties occurs spontaneously as the ants undergo activity cycles. This behavior is inherent to the aggregation and is not affected by changing the Velcro; it seen for both the loop side and the hook side. It is not affected by changing the amount of air available by either blowing more air in or covering the top to prevent air from going in. It is also not affected by performing the measurement with different numbers of ants at the same effective volume fraction.

Our model supports the idea that the material properties of fire ant aggregations change based on the number of active ants. Depending on this number, the aggregation can predominantly store energy or approximately equally store and dissipate energy. The aggregation state can be monitored with rheology and it is reflected in the normal force. When most ants are inactive, the normal force is low and the density becomes locally heterogeneous. When most ants are active, the normal force is high and the aggregation density is homogeneous. The transition between these two states is not linear and depends on the number of currently active ants that are able to activate inactive ants. This is accounted for with a rate of activation, $k_a t$, that is linear in time. We have also tried changing k_a to $k_a N_a$ to implement a density dependence but the result is a symmetric peak, Fig 3.14.

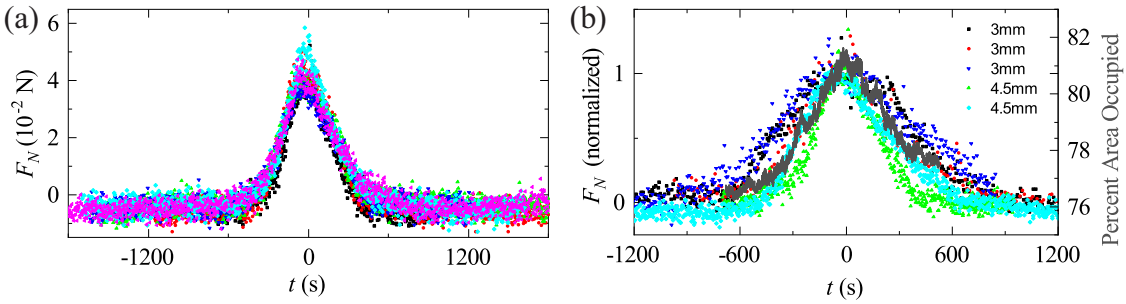

Figure 3.14: (a) Six peaks from one experiment shifted so that the center of each peak is overlaid. (b) Normal force peaks from three colonies at $h_V elcro = 3\ mm$ and at $h_V elcro = 4.5\ mm$. The solid line a peak in area fraction from a 2D experiment. All peaks have been shifted and normalized in order to compare peak shape.

Moreover, the normal force peak shape is consistent within each experiment. This can

be seen in Fig. 3.15 (a) where all of the peaks from Fig. 4.8 (c) have been shifted so that they overlay. The rate of turn on and turn off for active ants does not change over time for an individual aggregation since these rates are related to the shape of the peak in the normal force and that does not change within each experiment. We can also compare the shape of normal force peaks between experiments. Figure 3.15 (b) shows normal force peaks from experiments at $\phi_{eff} = 1.1$, three at $h_{Velcro} = 3\ mm$ and two at $h_{Velcro} = 4.5\ mm$. The solid line is a peak in the activity from the 2D apparatus shown in 3.11. Here we see that the peak shape in the normal force is similar throughout. From analyzing 22 peaks from four different ant colonies, we find that the peaks are characterized by a standard deviation of $(2.9 \pm 0.7) \times 10^2\ s$. We also calculate the skewness of the peaks, s, which is a measure of their symmetry with respect to the mean. For a Gaussian peak, which is symmetric about the mean, $s = 0$. We find an average skewness of $s = 0.1 \pm 0.2$, reflecting the high level of symmetry of the F_N peaks in our experiments. This further highlights that the proportion of active ants is the important feature of the activity peaks since the shape and hence the rates of turn on/off are similar across experiments.

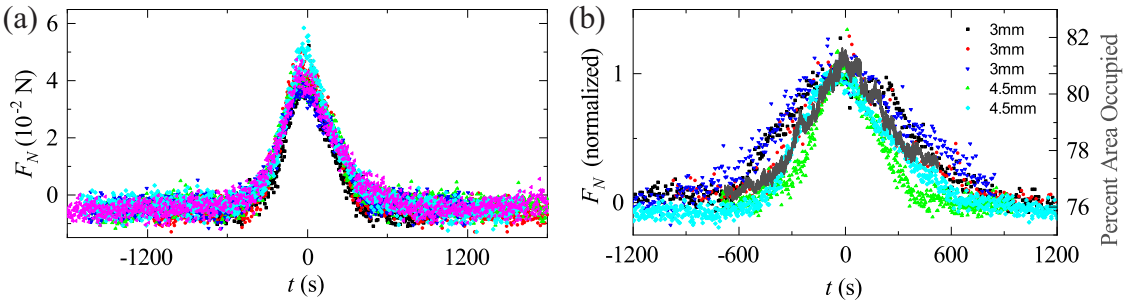

Figure 3.15: (a) Peaks from Fig. 4.8 (c) shifted to be centered on zero. this was done by fitting each peak to Eq. 3.17b with $t \to (t - t_0)$, we then shift each peak by its respective t_0. (b) Peaks from different experiments shifted to be centered on zero and normalized by the maximum value. One peak in activity from the 2D system is also included to exemplify that the peak shape is a product of the activity.

We also find that the spacing between the peaks is consistent across experiments with a time between peaks in activity of $58 \pm 20\ min$. This is not affected by trying to lowering or increasing the airflow into the rheometer. These were done by covering the top of the

containment cylinder with wax to cut off air and by pointing a fan into the containment cylinder to increase air flow. When we tried experiments without Velcro, the peak shape narrowed but the time between peaks stayed consistent.

3.5 Effects of Changing Volume Fraction

The observed congruence of the moduli is progressively lost as ϕ_{eff} increases and eventually results in an ant aggregation that is predominantly elastic, as shown in Fig. 3.16 (a). For $\phi_{eff} = 4.4$, corresponding to a density of $\rho = 1.36\ g/cm^3$, the elastic modulus $G' > G''$ and G' is weakly dependent on frequency. The congruent power-law behavior observed at the lowest ant densities within the frequency range probed in our experiments is not maintained at higher densities and the ants are unable to relax as much, hence exhibiting a predominantly elastic behavior. This is reflected also in the power law exponent, Fig. 3.17 (a,b). The power law exponent is larger when calculated from Eq. 3.17, Fig. 3.17 (a), than from fitting G' and G'' to ω^n, Fig. 3.17 (b), though this effect is smaller for larger ϕ_{eff}. The exponent for dead ants is not dependent on ϕ_{eff}. For large ϕ_{eff} the exponent values for live and dead ants become similar.

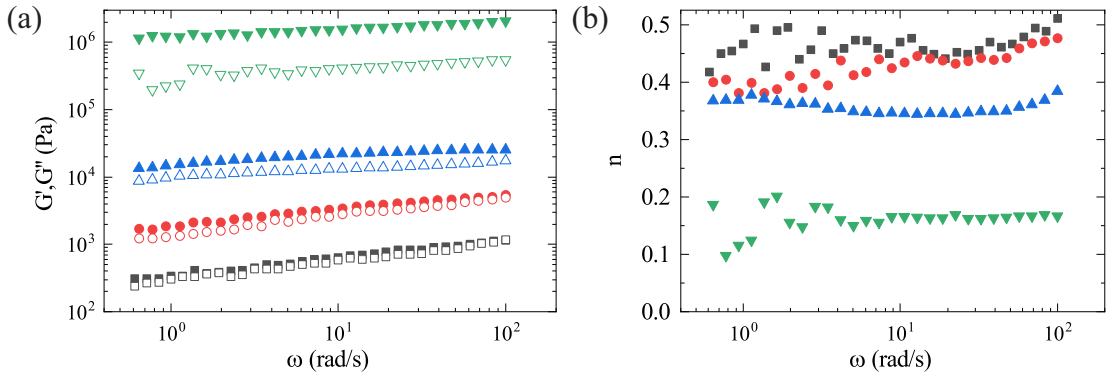

Figure 3.16: (a) Frequency sweep in the linear regime for live ants at $\phi_{eff} = 1.1$ (squares), $\phi_{eff} = 2.2$ (circles), $\phi_{eff} = 3.3$ (triangles), and $\phi_{eff} = 4.4$ (upside-down triangles). G' (closed) and G'' (open) are shown. As the effective volume fraction is increased the congruence observed for $\phi_{eff} = 1.1$ disappears and G' progressively becomes larger than G'' and becomes more frequency independent. (b) n calculated from Eq. 3.9 for the frequency sweeps in (a) with corresponding shapes and colors.

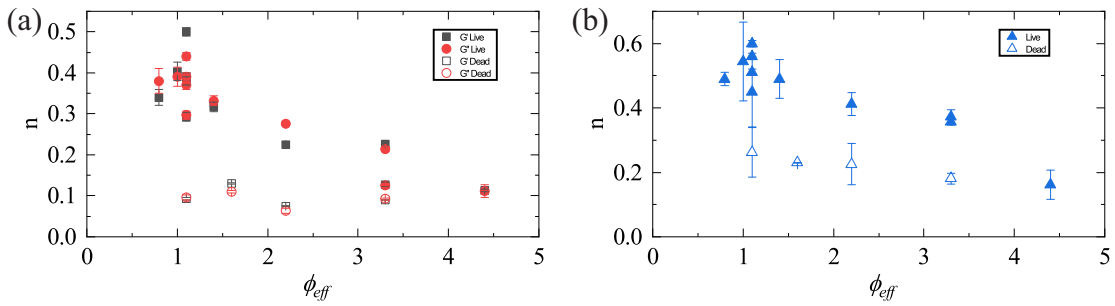

Figure 3.17: (a) Power law exponent found from Eq. 3.9 for live (solid) and dead (open) at a range of densities. (b) Power law exponent found from fitting frequency sweeps of live (solid) and dead (open) at a range of densities. Fits of G' are shown in black, G'' in in red.

The values of G' increase significantly with ϕ_{eff}, indicating that the ant aggregation stiffens with increasing density. To quantify this increase in G', we correlate the elastic modulus with ϕ_{eff} at a fixed frequency of $10\ rad/s$; similar results are obtained at any frequencies. We find that G' scales linearly with ϕ_{eff} up to $\phi_{eff} \approx 1.4$, as shown in Fig. 3.18. This linear behavior is also observed in thermal systems like colloidal hard sphere suspensions or Brownian emulsions in the supercooled liquid regime, below the volume fraction where a colloidal glass forms [215]. In these materials, the elasticity is of entropic in nature and arises from the progressive decrease in the available particle configurations as the particle volume fraction is increased, implying that $G' \sim kT/a^3$, with k the Boltzmann's constant, T the absolute temperature and a the inter-particle distance [2]. Using that $1/a^3 \sim \rho/m \sim \phi_{eff}$, we obtain that G' scales linearly with volume fraction. We then interpret the linearity of G' with ϕ_{eff} below $\phi_{eff} \approx 1.4$ for our ant aggregations as resulting from crowding effects and a progressive decrease in the ant configurations with increasing ϕ_{eff}.

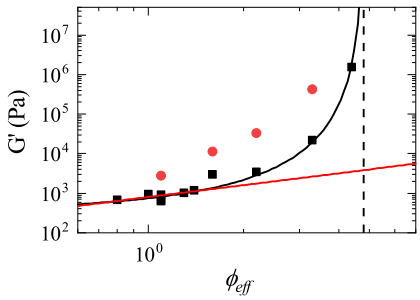

Figure 3.18: Storage modulus, G', as a function of effective volume fraction, ϕ_{eff}. The red line shows the initial linear scaling of G': $G' \sim \phi_{eff}$. After $\phi_{eff} = 1.4$, G' begins to increase faster than linearly. This is described by $G' \sim (\phi_c - \phi_{eff})^{-\alpha}$, shown be the black line, with $\phi_c = 4.8$ and $\alpha = 3.5$. The divergence at $\phi_c = 4.8$ is shown with a black dashed line.

For $\phi_{eff} > 1.4$, this linear behavior is lost and a new mechanism must now control the elasticity of the ant aggregation. To support this interpretation, we consider a cylindrical volume per ant with length equal to the ant length, l, and width w_1, and obtain w_1 from the condition that these cylinders fill space at $\phi_{eff} = 1.4$. Hence, from the condition:

$$\phi_{cyl} = 1 = (\frac{\rho}{m})[\pi(\frac{w_1}{2})^2 l], \tag{3.18}$$

where $\frac{\rho}{m} = \phi_{eff}(\frac{M_{ant}}{V_{ant}})$ is obtained from the fact that these cylinders fill space when $\phi_{eff} = 1.4$, we find $w_1 = 0.80\ mm$. The corresponding cylinder per ant is shown in Fig 3.19 (a) together with an image of a typical ant. Interestingly, the width of the resultant cylinder is close to but slightly smaller than the width of an ant with extended legs. This is then consistent with the idea that below $\phi_{eff} = 1.4$ the ants crowd, while for $\phi_{eff} > 1.4$, a new mechanism, presumably involving leg compression and more direct ant-ant interactions, becomes important. In this new regime, G' increases faster than linearly with ϕ_{eff}. The overall behavior of G' is well described by $G' \sim (\phi_c - \phi_{eff})^{-\alpha}$, with $\phi_c = 4.8$ and $\alpha = 3.5$ (see Fig. 3.18 (a)). Note that the value of ϕ_c sets the apparent divergence of G'. Physically, this critical effective volume fraction corresponds to the point where the ants cannot be further compressed. If we again calculate the width of a cylindrical volume associated to

an ant, assume that $1 = (\rho/m)[\pi(w_2/2)^2 l]$ and use that $\phi_{eff} = \phi_c = 4.8$ to obtain ρ/m, we find $w_2 = 0.43\ mm$ and a cylinder depicted in Fig. 3.19 (b) together with an image of a typical ant. Consistent with our interpretation, this width approximately corresponds to the width of an ant's body. As a result, if ants were compressed beyond this limit, we would be probing the elasticity of the ant exoskeleton, which has an elastic modulus that is much larger than the elastic modulus of the aggregation [179, 216]. The critical value of the volume fraction corresponds to a density of ants of $1.5\ g/cm^3$, which is around the same density as crystalline chitin which has a density of $\approx 1.4\ g/cm^3$ [179, 180]. Hence, the larger value of this elastic modulus sets the apparent divergence of the elastic modulus of the ant aggregation. Our results thus suggest that the elasticity of the ant aggregation can be understood as resulting from ant crowding first, followed by a jamming transition associated with the compression of the legs of the ants.

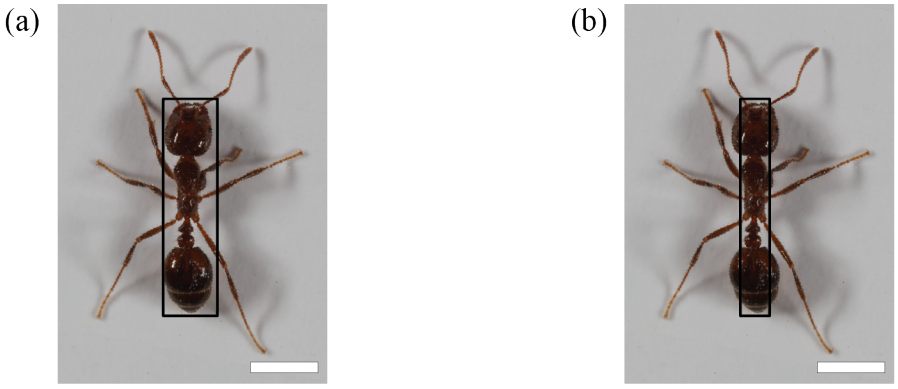

Figure 3.19: (a) A cylinder of length, $l = 3.2\ mm$, and width, $w_1 = 0.80\ mm$ overlaid on an ant. The cylinder sits just inside the reach of the ants legs. This corresponds to a ϕ_{eff} of 1.4, the transition from linear to non-linear scaling of G' with ϕ_{eff}. (b) A cylinder of length, $l = 3.2\ mm$, and width, $w_2 = 0.43\ mm$, overlaid on an ant. The cylinder fits closely around the body of the ant. This corresponds to the divergence of G' shown in (a), $\phi_{eff} = \phi_c = 4.8$. Scale bars are $1\ mm$.

In contrast, for dead ants only the weak frequency dependence of the moduli seen at high ρ for live ants is observed. We find that irrespective of the ant density, the elastic modulus $G' > G''$ and that it is weakly dependent on frequency, as shown in Fig. 3.20 (a). The exponents from the frequency sweeps also show the frequency independence as well

as the elasticity, Fig. 3.20 (b). The elastic modulus also increases with ant density, Fig. 3.20 (a) and Fig. 3.18, though not in the same way that live ants increase.

The behavior of live ants at high ϕ_{eff} is then similar of that of dead ants, where the importance of dissipation is expected to be lower. There are still movements at high volume fraction even if the density prevents most of them. We do detect a measurable contribution from G'' in the case of dead ants. We speculate this viscous modulus arises from rearrangements of the ants due their mechanically unstable packing from being loaded into the rheometer. Consistent with this physical picture, the normal force we measure along the span of the oscillatory experiment decreases, indicating that indeed the system is evolving to achieve a mechanically stable packing. Our results in the linear regime clearly indicate that the mechanics of live ant aggregations are characterized much more so by their activity than by the mechanics of dead ant aggregations; this is reminiscent of what is seen for active particles compared to Brownian particles [58, 217–219].

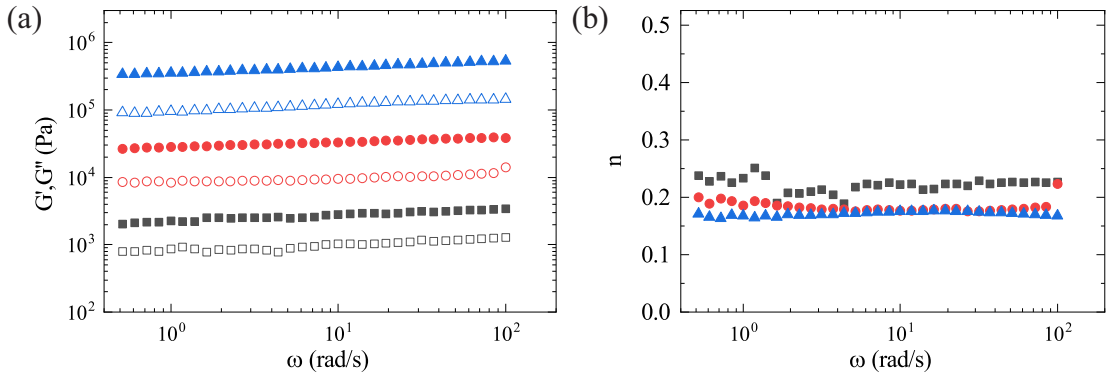

Figure 3.20: (a) Frequency sweeps of dead ants in the linear regime for ants at $\phi_{eff} = 1.1$ (squares), $\phi_{eff} = 2.2$ (circles), and $\phi_{eff} = 3.3$ (triangles). For all three densities G' is larger than G'' over the entire frequency range and exhibits little frequency dependence. This indicates the elastic nature of the dead ant aggregations. (b) n calculated from Eq. 3.9 for the frequency sweeps in (a) with corresponding shapes and colors.

3.6 Conclusions

The mechanical properties of fire ant aggregations are not constant in time but rather change with changing levels of activity. The level of activity is related to the number of active ants

in the aggregation and is correlated with the normal force. We model this behavior with coupled differential equations with time dependent constants. The time dependence reflects that as more ants become active the rate at which other ants become active increases and vice versa for the rate of deactivation. We find that the rate of turn on and turn off are the same. The shape of the peaks in the normal force is the same both within and between experiments and when compared to peaks in activity measured from 2D experiments.

Aggregations are equally viscous and elastic over the frequency range probed when active and at $\phi_{eff} = 1.1$. They show power law behavior that is consistent with the Kramers-Kronig relations. They are predominantly elastic when at low activity levels or dead. As ϕ_{eff} is increased active aggregations become more and more elastic, both in the magnitude of the storage modulus and in the relative weight of G' and G''. We can monitor this change from equally viscous and elastic to predominantly elastic using the power law exponents from fitting frequency sweeps directly or from calculating the exponents based on the Kramers-Kronig relations. This means that to change the mechanical properties of the aggregation we can either wait for the activity level to change or change the density of the ants.

CHAPTER 4

CREEP

To further inquire about the behavior of the ant aggregation, we perform creep experiments. This type of experiment has not been done before with dense active aggregations except for some work on cell aggregations. Cellular aggregations experiencing constant stress show short time elastic behavior and long time flow [218, 220, 221]. In cell experiments an applied stress of $0.1 - 5\ kPa$ was applied over 3 hours. The shear rate increased with applied stress until it saturated after about an hour . This highlights that aggregations of cells are predominantly elastic and are slow to move under external stresses.

Since in ant aggregations the mechanical properties are not constant in time and are at time "equally" viscous and elastic, we now look at how these changing material properties affect the flow response of the aggregation. We apply a step stress σ_0 at $t = 0$, and measure the time evolution of the strain, $\gamma(t)$. The ant aggregation is not forced to flow but rather responds spontaneously to the applied stress.

4.1 High Stress

There is an upper limit to the stress that can be applied to an ant aggregation of about $250\ Pa$. At stresses above this limit the ants are ripped apart, which we saw when removing the ants from the rheometer after an experiment. Since we are interested in the ants because of their activity, killing them during an experiment is not useful except that it tells us the force necessary to break off a limb. Ants can hold onto each other with a force of $2\ mN$ in tension through leg-leg interactions [38]. This means that the limbs are not pulled off since the stress that an ant limb can support is larger than $250\ Pa$ since the ants limbs have a cross section on the order of $0.01\ mm^2$ across. However the joints are much easier to breach in shear than in tension and $250\ Pa$ is enough to shear off limbs.

For stresses near but not past this limit the aggregation flows like a simple liquid, Fig. 4.1. Here the strain increases linearly with time. The slope of the strain vs time gives the shear rate, $\dot{\gamma}$, which is constant. We can combine this with the applied stress to calculate the viscosity of the aggregation in these conditions: $\eta = \sigma_0/\dot{\gamma}$.

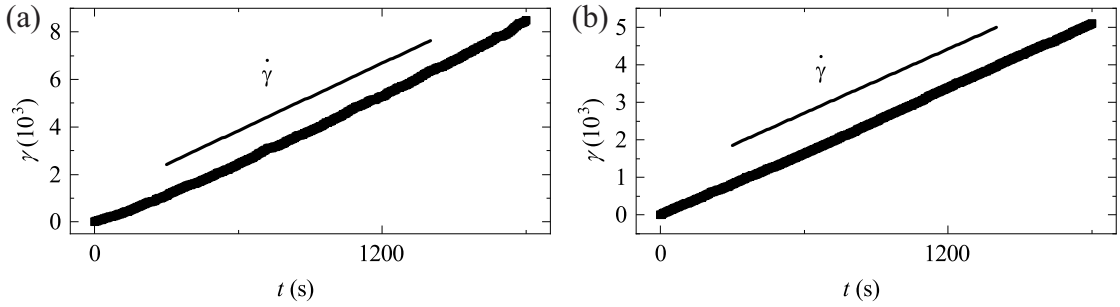

Figure 4.1: Creep experiments of live ants at $\phi_{eff} = 1.1$ at 200 Pa (a) and 100 Pa (b). The strain is linear throughout both 30 min experiments, showing that there is a global shear rate for both experiments.

4.2 Lower Stresses

For stresses below 100 Pa the aggregation no longer flows like a simple liquid. There are periods of flow but also periods of energy storage where the applied stress does not force the aggregation to flow. This implies that the ants are able to behave elastically over a certain time frame, preventing flow from occurring. From the linear regions in the strain-time curves, we can determine a shear rate and hence a viscosity. The regions where the aggregation is able to resist the applied stress increases in duration for lower applied stresses, Fig. 4.2. This is markedly different from cellular aggregations which do not show intermittent behavior.

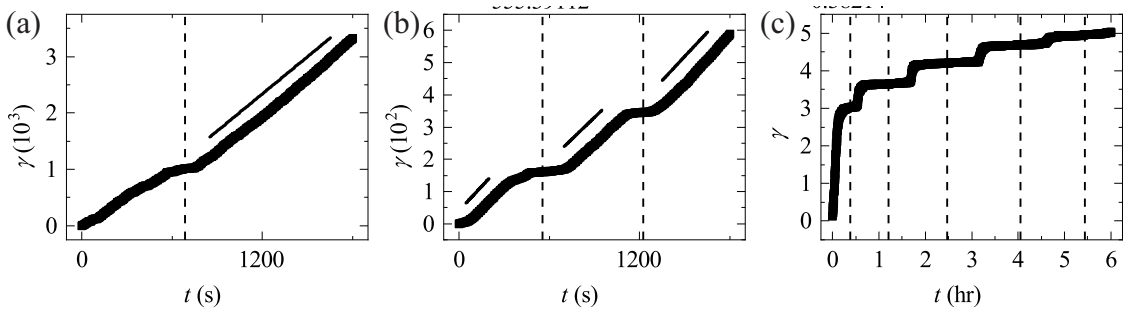

Figure 4.2: Creep experiments of live ants at $0.34g/cm^3$ at $70\ Pa$ (a), $40\ Pa$ (b), and $5\ Pa$ (c). In all three there are periods of time when the ants resist the applied stress and times when they flow with it. When the aggregation is flowing it is possible however to describe a local shear rate, as illustrated by the solid lines.

Interestingly, this change in aggregation behavior is also noticeable in the normal force, as shown in Fig. 4.3, which show the normal forces corresponding to the strain curves in Fig. 4.2. We see that when the normal force is lower the aggregation is more elastic and able to support the applied stress. In contrast, The normal force is high when the aggregation is flowing. As the applied stress decreases, the number of resisting periods increases. This indicates the role of activity is larger at lower applied stresses. This periodicity of the response was seen in Chapter 3 where changes in the viscoelastic properties were correlated with changes in the normal force, Fig. 3.8. Lower normal force corresponded to a more elastic aggregation, consistent with what is also seen in creep experiments where periods of flow are characterized by higher normal force and periods of resistance by low normal force.

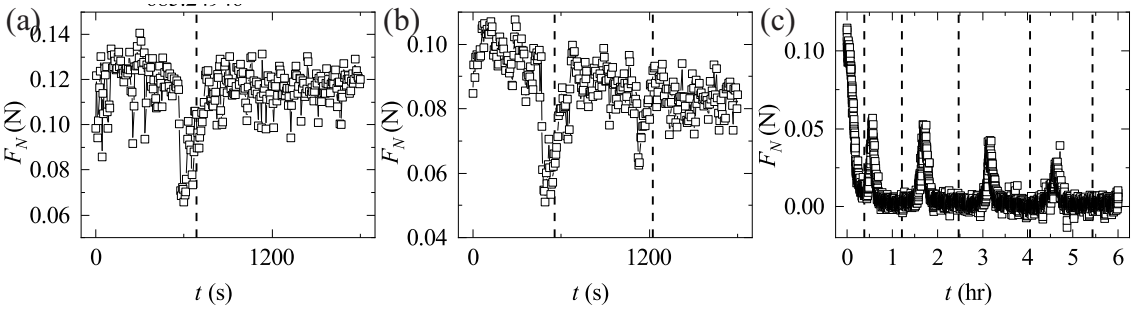

Figure 4.3: (a) Normal force for the creep experiment at $70\ Pa$ in Fig. 4.2 (a). (b) Normal force for the creep experiment at $40\ Pa$ in Fig. 4.2 (b). (c) Normal force for the creep experiment at $5\ Pa$ in Fig. 4.2 (c).

4.2.1 Dead Ants

We attribute the sudden changes in the normal force and the corresponding changes in the flow behavior to the ants activity. We have confirmed this by performing creep experiments with dead ant aggregations, where there is no activity. For dead ants, the strain is a strictly monotonic function of time, as shown in Fig. 4.4, confirming that the intermittent behavior with plateau regions observed with live ants is indeed due to ant activity. This is also consistent with a granular medium under constant stress which do not show plateau regions or large changes in the normal force and instead show monotonic creep behavior [25].

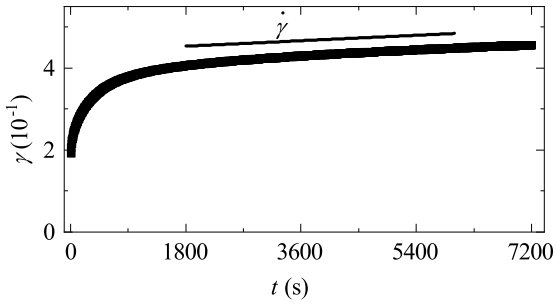

Figure 4.4: Creep experiment with dead ants at $\phi_{eff} = 1.1$ and $40\ Pa$. The timescale of this test is $2\ hrs$, 4 times longer than the creep experiments with live ant aggregations. The aggregation is elastic at shorter times, $t < 600\ s$ and flows at longer times, $t > 600\ s$.

4.2.2 Alternative Creep Tests

Another way to provide a constant stress to an aggregation is to place an object on top of the aggregation and monitor the objects progress through the aggregation. We did this by placing a lead sphere onto an aggregation confined in a test tube with a diameter of $2.7\ cm$.

The lead sphere has a diameter of $d_{sphere} = 1.1\ cm$ and a density $\rho_{sphere} \approx 11\ g/cm^3$. The aggregation has a density of $\rho \approx 0.3\ g/cm^3$. The test tube is vertical so that gravity pulls the sphere down with a constant fore, mg, with g the acceleration due to gravity. This downward force by gravity is balanced by "drag" such that the sphere falls with a constant speed through the aggregation. We measure this terminal velocity by measuring the distance the sphere falls in a set time period, Fig. 4.5. The ants flow around

the sphere allowing it to fall at a speed of $v \approx 2 \times 10^{-3}\ cm/s$. From these parameters we can calculate a shear rate by dividing the speed by the diameter of the sphere: $(2 \times 10^{-3}\ cm/s)/(1.1\ cm) = 1.8 \times 10^{-3}\ s^{-1}$. We then calculate the viscosity from the "Stokes drag" on the sphere [27, 222],

$$\eta = \frac{2}{9}\frac{(\rho_{sphere} - \rho)}{v} g \Big(\frac{d_{sphere}}{2}\Big)^2. \tag{4.1}$$

Though this is technically only true for spheres far away from any walls, when including wall proximity into the viscosity calculation, the result does not significantly change. The Ladenburg equation gives the first order wall effect correction with the drag being larger by a factor of $1 + 2.1044(d_{sphere}/d_{cylinder})$ [27]. Since $d_{sphere}/d_{cylinder} = 1.1/2.7 = 0.407$, the total correction is 1.86 which does not change the order of magnitude of our estimate.

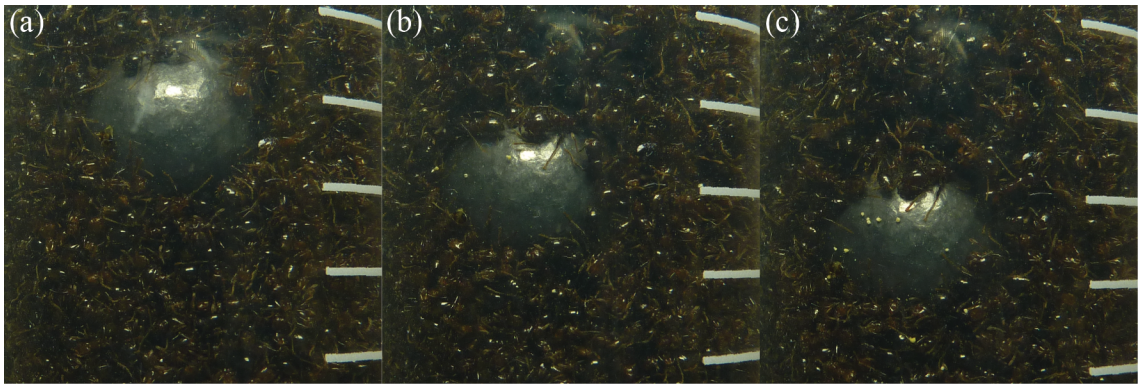

Figure 4.5: (a-c) A lead sphere of diameter, $1.1\ cm$ is placed on top of an ant aggregation, $\rho \approx 0.3\ g/cm^3$, inside a test tube. The test tube is vertical so that the gravitational acceleration on the sphere is $g \approx 10^3\ cm/s^2$. The time lapse between images is $90\ s$.

4.3 Viscosity

As we already mentioned, we can calculate a viscosity from each creep experiment by combining the measured shear rate and the applied stress, $\eta = \sigma_0/\dot{\gamma}$. For high stress experiments the shear rate comes from the entire experiment but for low stress experiments it comes from those regions where the aggregation is flowing. The shear rate versus applied stress is shown in Fig. 4.6 (a) where we see that the shear rate is larger for larger applied

stress. The viscosity however, decreases with increasing applied stress, Fig. 4.6 (b).

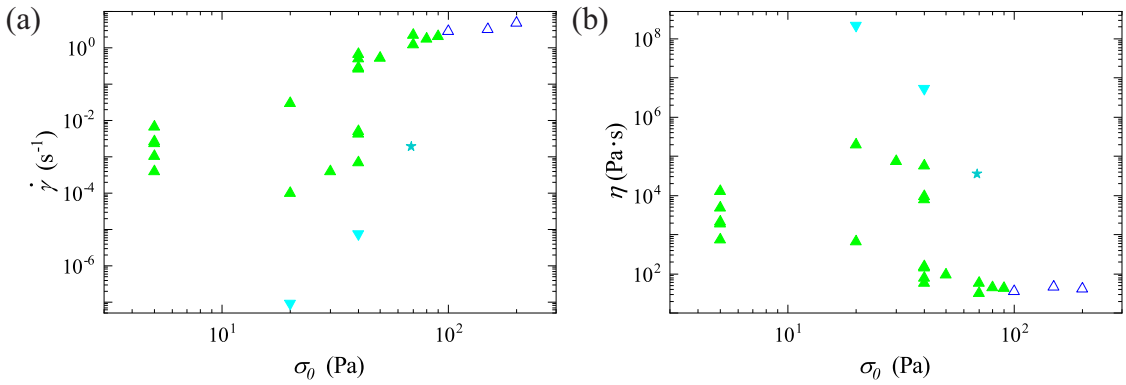

Figure 4.6: (a) Shear rate as a function of stress and (b) viscosity versus stress. The upwards triangles correspond to measurements taken from creep experiments with live ants. The open symbols are measurements above $100\ Pa$ as seen in Fig. 4.1. The downwards triangles correspond to viscosities taken from creep experiments with dead ants. The star is from the falling sphere in Fig. 4.5. $\phi_{eff} = 1.1$ in all these experiments.

We can then plot all of these points on a plot of viscosity versus shear rate to look at the nonlinear flow properties of the aggregation. This is shown in Fig. 4.7 where the first thing we notice is that the viscosity decreases with increasing shear rate. The next thing to notice is that the shear rate increases and the viscosity decreases as we move from dead ants (downward triangles) to live ants at low applied stress (closed upwards triangles) to live ants at high applied stress (open upwards triangles). The falling sphere falls in the middle of the live ants and in line with the other data points. We also note that the viscosity scales as $\dot{\gamma}^{-1}$, represented by the solid line in Fig. 4.7. The ant aggregation shear thin. At low shear rate the viscosity of a live aggregation is similar to smooth peanut butter! [223], at the highest shear rate live aggregations have a viscosity just above that of honey [224]. XXX

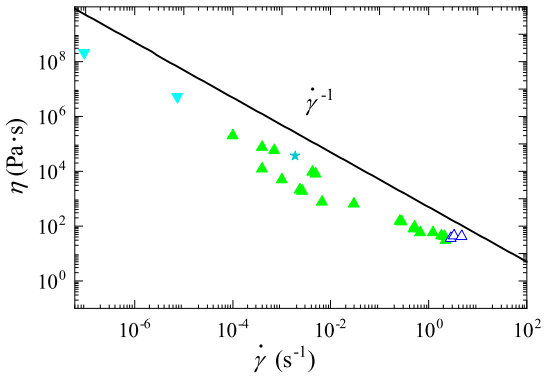

Figure 4.7: Viscosity, η, as a function of shear rate. The upwards triangles correspond to viscosities taken from creep experiments with live ants. The open symbols are measurements above $100\ Pa$ as seen in Fig. 4.1. The downwards triangles correspond to viscosities taken from creep experiments with dead ants. The star is the viscosity from the falling sphere in Fig. 4.5. $\phi_{eff} = 1.1$ in all these experiments.

4.4 Zero Stress

Under a high applied stress, ant aggregations flow at an approximately constant shear rate. When lower stresses are applied, the aggregations are able to resist the applied stress for shorts periods of the time and remain stationary, reflecting the inherent activity of the system. These periods also increase in duration for lower applied stresses. We then decided to monitor the aggregation's behavior in the absence of applied stress. To measure $\gamma(t)$ in these conditions, we apply a $0\ Pa$ stress, 0 within the limits of the rheometer. For an inactive system, the result would be zero strain.

Remarkably, for an applied stress of $0\ Pa$, we observe that the aggregation still moves and is able to produce a measurable strain, as shown in Fig. 4.8 (a). The ants spontaneously strain the tool of the rheometer. Note that the strain we measure is cumulative and indicates the current position relative to the position of the top plate at the start of the experiment. Here, live ants are able to move the top tool in either direction. For instance, at $4\ hrs$ they cause a clockwise rotation of the upper tool, while at $5\ hrs$ they produce a counterclockwise rotation of the upper tool. By converting the strain into a length scale, $R\phi = h\gamma$, we find that the maximum strain we measure is about two ant lengths. This is in stark contrast with

the behavior of any equilibrium material, where the application of a 0 Pa stress would cause no measurable strain.

Interestingly, we observe that the active periods correlate with the normal force, as shown in Fig. 4.8 (c). When the aggregation is straining, the normal force measured at the top plate is higher. When the top plate is not being strained, corresponding to the plateau regions in Fig. 4.8 (a), we find that the measured normal force is low. This is consistent with what we have seen in Chapter 3 and indeed the peak shape of normal force peaks is the same whether or not oscillatory measurements are being carried out.

We can also compare this to the behavior of dead ants subject to the same test, shown in Fig. 4.2 (b). The rearrangement due to unstable configurations of the dead ants moves the tool an order of magnitude less distance in one hour and the tool never changes direction. This small motion of the top tool in the dead ant case can then be attributed to the unstable granular dead ants settling over the course of the experiment. This is supported by the normal force falling for the entirety of the dead ant experiment, Fig. 4.8 (d).

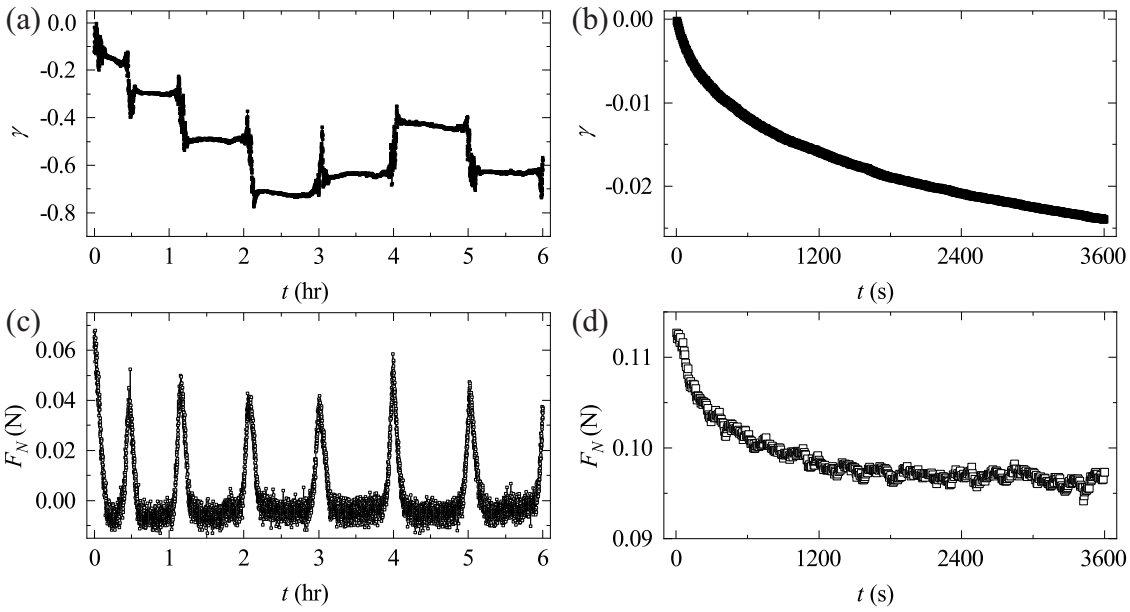

Figure 4.8: (a) Strain as a function of time for a creep experiment at an applied stress of $0\ Pa$ with a live ant aggregations. (b) The same experiment as (a) but with dead ants. (c) Normal force measurement corresponding to the creep test in (a). The normal force peaks at times where the strain changes for live ants. (d) Normal force measurement corresponding to the creep test in (b). The dead aggregation moves as the dead ants settle.

4.5 Effective Volume Fraction

Figure 4.9 (a) shows the first hour of creep experiments done with an applied stress of $0\ Pa$ with increasing densities. We see that as the effective volume fraction is increased, the amount the top tool rotates decreases significantly. At $\phi_{eff} = 3.3$, the ants move the top tool a similar amount to what was observed with dead ant experiments at $\phi_{eff} = 1.1$ indicating that the activity is being suppressed by the increase in density. This is consistent with what we saw in oscillatory measurements where for large ϕ_{eff} the behavior of live ants was similar to that of dead ants, Fig. 3.17.

The normal force increases with increasing ϕ_{eff} as is expected as the system is denser and more elastic. At $\phi_{eff} = 3.3$ both the strain and the normal force versus time resemble that of the dead ants in Fig. 4.8 (b,d). This again indicates that the importance of the activity decreases with increasing ϕ_{eff}.

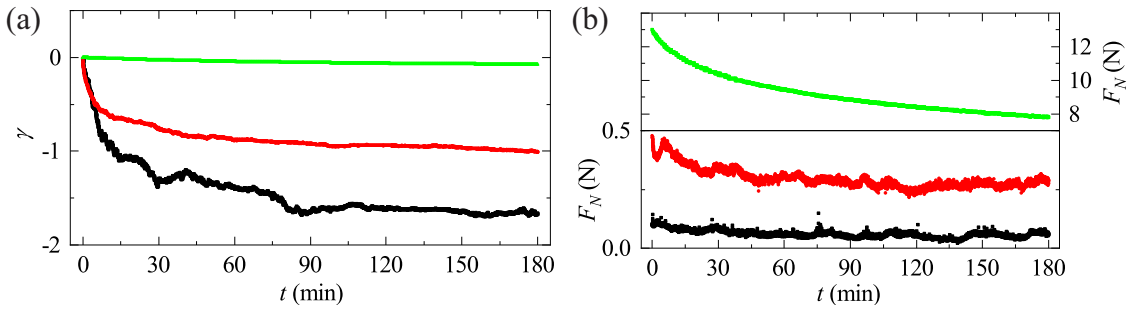

Figure 4.9: (a) Strain vs time for different volume fractions: 1.1 (black), 2.2 (red), and 3.3 (green). The maximum strain reached after $1\ hr$ decreases with increasing effective volume fraction. (b) Normal force vs time for the creep experiments in (a). The highest density is on a different axis so that all three are visible.

4.6 Conclusions

At high stresses, ant aggregations flow like simple liquids. At low stresses, they are able to resist the applied stress for periods of time. As such, there are periods where the ants flow and periods where they store energy. This behavior is correlated with the behavior of the normal force. When the aggregation is storing energy, the normal force is low and when

they flow the normal force is high. In contrast dead ants behave as granular matter. The intermittent behavior observed with live ants has not been seen in previous studies of active matter under constant stress.

With an applied stress of $0\ Pa$, within the limits of the rheometer, the activity of the ant aggregations cause the straining of the rheometer tool. We have seen them rotate the edge of the top tool a distance of 2 ant lengths and they can move the tool in either direction. The self straining behavior is again correlated with the normal force: when the aggregation is moving the top plate, the normal force is high, when they are static, the normal force is low. The peak shape is similar to what was seen and modeled in Chapter 3. Also like in chapter 3, when the density is increased the effects of the activity are suppressed.

CHAPTER 5
CONTROLLED SHEAR RATE

In this chapter we will discuss controlled shear rate experiments, where we apply a shear rate and measure the stress that is required to maintain the imposed flow. This is done to measure the nonlinear flow properties of the aggregation. When trying to measure the viscosity of a material controlled shear rate experiments are complementary to creep experiments which were discussed in the previous chapter. There we applied a constant stress, and measured the strain as a function of time to find the shear rate where possible and calculate the viscosity. We found that there were also times where the aggregation resisted the applied stress and we could not, as a result, determine a shear rate. Since we are now fixing the shear rate, the aggregation is forced to flow, bringing the aggregation well into the nonlinear regime. This allows us to measure the viscosity over a wide range of imposed shear rates.

Experiments are done for shear rates ranging from 10^{-4} to 10^{2} either starting at the lowest shear rate and getting progressively higher or starting at the higher shear rate and working downwards. All of the experiments presented in this chapter are done at a volume fraction of: $\phi_{eff} = 1.1$. We have used two different gap heights: $(2.00 \pm 0.05)\ grams$ of ants, $\approx 2800\ ants$ at $h_{Velcro} = 3\ mm$ and $(3.00 \pm 0.05)\ grams$ of ants, $\approx 4200\ ants$, at $h_{Velcro} = 4.5\ mm$. We find that the mechanical response is not significantly affected by the different gap height.

The viscosity of suspensions of cells has been measured experimentally in both conventional rheometers and microfluidic devices [131, 132, 225]. They find either a reduction or an increase in the viscosity depending on type of bacteria in the suspension. The lowering of the viscosity is only seen for pusher type cells and is caused by the hydrodynamic interactions of the active cells, typically *E. Coli* is used as a model pusher [132, 225]. This

effect has only been tested up to $\phi = 0.01$. Pullers increase the viscosity of the solution up at all measured volume fraction, $\phi = [0, 0.2]$. All of these studies have been at low volume fraction, $\phi < 0.2$ where the suspending fluids viscosity still plays an important role. In ant aggregations there is no suspending fluid and so any viscous effect must solely be based on the dissipation in the aggregation.

5.1 Stress, Viscosity, and Normal Force

Starting from high shear rate, we find that as the shear rate, $\dot{\gamma}$, is decreased, the stress, σ, also decreases, Fig. 5.1 (a). However, within a relatively large range of $\dot{\gamma}$, from $10^1\ s^{-1}$ to $10^{-3}\ s^{-1}$, the stress remains approximately constant and is always less than $100\ Pa$. As a result, the sample viscosity, $\eta = \sigma/\dot{\gamma}$, dramatically decreases with increasing $\dot{\gamma}$ as $\dot{\gamma}^{-1}$, Fig. 5.1 (b). Hence, the ant aggregation dramatically shear thins. Most suspensions that shear thin do so at $\dot{\gamma}^{-\alpha}$, $\alpha < 1$, with $\alpha = [0.3 - 0.7]$ being common [184, 194]. We then find that $\eta = \sigma_c \gamma^{-1}$ with $\sigma_c = 100\ Pa$ over an extended range of $\dot{\gamma}$. The main deviation from this trend is at high and low shear rate where the stress goes above and below $100\ Pa$. In the high shear rate region the normal force is also elevated, Fig. 5.1 (c).

The value of σ_c is the same as the cuttoff stress in Chapter 4 where creep experiments change from having intermittent flow to constant flow over the entire experiment. It is the lowest stress that has constant flow. From this we infer that when the aggregation is forced to flow, $100\ Pa$ seems to be the preferred stress.

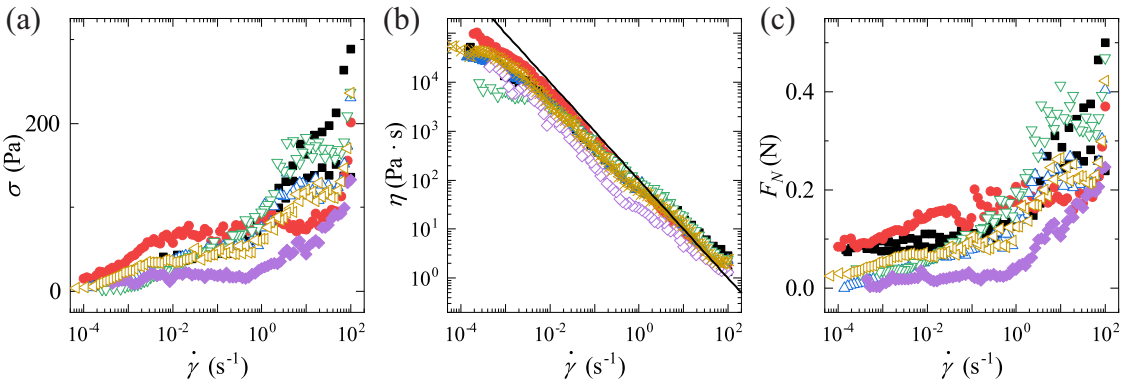

Figure 5.1: Shear stress (a), viscosity (b), and normal force (c) versus shear rate for controlled shear rate experiments with live ants. Each experiment begins at $\dot{\gamma} = 10^2$ and decreases until $\dot{\gamma} = 10^{-4}$. In (b), the line is $\eta = \sigma_c \dot{\gamma}^{-1}$. The closed symbols are for experiments with $(2.00 \pm 0.05)\ grams$ of ants and the open symbols are for experiments with $(3.00 \pm 0.05)\ grams$ of ants.

Similar results are obtained when the experiment is performed starting at the lowest shear rate. There is an additional range of increased stress around $\dot{\gamma} = 10^{-2}$ in addition to the an increase in the stress at high shear rate, Fig. 5.2 (a). This difference probably comes from the ants being more active and therefore more able to resist the applied flow since the shear rate is small at the beginning of the experiment. In the previous experiment by the time the ants were subjected to the lower shear rates their activity level was already lowered and as such they were unresisting to the applied flow. The increased stress at lower shear rate corresponds to an approximately constant viscosity at lower shear rate, as seen at low $\dot{\gamma}$ in Fig. 5.2 (b). That the stress goes to zero with decreasing shear rate implies that the aggregation does not have a yield stress which is consistent with the viscoelastic behavior seen in Chapter 3.

For higher shear rates the viscosity follows a similar form to the previous experiment, Fig. 5.2 (b) and the stress also again stays predominantly under $100\ Pa$. The normal force is high for large shear rate and decreases with decreasing shear rate except for around $\dot{\gamma} = 10^{-2}$ where there is a peak in the normal force similar to the peak in the stress.

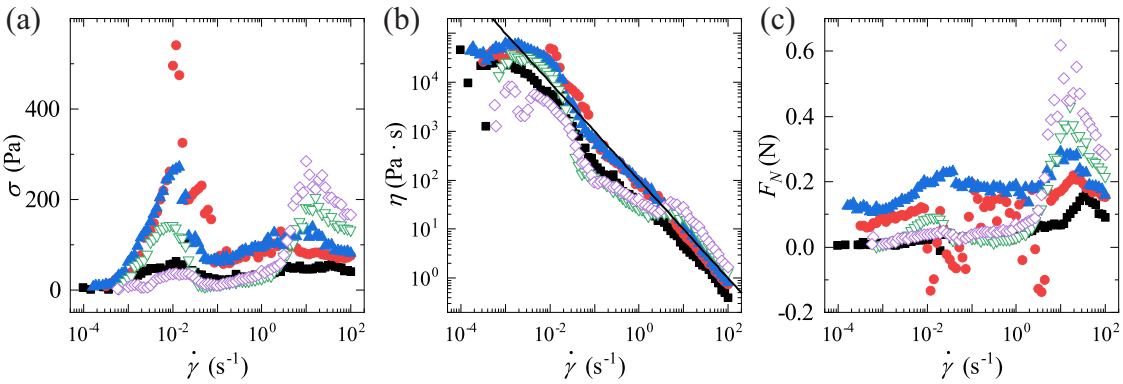

Figure 5.2: Shear stress (a), viscosity (b), and normal force (c) versus shear rate for controlled shear rate experiments with live ants. Each experiment begins at $\dot{\gamma} = 10^{-4}$ and increases till $\dot{\gamma} = 10^{2}$. In (b), the line is $\eta = \sigma_c \dot{\gamma}^{-1}$. The closed symbols are for experiments with $(2.00 \pm 0.05)\ grams$ of ants and the open symbols are for experiments with $(3.00 \pm 0.05)\ grams$ of ants.

We repeat this experiment with dead ants to tease apart the effect of activity from passive dissipative interactions (e.g. friction). For experiments that start at high shear rate the results are very similar for live and dead ants. The stress starts high and lowers continuously over the course of the experiment as shown in Fig. 5.3 (a) for all curves except for the red circles where the experiment was started at the lowest shear rate. For experiments starting at low $\dot{\gamma}$, the stress increases at low shear rate but eventually reaches a similar maximum to the experiments that start at high $\dot{\gamma}$. Both experiment types have peak stresses around $100\ Pa$. From the applied shear rate and the measured stress we calculate the viscosity, Fig. 5.3 (b). Dead ants shear thin, consistent with the stress only going up an order of magnitude over six orders of magnitude in shear rate. The viscosity again scales as $\eta = \sigma_c \dot{\gamma}$ with $\sigma_c = 100\ Pa$, the same as live ants. The normal force is high for large shear rate and decreases with decreasing shear rate, Fig. 5.3 (c).

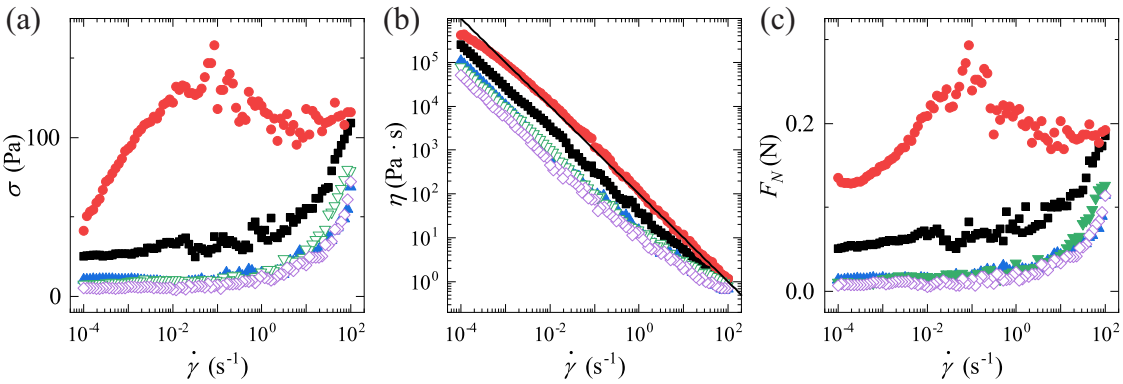

Figure 5.3: Shear stress (a), viscosity (b), and normal force (c) versus shear rate for controlled shear rate experiments with dead ants. The red circle experiment begins at $\dot{\gamma} = 10^{-4}$ and increases till $\dot{\gamma} = 10^{2}$, The rest begin at $\dot{\gamma} = 10^{2}$ and decreases till $\dot{\gamma} = 10^{-4}$. In (b), the line is $\eta = 100\dot{\gamma}^{-1}$. The closed symbols are for experiments with $(2.00 \pm 0.05)\ grams$ of ants and the open symbols are for experiments with $(3.00 \pm 0.05)\ grams$ of ants.

We can further check for the effects of activity by performing an experiment starting at high $\dot{\gamma}$ with live ants, removing them from the rheometer and killing them by freezing, and then repeating the experiment. In this way we remove all of the variables except for activity, since we are using the exact same ants for both experiments. Its the same number of ants with the same size distribution and subject to the same test.

The stress for both aggregations is within error when compared to Figs. 5.1, and 5.3 and the trend is the same, Fig. 5.4 (a). The viscosity is also comparable and the trend is the same, Fig. 5.4 (b). One difference is that at the highest strain the live ants have a region where the viscosity is mostly flat that is not present for dead ants. The normal force is higher for live ants than for dead but the trend of decreasing normal force with decreasing shear rate is the same. Again this lack of a significant difference highlights the fact that the behavior of the aggregation in controlled shear rate experiments is not based on the activity of the aggregation.

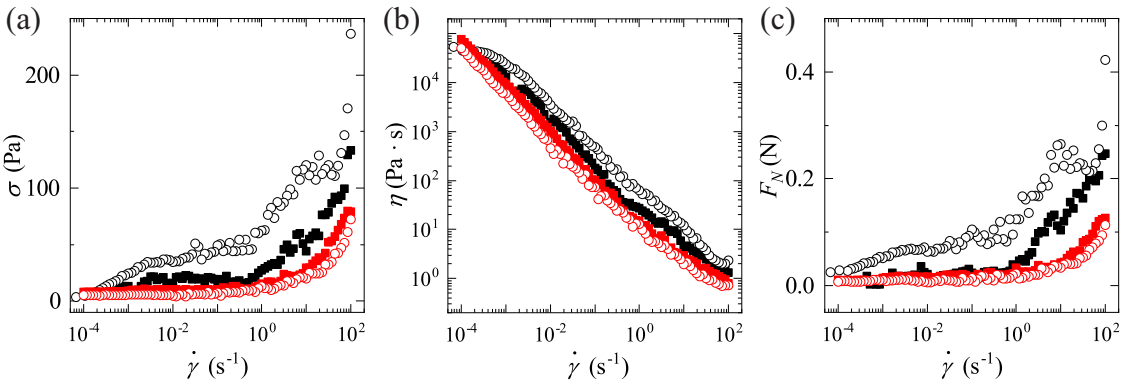

Figure 5.4: Shear stress (a), viscosity (b), and normal force (c) versus shear rate for controlled shear rate experiments with live and dead ants where the same colony was used for the live and dead experiments. The closed symbols are for a set of experiments with $(2.00 \pm 0.05)\ grams$ of ants and the open symbols are for a set with $(3.00 \pm 0.05)\ grams$ of ant. Both begin at $\dot{\gamma} = 10^2$ and decreases till $\dot{\gamma} = 10^{-4}$. The black symbols are for live ants and the red symbols are for dead ants.

Since the response to the applied shear rate is mostly the same for live and dead ants we can conclude that activity is not playing a major role in the behavior of the aggregation when forced to flow. Only at the highest $\dot{\gamma}$, for experiments where we decrease $\dot{\gamma}$, and the lowest $\dot{\gamma}$, for experiments where we increase $\dot{\gamma}$, do we observe small differences between the two situations. In these cases, η does not decrease with $\dot{\gamma}$, but rather remains approximately constant.

For both dead and live experiments the stress seems to be proportional to the normal force as both experimental curves have similar shapes; see for example, Fig. 5.1 (a) and (c). The shape of the stress versus shear rate is similar to the normal force versus shear rate for both increasing and decreasing experiments. We can compare these two quantities more directly by converting the normal force into a normal stress by dividing by the area of the top plate: $\sigma_N = F_N/(\pi R^2)$. We then divide the shear stress by the normal stress and find that the ratio is close to one, indicating the quantities are comparable, as shown in Fig. 5.5. Note however that for live ants the spread of possible values around 1 is larger than for dead ants, particularly at lower shear rates. This can be understood in terms of the relation between activity and F_N. The faster the aggregation is forced to flow, the more

homogeneous it becomes and the larger the outward normal force. In this case the imposed flow plays the role of the intrinsic aggregation activity. In granular systems increasing the applied shear stress decreases the volume fraction or if done at fixed volume, increases the normal force similar to what we see with the ant aggregation [25, 226].

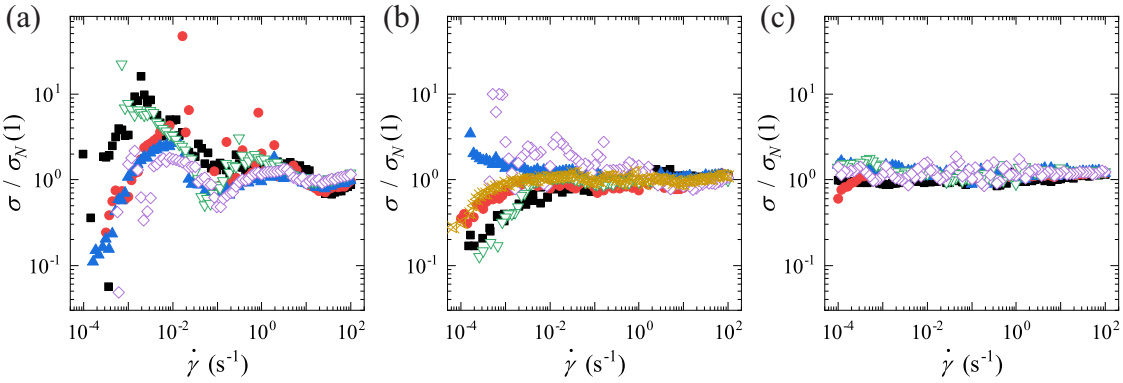

Figure 5.5: Shear stress divided by the normal stress for live ants with increasing shear rate (a), live ants with decreasing shear rate (b), and dead ants (c). The closed symbols are for experiments with $(2.00 \pm 0.05)\ grams$ of ants and the open symbols are for experiments with $(3.00 \pm 0.05)\ grams$ of ants.

5.2 Creep Comparisons

We can compare the values of viscosity that we get from controlled shear rate experiments to those found from individual creep experiments. We see good agreement between these two, with both following the trend line of $\eta = \sigma_c \dot{\gamma}^{-1}$ with $\sigma_c = 100\ Pa$, Fig. 5.6. Note that the viscosity obtained from the falling sphere experiment, shown in Fig. 5.6 with a star, also agrees with the viscosity obtained in the controlled shear rate experiments and from the creep experiments. This reflects that the viscosity of the ant aggregation changes to maintain a constant stress value that is close to the stress below which the aggregation is able to resist.

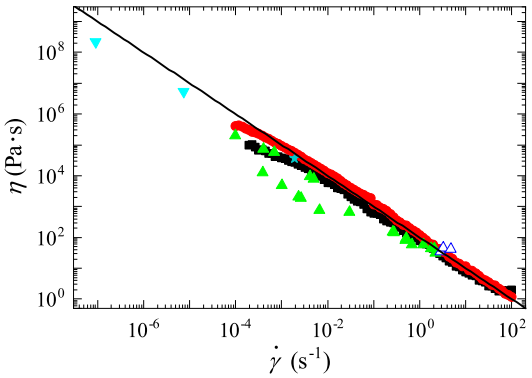

Figure 5.6: Viscosity from creep experiments and controlled shear rate experiments for both live (black squares) and dead (red circles) aggregations. These viscosities from creep experiments were measured from linear regions of the strain. The cyan downward triangles are from dead ant experiments, the green upward triangles are for creep experiment below $100\ Pa$ of stress, and the open blue triangles are from experiments above $100\ Pa$ of applied stress. The blue star is the viscosity measured from the ball falling through the tube of ants. The comparison line is $\eta = 100\dot{\gamma}^{-1}$.

5.3 Comparison to Individual Ant Behavior

To investigate what is happening at the individual ant level, we consider the energy dissipation rate per unit volume, $\Phi = \sigma\dot{\gamma}$ [184]. Since $\sigma = \eta\dot{\gamma}$ for viscous stresses, $\Phi = \eta\dot{\gamma}^2$. We substitute the relation that we found for the viscosity, $\eta = \sigma_c\dot{\gamma}^{-1}$, resulting in $\Phi \approx \sigma_c\dot{\gamma}$, where from experiment, $\sigma_c = 100\ Pa$. Note that σ_c is thus an energy loss per unit volume. In addition, results with dead and live ants are similar, indicating that the main contribution to the viscosity is not from the activity of the aggregation. When forced to flow, live ants seem to "play dead", ceasing all active motion.

One possible source for the energy loss common to live and dead aggregations is the friction in the leg joints of the ants; this friction must be overcome for an ant leg to give way and allow strain-rate-induced rearrangements within the aggregation. Indeed, highly frictional joints is a hallmark of insects such as stick insects [227] and is the reason that ants do not expend more energy walking uphill vs downhill [228]. Since most of their energy is put into overcoming the friction in their own joints and they have sticky pads giving them good attachment to the surface they are walking on, ants motion is not affected by walking

up or down inclines. To measure the dissipation in a limb, we take a dead ant and remove all but one of its legs. We then bring the ant with its leg oriented perpendicularly to the plate of an analytical balance and measure the force required for the leg to be displaced vertically a distance $L \approx 1\ mm$, which corresponds to the full range of motion of the leg, Fig. 5.7 (a). We video record the process to watch both the leg move and the reading on the balance, Fig. 5.7 (b). We average $N = 6$ measurements and obtain a force $F = (2 \pm 1)10^{-5}\ N$, which is approximately 2 ant body weights.

We can estimate the work done over the course of the motion as FL. Considering that an ant has six legs, the energy loss at the joints per unit volume due to joint movement is $E = 6FL/l^3 \approx 30 \pm 15\ Pa$. This measurement of the energy loss per unit volume is close to the value σ_c found in our rheological tests indicating that the value of σ_c could be associated with the energy required to overcome the friction in the leg joints of the ants. This picture is consistent with a single value of σ_c corresponding to both live and dead ants and suggests that live ants, when forced to flow, indeed "play dead" by allowing their limbs to deform as they would if the ants were dead and lacked inherent activity. The linear dependence of the energy dissipation per unit volume per unit time with $\dot{\gamma}$ then reflects that the number of joints that deform per unit time also increases linearly with $\dot{\gamma}$ since σ_c reflects the number of limbs deformed per volume and $\Phi \approx \sigma_c \dot{\gamma}$.

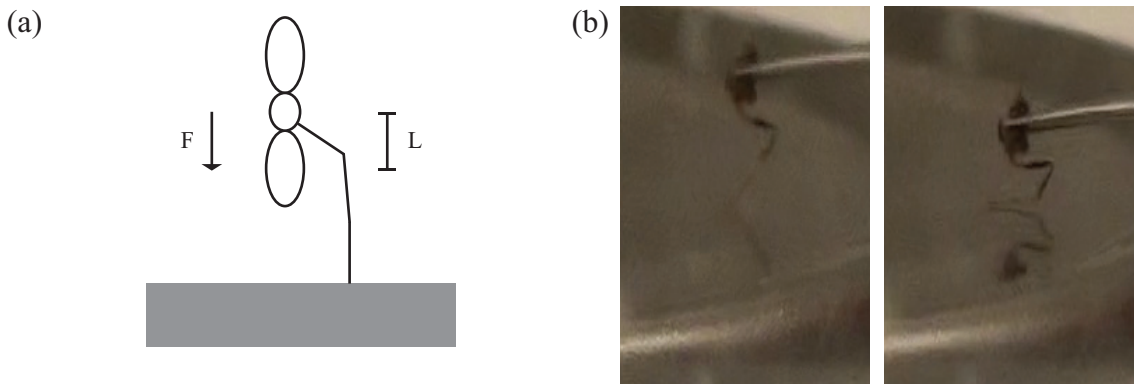

Figure 5.7: (a) Schematic of the work measurement to move one limb of an ant a distance $L = 1\ mm$. (b) Images of an ant limb before being moved and after being moved a distance L. Force was measured by analytical balance.

5.4 SAOS Comparisons

Theoretical work has been done to model the behavior of an ant aggregation by using an active rearrangeable network as the model [229]. The model treats the ants as a disordered network with dynamic bonds that attach actively and detach after a force dependent time [230]. They are able to capture the scaling of the viscosity with shear rate in terms of these active attachment/detachments. However, the scaling of the viscosity with shear rate is the same for live and dead ants and so not dependent on activity.

We can further show that this scaling is not dependent on activity by using frequency sweeps from Chapter 3 to calculate a viscosity for an active system. The Cox-Merz rule, originally written down to describe polymer rheology, which gives an empirical connection between the magnitude of the complex viscosity found from oscillatory experiments and the viscosity as a function of shear rate, $\eta(\dot{\gamma}) = |\eta^*(\omega)|$ [184, 194, 231, 232]. The complex viscosity is found from, $|\eta^*| = |G^*|/\omega$ [184].

In Chapter 3 we found that the aggregation follows the Kramers-Kronig relation [194, 203] and that when active $G' = G'' \sim \omega^{1/2}$ and when inactive $G' > G''$ with essentially no frequency dependence. We then find that $|\eta^*(\omega)| \sim \omega^{-1/2}$ and $|\eta^*(\omega)| \sim \omega^{-1}$, for active and inactive aggregations, respectively. We can then use the Cox-Merz rule to compare a controlled shear rate test, and the magnitude of the complex viscosity calculated from oscillatory measurements for dead, live but inactive, and live and active aggregations. Since we are mainly concerned with the scaling we have normalized each data set so that $\sigma_c/100$ is 1, Fig. 5.8. We see that the results from the controlled shear rate test agree between the dead, and the live but inactive aggregations and the expected scaling of $\dot{\gamma}^{-1}$. In the live and active aggregation the scaling is closer to $\dot{\gamma}^{-1/2}$. This suggests that the controlled shear rate experiments are not affected by activity since live, active ants measured in oscillation shear thin less than live, active ants under rotation.

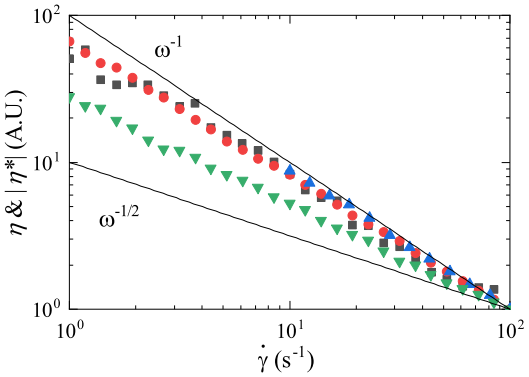

Figure 5.8: η and $|\eta^*|$ normalized to the value at $100\ s^{-1}$. The black squares are a controlled shear rate experiment starting at high $\dot{\gamma}$. The rest are viscosities calculated from oscillatory experiments using the Cox-Merz rule. The red circles are from an experiment with dead ants and the green up triangles are from an inactive live aggregation. The blue down triangles are for an active live aggregation. The range of $\dot{\gamma}$ was chosen from oscillatory experiments with active live aggregation. All experiment were done at $\phi_{eff} = 1.1$.

5.5 Conclusions

Under a constant applied shear rate, ant aggregations shear thin. In particular the viscosity goes as $\eta(\dot{\gamma}) = \sigma_c \dot{\gamma}^{-1}$ with $\sigma_c = 100\ Pa$. This behavior is not dependent on activity. From creep experiments in Chapter 4 we saw that $100\ Pa$ was the lowest applied stress for which aggregations flowed like a simple liquid, and that below that value the aggregations are able to resist the applied stress intermittently. This transition stress is the same as σ_c when the ants are forced to flow. The viscosities found from creep experiments where a strain rate can be defined follow the same scaling as those from controlled shear rate experiments. We attribute the viscous behavior largely to the friction in the ants limbs themselves, which are required to give way for the aggregation to shear thin. We also compared viscosities found from oscillatory rheology and found that while inactive and dead aggregations share the $\dot{\gamma}^{-1}$ scaling, active aggregations do not, confirming that activity is not important .

CHAPTER 6

LARGE AMPLITUDE OSCILLATORY SHEAR

In this chapter we will examine the nonlinear behavior of ant aggregations subjected to oscillatory shear strains. We do this experimentally by performing the same experiment as was discussed in Chapter 3 but increasing the strain amplitude beyond the linear regime. This type of experiment was shown in Fig. 3.2, and was used as a way of finding the linear regime. A similar experiment is shown here in Fig. 6.1 (a), along with strain amplitude sweeps for dead ants, Fig. 6.1 (c), and for live aggregations at high effective volume fraction, Fig. 6.1 (d). What we see from all of them is intercycle shear thinning and strain softening, as both the storage and loss modulus go down with increasing strain amplitude. The noisy region at the smallest strain amplitudes at $\phi_{eff} = 1.1$ is mainly due to the changing activity of the ants which is clearly detected in the normal force, Fig. 6.1 (b). The torque is just above the limit of what we can measure, $30\ \mu Nm$ at the lowest strain amplitude. The other thing to note is that all of the live aggregations exhibit separation of the moduli with increasing strain amplitude. $G'' > G'$ at the largest strain amplitudes. This separation moves to higher strain amplitudes with increasing effective volume fraction indicating that larger motions are needed to fluidize the aggregation at higher densities.

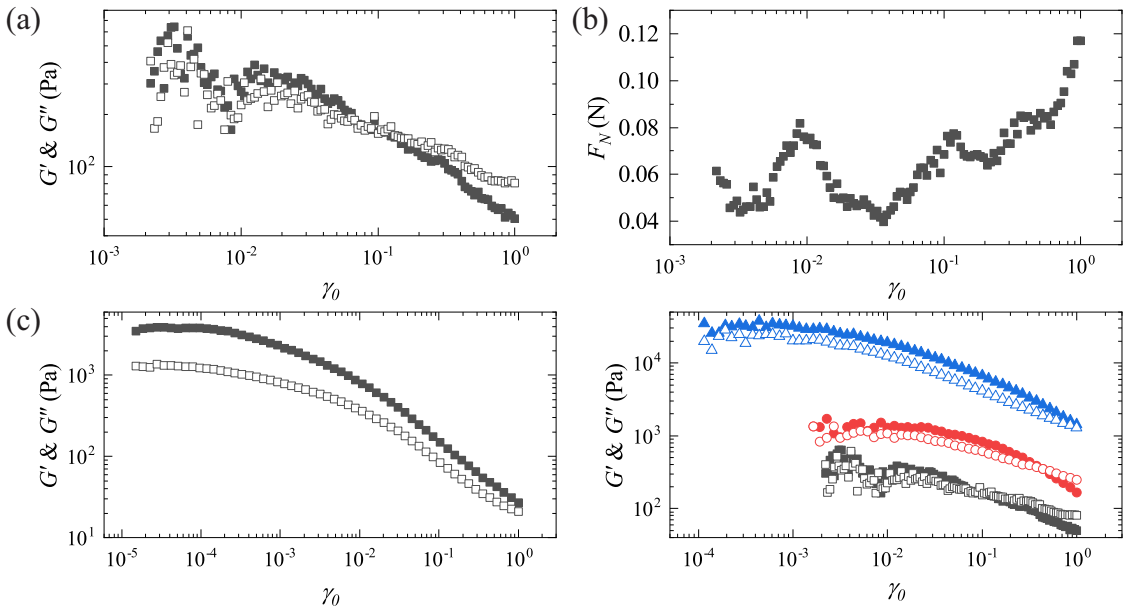

Figure 6.1: (a) Strain sweep with increasing strain amplitude of live ants at an effective volume fraction of 1.1. (b) Normal force data from the strain sweep in (a). (c) Strain sweep with increasing strain amplitude of dead ants at an effective volume fraction of 1.1. (d) Strain sweeps with increasing strain amplitude of live ants at effective volume fractions of $\phi_{eff} = 1.1$ (black squares), 2.2 (red circles) and 3.3 (blue triangles). Closed symbols represent G', open symbols represent G''. All strain sweeps were performed at $\omega = 1\ rad/s$.

The storage and loss modulus have physical meaning the linear regime as both the applied strain and the resultant stress are single sinusoids albeit out of phase. Beyond the linear regime these moduli are no longer as meaningful as they obscure some of the nuance of the nonlinear regime since G' and G'' are found from fitting to a single sinusoid. For large strain amplitudes the applied strain is by construction a single sinusoidal but the resultant stress is not, see Fig. 2.9 (a) for an example. To understand the behavior outside the linear regime we need to go beyond G' and G''. We will use the framework laid out by Ewoldt et al.[189] (see Chapter 2.2.5). This framework draws a distinction between intercycle and intracycle behavior. Intercycle behavior compare the moduli at different applied strain amplitudes whereas intracycle behavior gives information about the response within one oscillation.

6.1 Preliminary: Nonlinear Rheology of Emulsions

Consider an emulsion of oil and water stabilized with an amphiphilic block copolymer, poly(ethylene oxide)-block-poly(ϵ-caprolactone) (PEO-b-PCL) and lecithin [233]. This system is of interest in the food and drug industries since it is stable and biocompatible. With this emulsion we can make both an attractive and a repulsive emulsion by changing the surfactant (e.g. adding lecithin) in the system or changing the volume fraction such that short range interactions become relevant[234–237]. The storage and loss modulus are shown for an attractive and a repulsive emulsion in Fig. 6.2 (a) and (d), respectively. Attractive emulsions form a colloidal gel of drops whereas repulsive emulsions are a colloidal fluid up to random close pack. We can see that the attractive emulsion has a crossover from being mostly solid like at lower stains to being predominantly viscous at high strain amplitudes. The repulsive emulsion is predominantly viscous through the entire range of strain amplitude. Both intercycle strain soften and shear thin as the moduli all decrease with increasing strain amplitude.

To investigate the nonlinear behavior more correctly we now use a sum of sines or a sum of Chebyshev functions, Eq. 2.14, instead of describing the stress with a single sinusoid. Fitting to a sum of sines is done on the waveforms and fitting to Chebyshev functions is done of the in-phase or out-of-phase component of the stress, Eq. 2.14 and the two sets of coefficients are inter related by Eq. 2.16. In practice this is done by taking a Fast Fourier Transform (FFT) of the stress waveform which gives the weights of the sine fit and from there calculating the Fourier or Chebyshev coefficients. Fast Fourier Transforms are a class of algorithms that compute the Fourier transform of a discrete set of points in $\mathcal{O}(n \log n)$, whereas computing the Fourier transform directly takes a prohibitively long amount of time as it is $\mathcal{O}(n^2)$, where n is the number of points. The rheometer records 257 points for each waveform, with the last point overlapping the first. This means that there are 256 points in a full cycle, with each time step being taking the same amount of time. The number of

points is also a power of 2 which is convenient but not required for the FFT algorithm. It also sets the maximum number of modes that we can use as 128 via the Nyquist frequency, $\omega_{Nyquist} \sim N/2$ [189], though in practice we will never need this many. Firstly, because we only care about odd modes because the stress is assumed to be odd [189, 194] and secondly the first few modes contribute the most to the shape; the majority of experiments are captured using the first two odd modes only. We use the first 11 odd modes out of a possible 64 modes to determine the nonlinear moduli and to calculate the Chebyshev coefficients.

We can then use the ratio of the third mode coefficient to the first mode coefficient as a measure of the level of nonlinearity at a particular strain amplitude. This is shown for the emulsions in Fig. 6.2 (b,e). For the attractive emulsions, the level of elastic nonlinearity, e_3/e_1, drops below zero indicating intracycle strain softening just beyond the linear regime where $\gamma_0 = 0.01$, Fig. 6.2 (b). At $\gamma_0 = 0.1$, e_3/e_1 again crosses zero and the system begins to intracycle strain stiffen. The level of viscous nonlinearity does the opposite, starting out shear thickening and then transitioning to shear thinning. In contrast, the repulsive emulsion never has a crossover, the elastic nonlinearity intracycle strain stiffens and the viscous nonlinearity shear thins, Fig. 6.2 (e).

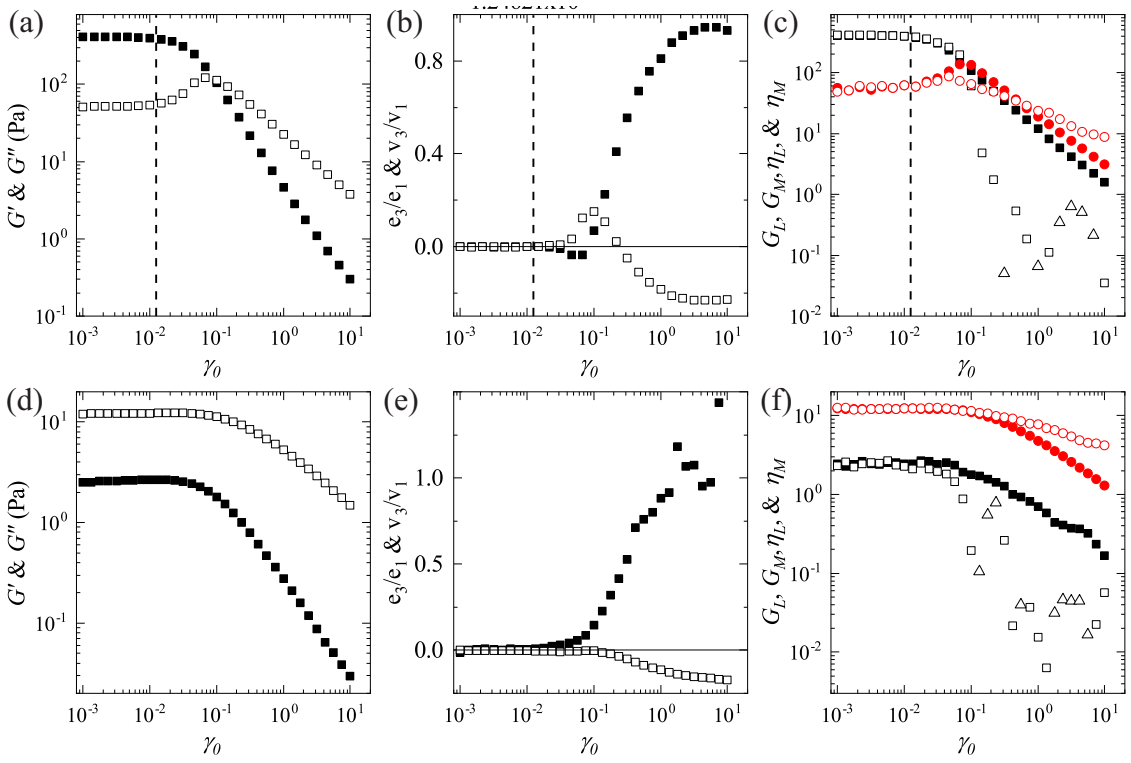

Figure 6.2: (a-c) Nonlinear oscillatory measurements of an attractive emulsion. (a) G' (closed symbols) and G'' (open symbols) as a function of strain amplitude. (b) The level of nonlinearity, e_3/e_1 (closed symbols) and v_3/v_1 (open symbols), as a function of strain amplitude. (c) Nonlinear moduli: η'_L (closed red circles), η'_M (open red circles), G'_L (solid black squares), and G'_M (open black squares are positive and open black triangles are negative), plotted versus strain amplitude. (d-f) Nonlinear oscillatory measurements of a repulsive emulsion. (d) Storage and loss moduli as a function of strain amplitude. (e) The level of nonlinearity, e_3/e_1 and v_3/v_1 as a function of strain amplitude. (f) Nonlinear moduli: η'_L (closed red circles), η'_M (open red circles), G'_L (solid black squares), and G'_M (open black squares are positive and open black triangles are negative), plotted versus strain amplitude.

Beyond the level of nonlinearity we can also look at the nonlinear moduli: the large strain elastic modulus, G'_L; the minimum strain elastic modulus, G'_M; the large strain rate viscous modulus, η'_L; and the minimum strain rate viscous modulus, η'_M; which we can calculate from the fitting using Eqs. 2.17, 2.19, and 2.20. The minimum strain elastic modulus gives information about the situation at small strain, while the large strain elastic modulus gives information about the situation at large strain. The viscous moduli give the same information but for small and large shear rates. For the attractive emulsion, just outside of the linear regime there is a region where $G'_M > G'_L$ indicating that the greatest

stress increase happens at small strains, Fig. 6.2 (c). As the strain amplitude is increased the contribution to the stress at large strains become more important, $G'_M < G'_L$. This distinction is lost when looking only at G' since it is always between G'_L and G'_M.

Another interesting feature of the nonlinear moduli is the moduli are not required to be positive. If this happens it is more likely to be in the minimum strain moduli, G'_M, since $G'_M \sim e_1 - 3e_3$ whereas $G'_L \sim e_1 + e_3$. The same is true for the minimum shear rate moduli, η'_M, and for a corresponding reason. This means that the slope of the in-phase stress can be zero or negative around $\gamma = 0$. This also appears as a self intersection in the out-of-phase Lissajous curve. A negative modulus indicates that the material is removing stress faster than it is accumulating it. This is a steady state effect and would not appear on the first oscillation. Negative moduli happen in both the attractive and repulsive emulsion at higher strain amplitudes, represented by the open black triangles in Fig. 6.2 (c,f). We have taken the absolute value of the moduli so that they are visible in a log scale plot. A representative point, $\gamma_0 = 0.133$ with a negative modulus is shown in Fig. 6.3. The slight negative slope can be seen in the elastic Lissajous curve around $\gamma = 0$ and the self intersection can be seen at the lowest shear rate, Fig. 6.3 (a,b). The mode weights are shown in Fig. 6.3 (c) where we can see that the first few modes contribute the most and that they are both positive and negative.

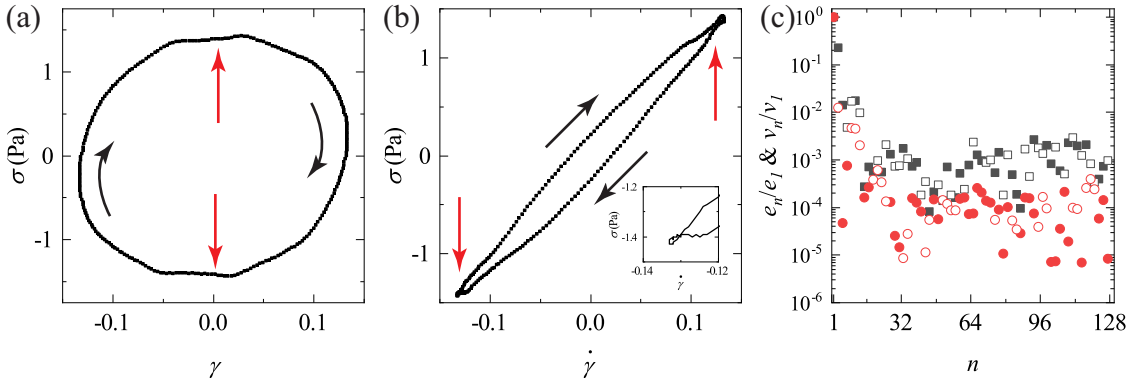

Figure 6.3: Oscillatory measurement of a repulsive emulsion at $\gamma_0 = 0.133$. (a) Stress vs strain Lissajous curve illustrating a negative G'_M. (b) Stress vs shear rate for the same cycle. The direction of oscillation is indicated with arrows. The inset is close up of the loop in the bottom left of the Lissajous plot. (c) The magnitude of the Chebyshev modes normalized to the first mode. Closed symbols are positive and open symbols are negative.

6.2 Ant Lissajous Reconstructions

We now perform the same analysis for an ant aggregation at $\phi_{eff} = 1.6$ for two representative strains: $\gamma_0 = 0.01$ and $\gamma_0 = 1$. Their waveforms and reconstructions are shown in Fig. 6.4 (a,b,d,e). The absolute value of the relative contributions of each mode number for the stress waveforms are shown in Fig. 6.4 (c,f). The relative weight is found by normalizing with respect to the first mode and the absolute value is used, as the contributions can be negative. This is plotted on a semi-log scale to further emphasize the importance of only the first few modes. From the coefficients we can then calculate the nonlinear moduli as well as the in-phase and out-of-phase stress components, σ' and σ''. The moduli and the stress components are shown in Fig. 6.5, overlaid over the Lissajous curves, for the example waveforms in Fig. 6.4 (a,b,d,e).

We see good agreement between the strain and stress and reconstructions using only the first mode in the linear regime, Fig. 6.4 (a,b), 6.5 (a,b). However, only using a single mode certainly does not fit the stress response outside of the linear regime, Fig. 6.4 (e). Considering the first 11 modes gives a good fit of the stress. There is a slight deviation in the strain at high strain amplitude directly after the system has reached the largest strain, Fig.

6.4 (d). This does not affect the elastic nonlinear moduli, however, since the reconstruction is good at the minimum strain and the maximum strain, Fig. 6.5 (c). It does however affect the viscous nonlinear moduli by overestimating η'_L and underestimating η'_M, Fig. 6.5 (d). This means that at the highest strain amplitudes the value of v_3/v_1 or T is in reality smaller in magnitude than what we find from our fits. The placement of the deviation means that the deviations in strain rate are at the minimum and maximum values while the deviations in strain are between the minimum and maximum, thereby causing a larger effect in T than in S.

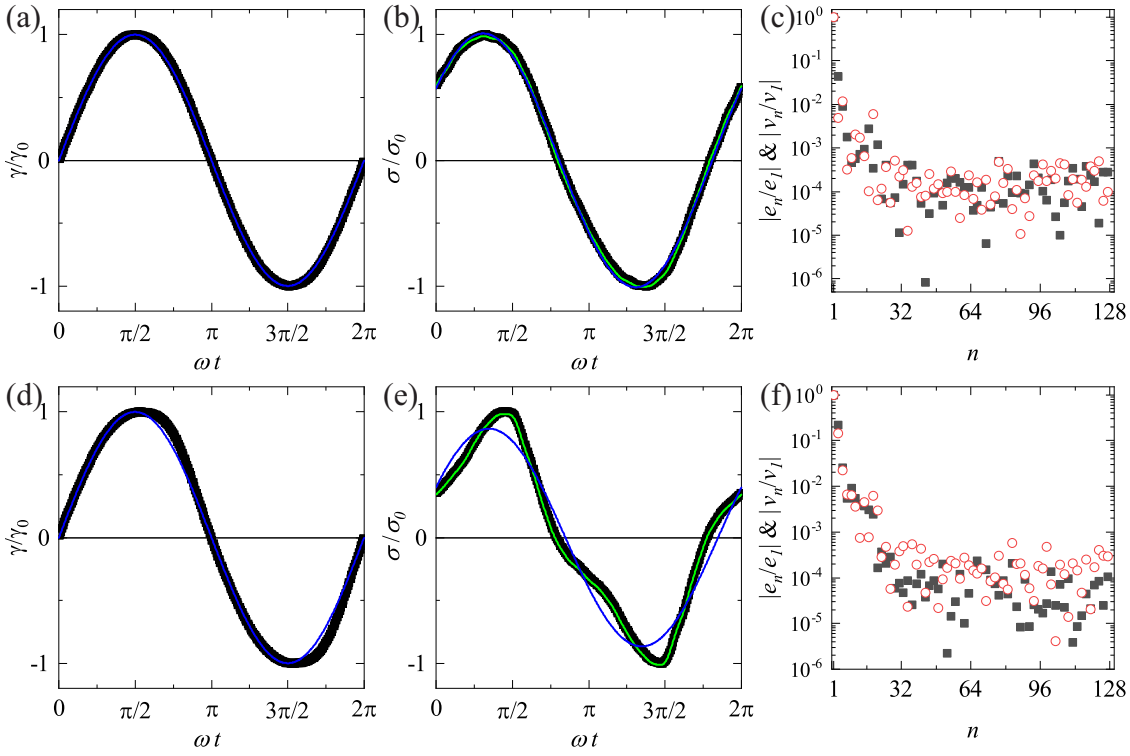

Figure 6.4: (a-c) Oscillatory measurement in the linear regime for a live aggregation at $\phi_{eff} = 1.6$, $\omega = 10\ rad/s$, and $\gamma_0 = 0.01$. (a) Normalized strain vs phase angle. The line is a fit $\gamma = \gamma_0 sin(\omega t)$. (b) Normalized stress vs phase angle for the same measurement. The lines are reconstructions from the first and first 11 Fourier coefficients. (c) The magnitude of the Chebyshev coefficients normalized to the first mode. The black squares are the closed elastic coefficients, e_n/e_1, and the open red circles are the viscous coefficients, v_n/v_1. (d-f) Oscillatory measurement outside the linear regime for a live aggregation at $\phi_{eff} = 1.6$, $\omega = 10\ rad/s$, and $\gamma_0 = 1$. (d) Normalized strain vs phase angle. The line is a fit $\gamma = \gamma_0 sin(\omega t)$. The deviation at high strain does not affect the calculation of nonlinear moduli since only the magnitude of γ_0 is used but it does affect how the viscous Lissajous curve looks. (e) Normalized stress vs phase angle for the same measurement. The line is reconstruction from the first (blue) and first 11 (green) Fourier coefficients. (f) The magnitude of the Chebyshev coefficients normalized to the first mode. The black squares are the closed elastic coefficients, e_n/e_1, and the open red circles are the viscous coefficients, v_n/v_1.

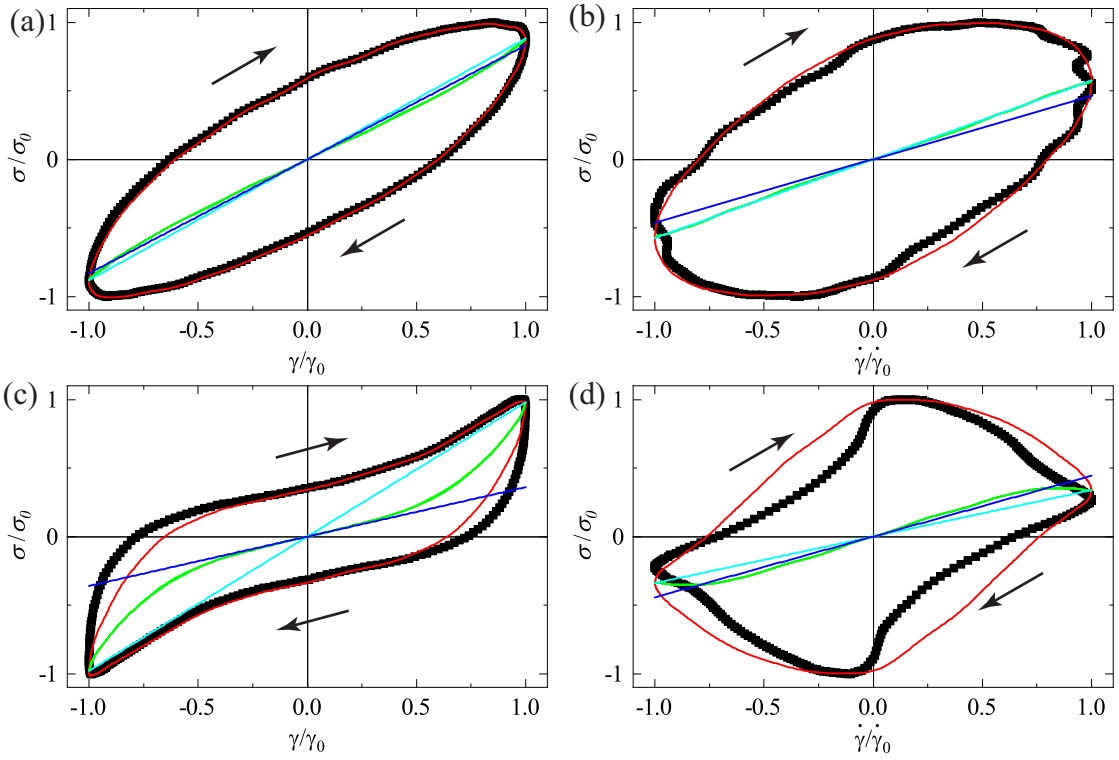

Figure 6.5: (a-b) Lissajous curves for an oscillatory measurement in the linear regime for a live aggregation at $\phi_{eff} = 1.6$, $\omega = 10\ rad/s$, and $\gamma_0 = 0.01$. The waveforms are shown in Fig. 6.4 (a,b). (a) Elastic Lissajous curve (black squares) and reconstruction (red line). σ', G'_L, and G'_M are overlapping lines. (b) Viscous Lissajous curve (black squares) and reconstruction from the first 11 modes (red line) and 1 mode (green line). σ'', η'_L, and η'_M are overlapping lines. (c-d) Lissajous curves for an oscillatory measurement outside the linear regime for a live aggregation at $\phi_{eff} = 1.6$, $\omega = 10\ rad/s$, and $\gamma_0 = 1$. The waveforms are shown in Fig. 6.4 (d,e). (c) Elastic Lissajous curve (black squares) and reconstruction (red line). σ' is the green line, G'_L the cyan, and G'_M is the blue line. (d) Viscous Lissajous curve (black squares) and reconstruction (red line). σ'' is the green line, η'_L is the cyan line, and η'_M is the blue line. The deviations in the strain seen in Fig. 6.4 (d) show up in the elastic Lissajous curve and are pronounced in the viscous Lissajous curve.

6.3 Pipkin Diagram

We can look for the onset of nonlinearity in both strain and frequency by constructing a Pipkin diagram. This type of diagram plots either the level of nonlinearity or the Lissajous-Bowditch plots as a function of both strain amplitude and frequency. The raw data from one set of strain amplitude sweeps at five different frequencies can be seen in Fig. 6.6 (a). Each point has been scaled by its maximum stress and strain. Since the applied strain amplitude

changes by two orders of magnitude from the top of the plot to the bottom this scaling is necessary in order to look at differences in the shape of the Lissajous curves. This data has been reconstructed in Fig. 6.6 (b) using only the first 4 odd modes of the Chebyshev coefficients found from fitting the waveforms. This was done to eliminate the higher order noise that we see at high ω. The noise at the lowest strain at the lowest frequencies comes from being near the torque limit of what we can measure with our modified rheometer setup.

In the reconstructed data it is easier to see the onset of nonlinearity. In the top right of the plot we can see the intracycle strain stiffening, evidenced by the increase of the stress at high strain. We cannot tell anything about the intercycle behavior since each Lissajous-Bowditch plot has been normalized so that all can be seen.

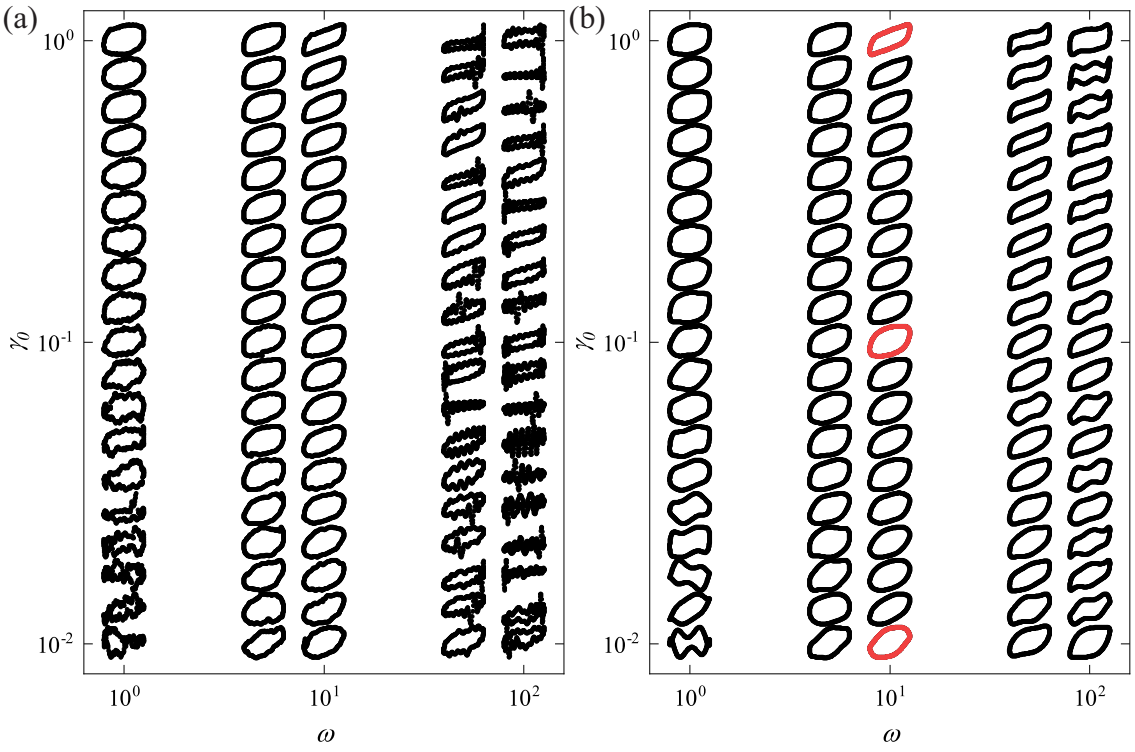

Figure 6.6: (a) Raw Lissajous curves for strain amplitudes from 10^{-2} to 10^0 and frequencies from 10^0 to 10^2. The noise at low strain and frequencies is because of the torque limit of the rheometer. The higher order noise at high frequency is from limitations of the feedback loop in the rheometer. (b) Reconstruction of the raw data in (a) using 4 many modes. The three curves in red are the three points we will focus on in Section. 6.4.

Looking at the Lissajous curves both in the linear and nonlinear regimes gives us several criterion for determining if a point is reasonable and removing the bad ones from the dataset. This allows us to use points that are really close to or at the torque limit of the rheometer and to throw out points that are below the torque limit automatically. From the shape we can determine that the moduli cannot be negative for ant aggregations. This is not to say that it is impossible to have negative nonlinear moduli, a material unloading stress faster than it is accumulating it around $\gamma = 0$ will have a negative G'_M, but in the case of ant aggregations, this is not seen and therefor we can remove any point that has any negative moduli. The most likely to be negative moduli are the minimum strain and strain rate moduli [189].

We also remove points where the level of nonlinearity differs by a large amount depending on how it is calculated. If $|(S/4 - e_3/e_1)| > 1$ or $|(T/4 - v_3/v_1)| > 1$ we remove the point. We can rewrite this inequality using Eq. 2.21 to put the inequality in terms of e_3/e_1 and v_3/v_1:

$$\begin{aligned} \Big|\frac{S}{4} - \frac{e_3}{e_1}\Big| &= \Big|\frac{e_3 + ...}{e_1 + e_3 + ...} - \frac{e_3}{e_1}\Big| > 1 \\ &\approx \Big|\frac{e_3}{e_1 + e_3} - \frac{e_3}{e_1}\Big| = \Big|\frac{e_3^2}{e_1(e_1 + e_3)}\Big| = \Big|\frac{(e_3/e_1)^2}{1 + (e_3/e_1)}\Big| > 1. \end{aligned} \tag{6.1}$$

This inequality then says that we will remove the point if e_3/e_1 and v_3/v_1 lie outside of $\pm(1 + \sqrt{5})/2$, about ± 1.6. This is a reasonable range since at the highest strain amplitude we have explored, $\gamma_0 = 1$, $e_3/e_1 \approx 0.2$ and $v_3/v_1 \approx -0.25$. For example the point in Fig. 6.5 (c,d), which is at $\gamma_0 = 1$, $e_3/e_1 = 0.22$ and $v_3/v_1 \approx -0.15$.

6.3.1 Effects of Activity

We also want to be able to look at the effect the level of activity has of the level of nonlinearity and the nonlinear moduli. We saw in Chapters 3 and 4 that activity affects the mechanics of ant aggregations. there we saw that we could determine the level of activity by looking

at the normal force that the aggregation exerts on the top tool. This was clearly seen in $0\ Pa$ creep experiments and linear oscillatory rheology, both of which showed cyclic peaks in the normal force. An example of such a timesweep is shown in Fig. 6.7. Overlaid on the peaks in the normal force are the cuttoffs used to classify each measurement as either: inactive, active, or transitional points. Active points have high normal force and capture the peaks of activity. Inactive points have low normal force and capture the instance of an aggregation when it is predominantly static and inactive. The middle, transitional, section has intermediate normal force and displays properties between what we have called active and inactive. We will be comparing the active to the inactive case and using the transitional measurements as a buffer to separate the two. The number of points measured at each of the three strains is shown in Table 6.1.

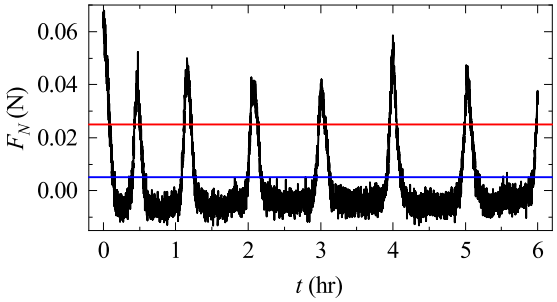

Figure 6.7: Normal force as a function of time illustrating the cyclic changes of the level of activity. The lower blue line is the upper limit of what we are classifying as inactive. The upper red line is the lower limit of what we are classifying as active.

Table 6.1: Number of colonies used, number of experiments run, and the number of active and inactive points obtained at each effective volume fraction.

		$\gamma = 0.01$	$\gamma = 0.1$	$\gamma = 1$
$\phi_{eff} = 1.1$	Colonies	5	2	5
	Days	8	3	8
	Active	620	308	2490
	Inactive	703	366	800
$\phi_{eff} = 1.6$	Colonies	2	3	3
	Days measured	2	3	3
	Active	997	1368	756
	Inactive	663	1083	341

6.4 Three Points in the Pipkin Diagram

We are going to focus on three representative points on the Pipkin diagram in order to more closely investigate the nonlinearities and to account for the effects of activity. We pick a frequency of $10\ rad/s$ because there is enough torque to have the full strain amplitude range measurable and strain amplitudes of 0.01, 0.1, and 1 to fully cover the range. Since different days and different colonies yield different moduli, we need to take timesweeps of multiple colonies over multiple days in order to have statistically meaningful results. The number of colonies and days measured for each strain is shown in Table 6.1.

6.4.1 Small Strain Amplitude, $\gamma_0 = 0.01$

At $\gamma_0 = 0.01$ and $\omega = 10\ rad/s$ the aggregation is within the linear regime explored in Chapter 3. In Fig. 6.8 (a) (solid lines) we show the distribution of elastic nonlinearities obtained from active and inactive aggregations, black and red respectively. The level of elastic nonlinearity does not change with activity since both are in the linear regime and as such the level is around zero. The elastic moduli also do not change with activity as seen

in the distributions of G'_L and G'_M in, Fig. 6.8 (b-c). This is not surprising since the elastic moduli did not change significantly at $\omega = 10\ rad/s$ in frequency sweeps done for active and inactive aggregations, Fig. 3.8 (c,d).

The level of viscous nonlinearity again does not change with activity since both are in the linear regime, Fig. 6.8 (d). However, the viscous nonlinear moduli do change with activity; they both increase with activity consistent with frequency sweeps of active and inactive ants in Fig. 3.8 (c,d). Both moduli increase by the same amount,, Fig. 6.8 (e-f), keeping their ratio and hence the level of nonlinearity the same, $v_3/v_1 \sim (\eta'_L - \eta'_M)/\eta'_L$. The viscous moduli are an order of magnitude lower than the elastic moduli since the elastic nonlinear moduli are equal to G' in the linear regime whereas the viscous nonlinear moduli are equal to G''/ω [189]; $\omega = 10\ rad/s$ in the case considered.

Increasing the effective volume fraction to $\phi_{eff} = 1.6$ does not change the level of nonlinearity, either elastic or viscous, significantly, since this strain amplitude is in the linear regime, Fig. 6.8 (a,d) (dashed lines). The distributions are narrower which is seen from a decrease in the standard deviation of the peaks but they are otherwise very similar, Tab. 6.3. The elastic moduli increase with increased ϕ_{eff} as we would expect from what we saw in Chapter 3, Fig. 3.18, since we are within the density region where the moduli are linear with ϕ_{eff}. The viscous moduli also increase when increasing ϕ_{eff}. However the ratio between the active and inactive moduli is smaller, Fig. 6.8 (e,f).

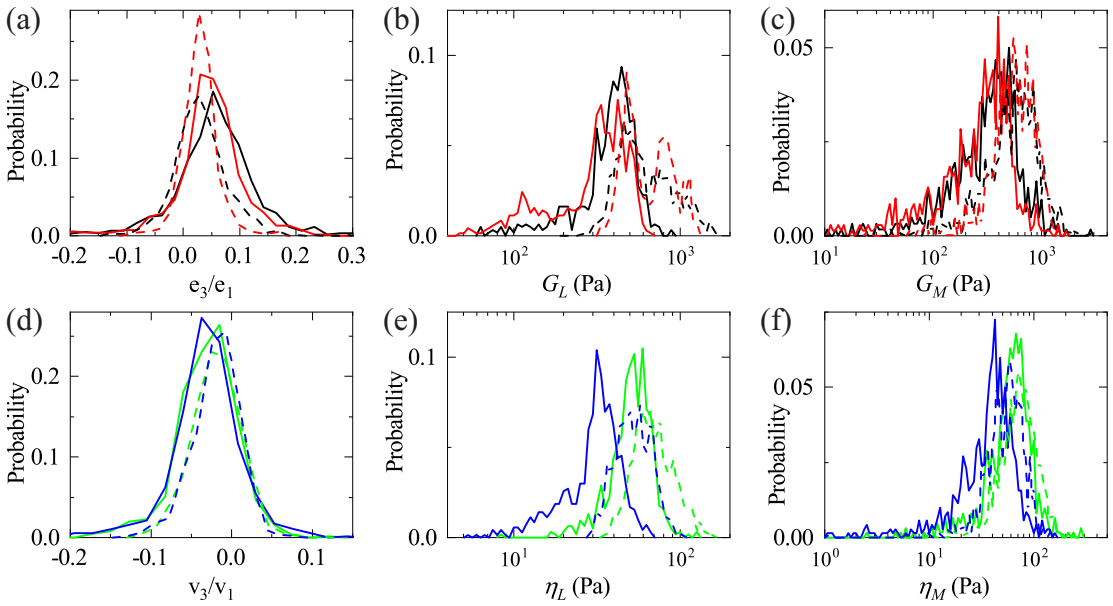

Figure 6.8: (a-f) Distributions of the level of the nonlinearity and the nonlinear moduli for a strain amplitude of $\gamma = 0.01$. Solid lines are at an effective volume fraction of 1.1 and dotted lines are at $\phi_{eff} = 1.6$. Black and green lines are for active aggregations, red and blue lines are for inactive aggregations. Elastic properties are shown in (a-c) with distributions of e_3/e_1 in (a), G'_L in (b), and G'_M in (c). Viscous properties are shown in (d-f) with distributions of v_3/v_1 in (d), η'_L in (e), and η'_M in (f). All distributions have been normalized by the number of points in the distribution. For the number of points in each see Tab. 6.1.

6.4.2 Large Strain Amplitude, $\gamma_0 = 1$

We now move to the largest strain amplitude; at $\gamma_0 = 1$ and $\omega = 10\ rad/s$ the aggregation is now far from the linear regime. The level of elastic nonlinearity is around 0.2 and is unaffected by the level of activity, Fig. 6.9 (a). Positive e_3/e_1 confirms the intracycle strain stiffening behavior of the aggregation seen from the increase of stress at high strain in Lissajous curves, Fig. 6.5 (c), and negative v_3/v_1 confirms the intracycle shear thinning seen from the Lissajous curves in Fig. 6.5 (d). G'_L is larger than G'_M and neither is affected by the level of activity, Fig. 6.9 (b,c). The level of viscous nonlinearity is around -0.25 and is unaffected by activity, Fig. 6.9 (d). η'_M is larger than η'_L and neither is affected by the level of activity, Fig. 6.9 (e,f). At strain amplitudes this high, the forcing effect of the large strain is enough to wash out the affects of activity on the behavior of the system. This

is reminiscent of how dead and live ants flow the same way when forced to flow during a controlled shear rate experiment, Fig. 5.4.

Increasing the effective volume fraction does not change the level of elastic nonlinearity but does change the viscous nonlinearity, Fig. 6.9 (a,d). The value of the elastic moduli both increase with ϕ_{eff}, Fig. 6.9 (b,c). There is an increase in the moduli, Fig. 6.9 (e,f), and a decrease in the level of viscous nonlinearity due to the increased effective volume fraction. There is no effect from activity.

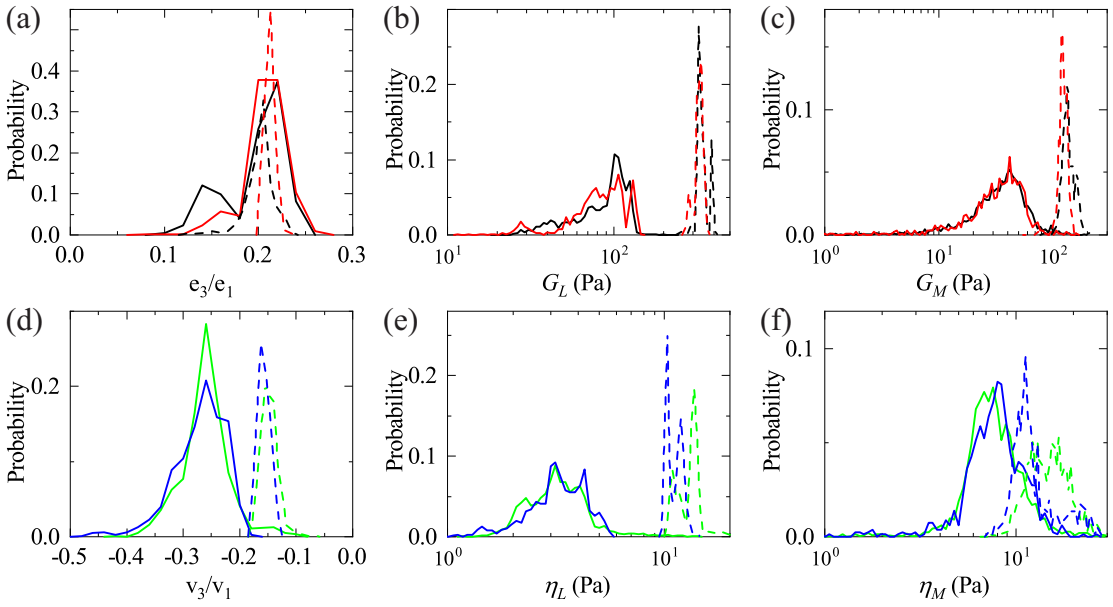

Figure 6.9: (a-f) Distributions of the level of the nonlinearity and the nonlinear moduli for a strain amplitude of $\gamma = 1$. Solid lines are at an effective volume fraction of 1.1 and dotted lines are at $\phi_{eff} = 1.6$. Black and green lines are for active aggregations, red and blue lines are for inactive aggregations. Elastic properties are shown in (a-c) with distributions of e_3/e_1 in (a), G'_L in (b), and G'_M in (c). Viscous properties are shown in (d-f) with distributions of v_3/v_1 in (d), η'_L in (e), and η'_M in (f). All distributions have been normalized by the number of points in the distribution. For the number of points in each see Tab. 6.1.

6.4.3 Medium Strain Amplitude, $\gamma_0 = 0.1$

At $\gamma_0 = 0.1$ and $\omega = 10\ rad/s$ the aggregation is not in the linear regime but not at high enough γ_0 to wash out the effects of activity. The level of elastic nonlinearity is always positive, Fig. 6.10 (a) unlike for $\gamma_0 = 0.01$ which has a similar peak location but a much

wider distribution. It also does not change with activity. In addition, G'_L is larger than G'_M and neither change with activity, Fig. 6.10 (b,c).

The level of viscous nonlinearity is always negative, however, it does change with activity/ Increasing activity decreases the level of viscous nonlinearity, Fig. 6.10 (d). Activity increases the nonlinear viscous moduli, but it increases the large strain rate modulus by a larger amount thereby decreasing the level of nonlinearity, Fig. 6.10 (e,f). The viscous moduli are again about an order of magnitude lower than the elastic moduli.

Increasing the effective volume fraction does not change the elastic level of nonlinearity but the moduli increase some, Fig. 6.10 (a-c). This is unsurprising since we had previously seen that $G' \sim \phi_{eff}$ in this range of ϕ_{eff}. Again, activity has no effect. For the viscous component, increasing the effective volume fraction decreases the level of nonlinearity and increases the moduli, Fig. 6.10 (e-f). At the higher effective volume fraction active aggregations are less nonlinear and have larger viscous moduli than inactive aggregations. This indicates that there are two ways of decreasing the level of viscous nonlinearity: increasing the effective volume fraction and increasing the level of activity. These two mechanisms contribute in the same direction but not equal. Changing the level of activity has a smaller effect at higher effective volume fraction, though it has an effect at the two effective volume fractions we have worked with.

We can attribute both of these effects to the same underlying cause. Vernerey et al. proposed that in a transient network the mechanics would be dependent on the rate of attachment and detachment in the system[229, 230, 238]. From the elastic behavior, we see that the network is essentially unchanged by activity. Since the network does not change with activity or with time this means that the rate of linking and unlinking must be similar. What can change then is the number of linking/unlinking events. Increasing this number increases the dissipation. From this standpoint, increasing the activity and increasing ϕ_{eff} both increase the number of linking/unlinking events, hence decreasing the level of viscous nonlinearity and increasing the viscous moduli. At much higher effective volume fractions,

we would expect the affect of activity to disappear and to see no difference between active and inactive aggregations, since in this case there would no longer be space to be active (see Chapter 3, Fig, 3.18).

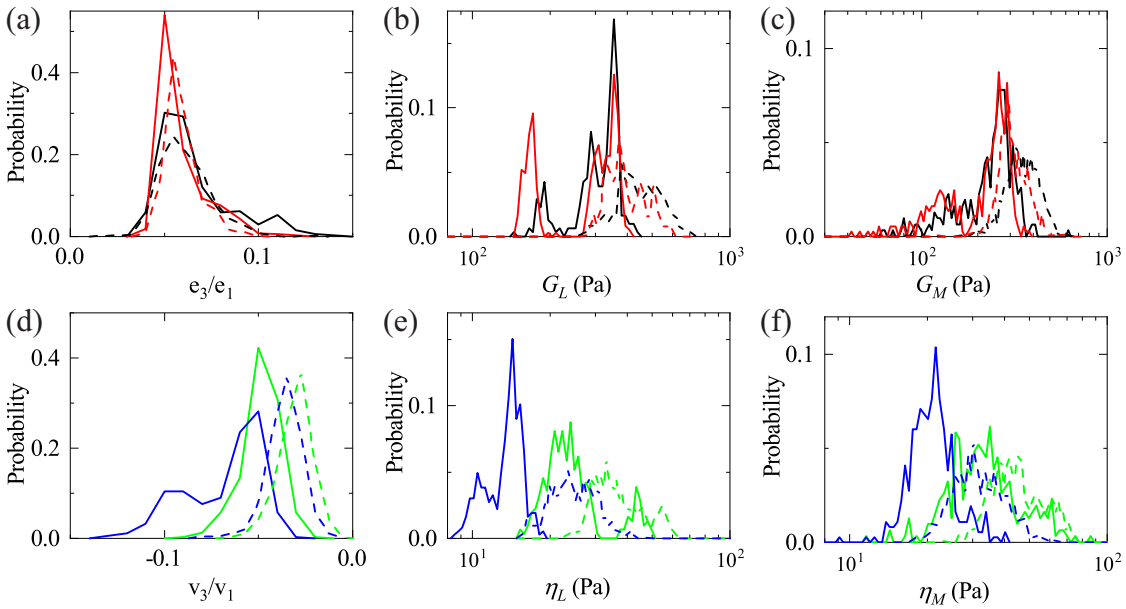

Figure 6.10: (a-f) Distributions of the level of the nonlinearity and the nonlinear moduli for a strain amplitude of $\gamma = 0.1$. Solid lines are at an effective volume fraction of 1.1 and dotted lines are at $\phi_{eff} = 1.6$. Black and green lines are for active aggregations, red and blue lines are for inactive aggregations. Elastic properties are shown in (a-c) with distributions of e_3/e_1 in (a), G'_L in (b), and G'_M in (c). Viscous properties are shown in (d-f) with distributions of v_3/v_1 in (d), η'_L in (e), and η'_M in (f). All distributions have been normalized by the number of points in the distribution. For the number of points in each see Tab. 6.1.

6.5 Effects of Strain Amplitude and Volume Fraction

Now we can combine data for different γ_0 to address what is happening intercycle when changing the applied strain amplitude and the effective volume fraction. At low strain amplitudes the levels of both elastic and viscous nonlinearity are around zero though the mean elastic nonlinearity is slightly positive and the mean viscous nonlinearity is slightly negative, Fig. 6.11 (a). As the strain amplitude is increased the elastic nonlinearity has a similar mean but a smaller standard deviation indicating that at this strain it is always positive. The mean of the viscous nonlinearity remains comparable to the low strain amplitude value but

it is always negative. There is also an effect of activity with increasing activity decreasing the level of nonlinearity. At $\gamma_0 = 1$ the aggregation intracycle strain stiffens, seen from the positive e_3/e_1, and intracycle shear thins, seen from the negative v_3/v_1, Fig. 6.11 (a). Activity does not play a significant role in either nonlinearity.

Increasing the effective volume fraction does not change the level of elastic nonlinearity at any strain amplitude. The viscous nonlinearity decreases with increased ϕ_{eff} and this change is larger at larger strain, Fig. 6.11 (a). There is a change in the viscous nonlinearity with activity at $\gamma_0 = 0.1$ but the effect is small compared to lower ϕ_{eff}.

While the system intracycle shear thins and strain stiffens we can now also look at the intercycle behavior. Ant aggregations intercycle strain soften which is seen from the decreasing magnitude of the elastic moduli in Fig. 6.11 (b). They intercycle shear thin, seen from the decreasing magnitude of the viscous moduli, Fig. 6.11 (c). These are consistent with strain amplitude sweeps that just show the storage and loss modulus as in Fig. 6.1. However, the description in terms of G'_L, G'_M, η'_L, and η'_M is more strictly correct, since in the nonlinear rheology, the stress cannot be described with a single harmonic. Both effects are less pronounced with increasing effective volume fraction.

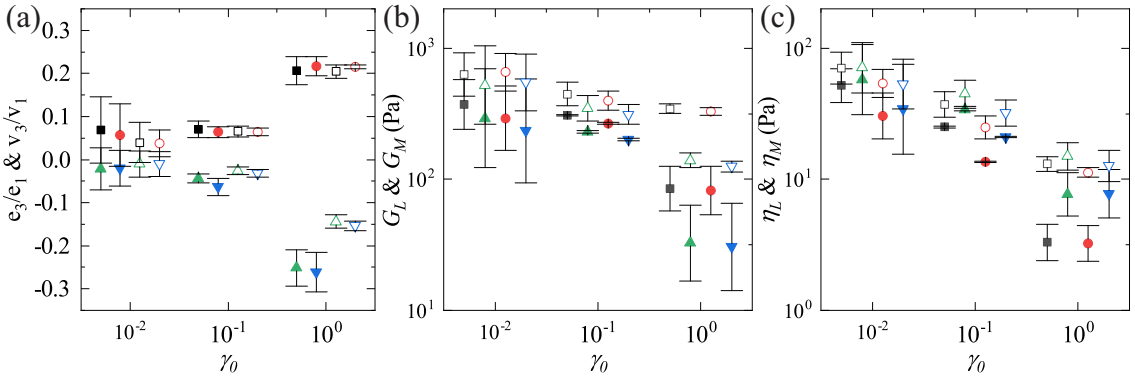

Figure 6.11: Nonlinear moduli and the level of nonlinearity for ant aggregations at $\phi_{eff} = 1.1$ (closed symbols) and $\phi_{eff} = 1.6$ (open symbols). (a) e_3/e_1 for active ants (black squares), e_3/e_1 for inactive ants (red circles), v_3/v_1 for active ants (green up triangles), v_3/v_1 for inactive ants (blue down triangles). (b) G'_L for active ants (black squares), G'_L for inactive ants (red circles), G'_M for active ants (green up triangles), G'_M for inactive ants (blue down triangles). (c) η'_L for active ants (black squares), η'_L for inactive ants (red circles), η'_M for active ants (green up triangles), η'_M for inactive ants (blue down triangles). The exact values from these plots are in Tables 6.2 and 6.3.

Table 6.2: Mean and standard deviation for the distributions of the log of the nonlinear moduli.

			$\gamma = 0.01$		$\gamma = 0.1$		$\gamma = 1$	
			Mean	SD	Mean	SD	Mean	SD
$\phi_{eff} = 1.1$	G'_L	Active	2.57	0.19	2.49	0.10	1.93	0.17
		Inactive	2.47	0.24	2.43	0.15	1.91	0.18
	G'_M	Active	2.46	0.38	2.36	0.16	1.51	0.29
		Inactive	2.37	0.40	2.30	0.19	1.48	0.33
	η'_L	Active	1.72	0.13	1.40	0.12	0.52	0.14
		Inactive	1.48	0.18	1.13	0.07	0.51	0.14
	η'_M	Active	1.76	0.27	1.53	0.14	0.89	0.17
		Inactive	1.54	0.34	1.32	0.10	0.89	0.18
$\phi_{eff} = 1.6$	G'_L	Active	2.80	0.16	2.65	0.09	2.54	0.04
		Inactive	2.82	0.14	2.60	0.07	2.52	0.03
	G'_M	Active	2.72	0.30	2.54	0.10	2.14	0.06
		Inactive	2.74	0.22	2.49	0.08	2.10	0.04
	η'_L	Active	1.85	0.12	1.57	0.10	1.12	0.06
		Inactive	1.73	0.11	1.40	0.09	1.05	0.04
	η'_M	Active	1.85	0.19	1.65	0.10	1.17	0.11
		Inactive	1.73	0.19	1.51	0.10	1.10	0.12

Table 6.3: Mean and standard deviation for the distributions of the level of nonlinearity.

			$\gamma = 0.01$		$\gamma = 0.1$		$\gamma = 1$	
			Mean	SD	Mean	SD	Mean	SD
$\phi_{eff} = 1.1$	e_3/e_1	Active	0.069	0.077	0.071	0.020	0.207	0.032
		Inactive	0.057	0.073	0.064	0.013	0.217	0.022
	v_3/v_1	Active	-0.022	0.049	-0.044	0.010	-0.251	0.042
		Inactive	-0.020	0.042	-0.064	0.020	-0.261	0.046
$\phi_{eff} = 1.6$	e_3/e_1	Active	0.040	0.047	0.066	0.013	0.205	0.016
		Inactive	0.038	0.031	0.064	0.009	0.216	0.004
	v_3/v_1	Active	-0.010	0.030	-0.026	0.009	-0.144	0.015
		Inactive	-0.010	0.029	-0.032	0.009	-0.153	0.011

6.6 Conclusions

Ant aggregations intercycle strain soften and shear thin with increasing strain amplitude. Within one cycle however, at higher strain amplitudes they strain stiffen and shear thin. The level of viscous nonlinearity indicates an intracycle shear thinning, that decreases with increasing activity and effective volume fraction. The level of elastic nonlinearity indicates an the intracycle strain stiffening, that does not depend on either activity or effective volume fraction. The nonlinear moduli, however, are affected by ϕ_{eff}, as we would expect from looking at the behavior of the linear moduli in Chapter 3.

The dissipation rate and hence the viscous nature of the aggregation is affected by the number of linking and unlinking events that take place inside the system. This increases with activity and with effective volume fraction. Having more different modes of relaxation available lowers the level of viscous nonlinearity.

The level of elastic nonlinearity is based on the overall structure of the network which does not seem to change likely due to the rates of linking and unlinking between the ants

being comparable. Neither activity nor effective volume fraction within the range probed affects the level of elastic nonlinearity.

REFERENCES

[1] David K Campbell. “Nonlinear physics: Fresh breather”. In: *Nature* 432.7016 (2004), p. 455.

[2] Thomas A Witten and Philip A Pincus. *Structured fluids*. OUP, 2010. ISBN: 019958382X.

[3] Rk Pathria and PD Beale. *Statistical Mechanics Third Edition*. Oxford, UK: Elsevier, 2011.

[4] Christopher Battle et al. “Broken detailed balance at mesoscopic scales in active biological systems”. In: *Science* 352.6285 (2016), pp. 604–607.

[5] Pablo G Debenedetti and Frank H Stillinger. “Supercooled liquids and the glass transition”. In: *Nature* 410.6825 (2001), p. 259.

[6] Johan Mattsson. “The Glass Transition”. In: *Fluids, Colloids and Soft Materials: An Introduction to Soft Matter Physics* (2016), pp. 249–278.

[7] Michael Rubinstein and RH Colby. *Polymer Physics*. Oxford, 2003.

[8] Peter N Pusey and W Van Megen. “Phase behaviour of concentrated suspensions of nearly hard colloidal spheres”. In: *Nature* 320.6060 (1986), p. 340.

[9] Gary L Hunter and Eric R Weeks. “The physics of the colloidal glass transition”. In: *Reports on Progress in Physics* 75.6 (2012), p. 066501.

[10] PN Pusey. “The effect of polydispersity on the crystallization of hard spherical colloids”. In: *Journal de physique* 48.5 (1987), pp. 709–712.

[11] See-Eng Phan et al. “Effects of polydispersity on hard sphere crystals”. In: *The Journal of chemical physics* 108.23 (1998), pp. 9789–9795.

[12] Paul M Chaikin, Tom C Lubensky, and Thomas A Witten. *Principles of condensed matter physics*. Vol. 1. Cambridge university press Cambridge, 1995.

[13] Gerold Adam and Julian H Gibbs. “On the temperature dependence of cooperative relaxation properties in glass-forming liquids”. In: *The journal of chemical physics* 43.1 (1965), pp. 139–146.

[14] Heinrich M Jaeger, Sidney R Nagel, and Robert P Behringer. “Granular solids, liquids, and gases”. In: *Reviews of modern physics* 68.4 (1996), p. 1259.

[15] Bruno Andreotti, Yoel Forterre, and Olivier Pouliquen. *Granular media: between fluid and solid*. Cambridge University Press, 2013. ISBN: 1107034795.

[16] P. G. de Gennes. “Granular matter: a tentative view”. In: *Reviews of Modern Physics* 71.2 (1999), S374–S382.

[17] Scott V. Franklin. “Extensional rheology of entangled granular materials”. In: *EPL (Europhysics Letters)* 106.5 (2014), p. 58004.

[18] G D’anna et al. “Observing brownian motion in vibration-fluidized granular matter”. In: *Nature* 424.6951 (2003), p. 909.

[19] ML Hunt et al. “Effects of horizontal vibration on hopper flows of granular materials”. In: *Physics of fluids* 11.1 (1999), pp. 68–75.

[20] G Junot et al. “Active versus Passive Hard Disks against a Membrane: Mechanical Pressure and Instability”. In: *Physical review letters* 119.2 (2017), p. 028002.

[21] G Marty and Olivier Dauchot. “Subdiffusion and cage effect in a sheared granular material”. In: *Physical review letters* 94.1 (2005), p. 015701.

[22] Pedro M Reis, Rohit A Ingale, and Mark D Shattuck. “Crystallization of a quasi-two-dimensional granular fluid”. In: *Physical review letters* 96.25 (2006), p. 258001.

[23] Klebert Feitosa and Narayanan Menon. “Fluidized granular medium as an instance of the fluctuation theorem”. In: *Physical review letters* 92.16 (2004), p. 164301.

[24] LG Gibilaro et al. “On the apparent viscosity of a fluidized bed”. In: *Chemical engineering science* 62.1-2 (2007), pp. 294–300.

[25] Francois Boyer, Elisabeth Guazzelli, and Olivier Pouliquen. “Unifying suspension and granular rheology”. In: *Physical Review Letters* 107.18 (2011), p. 188301.

[26] S Mori and CY Wen. “Estimation of bubble diameter in gaseous fluidized beds”. In: *AIChE Journal* 21.1 (1975), pp. 109–115.

[27] Raj P Chhabra. *Bubbles, drops, and particles in non-Newtonian fluids*. CRC press, 2006. ISBN: 1420015389.

[28] Nick Gravish et al. “Entangled Granular Media”. In: *Physical Review Letters* 108.20 (2012).

[29] Nick Gravish and Daniel I Goldman. “Entangled Granular Media”. In: *Fluids, Colloids and Soft Materials: An Introduction to Soft Matter Physics* (2016), pp. 341–354.

[30] Julien Deseigne, Olivier Dauchot, and Hugues Chate. “Collective motion of vibrated polar disks”. In: *Physical review letters* 105.9 (2010), p. 098001.

[31] Vijay Narayan, Sriram Ramaswamy, and Narayanan Menon. “Long-lived giant number fluctuations in a swarming granular nematic”. In: *Science* 317.5834 (2007), pp. 105–108.

[32] Antoine Bricard et al. “Emergent vortices in populations of colloidal rollers”. In: *Nature communications* 6 (2015), p. 7470.

[33] Antoine Bricard et al. “Emergence of macroscopic directed motion in populations of motile colloids”. In: *Nature* 503.7474 (2013), p. 95.

[34] J. Palacci et al. “Living crystals of light-activated colloidal surfers”. In: *Science* 339.6122 (2013), pp. 936–40.

[35] Richard P. Wool. “Self-healing materials: a review”. In: *Soft Matter* 4.3 (2008), p. 400.

[36] Yan Huang et al. “A self-healable and highly stretchable supercapacitor based on a dual crosslinked polyelectrolyte”. In: *Nature Communications* 6 (2015), 10310–.

[37] R. S. Trask, H. R. Williams, and I. P. Bond. “Self-healing polymer composites: mimicking nature to enhance performance”. In: *Bioinspir Biomim* 2.1 (2007), P1–9.

[38] S. Phonekeo et al. “Ant aggregations self-heal to compensate for the Ringelmann effect”. In: *Soft Matter* 12.18 (2016), pp. 4214–20.

[39] Simon Garnier. “From ants to robots and back: how robotics can contribute to the study of collective animal behavior”. In: *Bio-Inspired Self-Organizing Robotic Systems*. Springer, 2011, pp. 105–120. ISBN: 3642207596.

[40] M. Moussaid et al. “Collective Information Processing and Pattern Formation in Swarms, Flocks, and Crowds”. In: *Topics in Cognitive Science* 1.3 (2009), pp. 469–497.

[41] Michael Rubenstein, Alejandro Cornejo, and Radhika Nagpal. “Programmable self-assembly in a thousand-robot swarm”. In: *Science* 345.6198 (2014), pp. 795–799.

[42] Dhananjay T Tambe et al. “Collective cell guidance by cooperative intercellular forces”. In: *Nature materials* 10.6 (2011), p. 469.

[43] R Di Leonardo et al. “Bacterial ratchet motors”. In: *Proceedings of the National Academy of Sciences* 107.21 (2010), pp. 9541–9545.

[44] Guillaume Duclos et al. “Topological defects in confined populations of spindle-shaped cells”. In: *Nature Physics* 13.1 (2017), p. 58.

[45] He-Peng Zhang et al. “Collective motion and density fluctuations in bacterial colonies”. In: *Proceedings of the National Academy of Sciences* 107.31 (2010), pp. 13626–13630.

[46] M. Moussaid et al. “Experimental study of the behavioural mechanisms underlying self-organization in human crowds”. In: *Proceedings of the Royal Society B-Biological Sciences* 276.1668 (2009), pp. 2755–2762.

[47] M. Moussaid et al. “The walking behaviour of pedestrian social groups and its impact on crowd dynamics”. In: *PLoS One* 5.4 (2010), e10047.

[48] Jesse L. Silverberg et al. “Collective Motion of Humans in Mosh and Circle Pits at Heavy Metal Concerts”. In: *Physical Review Letters* 110.22 (2013).

[49] J. Toner and Y. Tu. “Long-Range Order in a Two-Dimensional Dynamical XY Model: How Birds Fly Together”. In: *Phys Rev Lett* 75.23 (1995), pp. 4326–4329.

[50] Tamas Vicsek et al. “Novel Type of Phase Transition in a System of Self-Driven Particles”. In: *Physical Review Letters* 75.6 (1995), pp. 1226–1229.

[51] Igor S Aranson. “Active colloids”. In: *Physics-Uspekhi* 56.1 (2013), p. 79.

[52] Jonathan R Howse et al. “Self-motile colloidal particles: from directed propulsion to random walk”. In: *Physical review letters* 99.4 (2007), p. 048102.

[53] Walter F Paxton et al. “Catalytically induced electrokinetics for motors and micropumps”. In: *Journal of the American Chemical Society* 128.46 (2006), pp. 14881–14888.

[54] Sumit Gangwal et al. “Induced-charge electrophoresis of metallodielectric particles”. In: *Physical review letters* 100.5 (2008), p. 058302.

[55] L. Giomi, N. Hawley-Weld, and L. Mahadevan. “Swarming, swirling and stasis in sequestered bristle-bots”. In: *Proceedings of the Royal Society a-Mathematical Physical and Engineering Sciences* 469.2151 (2013), p. 18.

[56] Daniel L. Blair, T. Neicu, and A. Kudrolli. “Vortices in vibrated granular rods”. In: *Physical Review E* 67.3 (2003), p. 031303.

[57] Tim Sanchez et al. “Spontaneous motion in hierarchically assembled active matter”. In: *Nature* 491.7424 (2012), pp. 431–434.

[58] Thomas E Angelini et al. “Glass-like dynamics of collective cell migration”. In: *Proceedings of the National Academy of Sciences* 108.12 (2011), pp. 4714–9.

[59] Simon Garcia et al. “Physics of active jamming during collective cellular motion in a monolayer”. In: *Proceedings of the National Academy of Sciences (PNAS)* 112.50 (2015), 15314–15319.

[60] Ben Fabry et al. “Scaling the Microrheology of Living Cells”. In: *Physical Review Letters* 87.14 (2001), p. 148102.

[61] J. Toner and Y. H. Tu. “Flocks, herds, and schools: A quantitative theory of flocking”. In: *Physical Review E* 58.4 (1998), pp. 4828–4858.

[62] A. Cavagna et al. “Scale-free correlations in starling flocks”. In: *Proc Natl Acad Sci U S A* 107.26 (2010), pp. 11865–70.

[63] A. Cavagna et al. “Short-range interactions versus long-range correlations in bird flocks”. In: *Phys Rev E Stat Nonlin Soft Matter Phys* 92.1-1 (2015), p. 012705.

[64] M. Ballerini et al. “Interaction ruling animal collective behavior depends on topological rather than metric distance: Evidence from a field study”. In: *Proceedings of the National Academy of Sciences of the United States of America* 105.4 (2008), pp. 1232–1237.

[65] J Scott Turner. “Termites as models of swarm cognition”. In: *Swarm Intelligence* 5.1 (2011), pp. 19–43.

[66] Orit Peleg et al. “Collective mechanical adaptation of honeybee swarms”. In: *bioRxiv* (2017), p. 188953.

[67] M. Tennenbaum et al. “Mechanics of fire ant aggregations”. In: *Nature Materials* 15.1 (2016), pp. 54–9.

[68] Michael Tennenbaum and Alberto Fernandez-Nieves. “Activity-driven changes in the mechanical properties of fire ant aggregations”. In: *Physical Review E* 96.5 (2017), p. 052601.

[69] John Toner, Yuhai Tu, and Sriram Ramaswamy. “Hydrodynamics and phases of flocks”. In: *Annals of Physics* 318.1 (2005), pp. 170–244.

[70] Tamas Vicsek and Anna Zafeiris. “Collective motion”. In: *Physics Reports* 517.3-4 (2012), pp. 71–140.

[71] M. C. Marchetti et al. “Hydrodynamics of soft active matter”. In: *Reviews of Modern Physics* 85.3 (2013), pp. 1143–1189.

[72] David Saintillan and Michael J Shelley. “Instabilities and pattern formation in active particle suspensions: kinetic theory and continuum simulations”. In: *Physical Review Letters* 100.17 (2008), p. 178103.

[73] John Michael Kosterlitz and David James Thouless. “Ordering, metastability and phase transitions in two-dimensional systems”. In: *Journal of Physics C: Solid State Physics* 6.7 (1973), p. 1181.

[74] Maria R D’Orsogna et al. “Self-propelled particles with soft-core interactions: patterns, stability, and collapse”. In: *Physical review letters* 96.10 (2006), p. 104302.

[75] Jose A Carrillo et al. “Particle, kinetic, and hydrodynamic models of swarming”. In: *Mathematical modeling of collective behavior in socio-economic and life sciences*. Springer, 2010, pp. 297–336.

[76] Iain D Couzin et al. “Collective memory and spatial sorting in animal groups”. In: *Journal of theoretical biology* 218.1 (2002), pp. 1–11.

[77] SC Takatori, W Yan, and JF Brady. “Swim Pressure: Stress Generation in Active Matter”. In: *Physical review letters* 113.2 (2014), p. 028103.

[78] S. C. Takatori and J. F. Brady. “Swim stress, motion, and deformation of active matter: effect of an external field”. In: *Soft Matter* 10.47 (2014), pp. 9433–9445.

[79] Sho C. Takatori and John F. Brady. “A theory for the phase behavior of mixtures of active particles”. In: *Soft matter* 11.40 (2015), pp. 7920–31.

[80] S. C. Takatori and J. F. Brady. “Towards a thermodynamics of active matter”. In: *Physical Review E* 91.3 (2015), p. 7.

[81] A. P. Solon et al. “Pressure is not a state function for generic active fluids”. In: *Nature Physics* 11.8 (2015), 673–678.

[82] Felix Ginot et al. “Nonequilibrium Equation of State in Suspensions of Active Colloids”. In: *Physical Review X* 5.1 (2015).

[83] Jim C Chen and Albert S Kim. “Brownian dynamics, molecular dynamics, and Monte Carlo modeling of colloidal systems”. In: *Advances in colloid and interface science* 112.1-3 (2004), pp. 159–173.

[84] Vishwajeet Mehandia and Prabhu R Nott. “The collective dynamics of self-propelled particles”. In: *Journal of Fluid Mechanics* 595 (2008), pp. 239–264.

[85] Gabriel S. Redner, Aparna Baskaran, and Michael F. Hagan. “Reentrant phase behavior in active colloids with attraction”. In: *Physical Review E* 88.1 (2013).

[86] Gabriel S Redner, Michael F Hagan, and Aparna Baskaran. “Structure and dynamics of a phase-separating active colloidal fluid”. In: *Physical review letters* 110.5 (2013), p. 055701.

[87] A. Wysocki, R. G. Winkler, and G. Gompper. “Cooperative motion of active Brownian spheres in three-dimensional dense suspensions”. In: *Epl* 105.4 (2014), p. 6.

[88] A. P. Solon, M. E. Cates, and J. Tailleur. “Active brownian particles and run-and-tumble particles: A comparative study”. In: *European Physical Journal-Special Topics* 224.7 (2015), pp. 1231–1262.

[89] J. Stenhammar et al. “Phase behaviour of active Brownian particles: the role of dimensionality”. In: *Soft Matter* 10.10 (2014), pp. 1489–99.

[90] C. C. Huang et al. “Thermostat for nonequilibrium multiparticle-collision-dynamics simulations”. In: *Physical Review E* 91.1 (2015), p. 11.

[91] Yaouen Fily and M Cristina Marchetti. “Athermal phase separation of self-propelled particles with no alignment”. In: *Physical review letters* 108.23 (2012), p. 235702.

[92] Guillaume Gregoire and Hugues Chate. “Onset of collective and cohesive motion”. In: *Physical review letters* 92.2 (2004), p. 025702.

[93] Hugues Chate et al. “Collective motion of self-propelled particles interacting without cohesion”. In: *Physical Review E* 77.4 (2008), p. 046113.

[94] Michael E Cates and Julien Tailleur. “Motility-induced phase separation”. In: *Annu. Rev. Condens. Matter Phys.* 6.1 (2015), pp. 219–244.

[95] J. Barre et al. “Motility-Induced Phase Separation of Active Particles in the Presence of Velocity Alignment”. In: *Journal of Statistical Physics* 158.3 (2015), pp. 589–600.

[96] Yaouen Fily, Silke Henkes, and M Cristina Marchetti. “Freezing and phase separation of self-propelled disks”. In: *Soft matter* 10.13 (2014), pp. 2132–2140.

[97] Andras Czirok, H Eugene Stanley, and Tamas Vicsek. “Spontaneously ordered motion of self-propelled particles”. In: *Journal of Physics A: Mathematical and General* 30.5 (1997), p. 1375.

[98] Matthew Spellings et al. “Shape control and compartmentalization in active colloidal cells”. In: *Proceedings of the National Academy of Sciences* 112.34 (2015), E4642–E4650.

[99] Clemens Bechinger et al. “Active particles in complex and crowded environments”. In: *Reviews of Modern Physics* 88.4 (2016), p. 045006.

[100] Jing Yan, Sung Chul Bae, and Steve Granick. “Rotating crystals of magnetic Janus colloids”. In: *Soft Matter* 11.1 (2015), pp. 147–153.

[101] Ambarish Ghosh and Peer Fischer. “Controlled propulsion of artificial magnetic nanostructured propellers”. In: *Nano letters* 9.6 (2009), pp. 2243–2245.

[102] Wei Gao et al. “Highly efficient catalytic microengines: template electrosynthesis of polyaniline/platinum microtubes”. In: *Journal of the American Chemical Society* 133.31 (2011), pp. 11862–11864.

[103] Ivo Buttinoni et al. “Dynamical clustering and phase separation in suspensions of self-propelled colloidal particles”. In: *Physical review letters* 110.23 (2013), p. 238301.

[104] Sambeeta Das et al. “Boundaries can steer active Janus spheres”. In: *Nature Communications* 6 (2015), 8999–.

[105] Jeremie Palacci et al. “Sedimentation and effective temperature of active colloidal suspensions”. In: *Physical Review Letters* 105.8 (2010), p. 088304.

[106] Walter F Paxton et al. “Catalytic nanomotors: autonomous movement of striped nanorods”. In: *Journal of the American Chemical Society* 126.41 (2004), pp. 13424–13431.

[107] Remi Dreyfus et al. “Microscopic artificial swimmers”. In: *Nature* 437.7060 (2005), p. 862.

[108] Ivo Buttinoni et al. “Active Brownian motion tunable by light”. In: *Journal of Physics: Condensed Matter* 24.28 (2012), p. 284129.

[109] Manuele Brambilla et al. “Swarm robotics: a review from the swarm engineering perspective”. In: *Swarm Intelligence* 7.1 (2013), pp. 1–41.

[110] G. Briand and O. Dauchot. “Crystallization of Self-Propelled Hard Discs”. In: *Physical Review Letters* 117.9 (2016), p. 098004.

[111] Guillaume Briand, Michael Schindler, and Olivier Dauchot. “Spontaneously Flowing Crystal of Self-Propelled Particles”. In: *Physical review letters* 120.20 (2018), p. 208001.

[112] A. Kudrolli et al. “Swarming and swirling in self-propelled polar granular rods”. In: *Physical Review Letters* 100.5 (2008), p. 4.

[113] J. Werfel, K. Petersen, and R. Nagpal. “Designing collective behavior in a termite-inspired robot construction team”. In: *Science* 343.6172 (2014), pp. 754–8.

[114] Gil Henkin et al. “Tunable dynamics of microtubule-based active isotropic gels”. In: *Phil. Trans. R. Soc. A* 372.2029 (2014), p. 20140142.

[115] Gijsje H. Koenderink et al. “An active biopolymer network controlled by molecular motors”. In: *Proceedings of the National Academy of Sciences* 106.36 (2009), pp. 15192–15197.

[116] Pau Guillamat et al. “Probing the shear viscosity of an active nematic film”. In: *Physical Review E* 94.6 (2016), p. 060602.

[117] Pau Guillamat, Jordi Ignes-Mullol, and Francesc Sagues. “Control of active liquid crystals with a magnetic field”. In: *Proceedings of the National Academy of Sciences* 113.20 (2016), pp. 5498–5502.

[118] Perry W Ellis et al. “Curvature-induced defect unbinding and dynamics in active nematic toroids”. In: *Nature Physics* 14.1 (2018), p. 85.

[119] J. Prost, F. Julicher, and J. F. Joanny. “Active gel physics”. In: *Nature Physics* 11.2 (2015), pp. 111–117.

[120] Samantha Stam et al. “Filament rigidity and connectivity tune the deformation modes of active biopolymer networks”. In: *Proceedings of the National Academy of Sciences* 114.47 (2017), E10037–E10045.

[121] Nitin Kumar et al. “Tunable structure and dynamics of active liquid crystals”. In: *Science Advances* 4.10 (2018).

[122] Sriram Ramaswamy. “The mechanics and statistics of active matter”. In: *Annu. Rev. Condens. Matter Phys.* 1.1 (2010), pp. 323–345.

[123] Knut Drescher et al. “Direct measurement of the flow field around swimming microorganisms”. In: *Physical Review Letters* 105.16 (2010), p. 168101.

[124] Eric Lauga and Thomas R Powers. “The hydrodynamics of swimming microorganisms”. In: *Reports on Progress in Physics* 72.9 (2009), p. 096601.

[125] Willow R. DiLuzio et al. “Escherichia coli swim on the right-hand side”. In: *Nature* 435 (2005), p. 1271.

[126] Linda Turner, William S Ryu, and Howard C Berg. “Real-time imaging of fluorescent flagellar filaments”. In: *Journal of bacteriology* 182.10 (2000), pp. 2793–2801.

[127] Howard C Berg. *Random walks in biology*. Princeton University Press, 1993. ISBN: 0691000646.

[128] Michael Garcia et al. “Random walk of a swimmer in a low-Reynolds-number medium”. In: *Physical Review E* 83.3 (2011), p. 035301.

[129] WCK Poon. “From Clarkia to Escherichia and Janus: The physics of natural and synthetic active colloids”. In: *Proc. Int. Sch. Phys. Enrico Fermi* 184 (2013), pp. 317–386.

[130] Andrey Sokolov et al. “Concentration dependence of the collective dynamics of swimming bacteria”. In: *Physical review letters* 98.15 (2007), p. 158102.

[131] Salima Rafai, Levan Jibuti, and Philippe Peyla. “Effective viscosity of microswimmer suspensions”. In: *Physical Review Letters* 104.9 (2010), p. 098102.

[132] Hector Matias Lopez et al. “Turning bacteria suspensions into superfluids”. In: *Physical review letters* 115.2 (2015), p. 028301.

[133] Shuo Guo et al. “Symmetric shear banding and swarming vortices in bacterial superfluids”. In: *Proceedings of the National Academy of Sciences* 115.28 (2018), pp. 7212–7217.

[134] Xabel Garcia, Salima Rafai, and Philippe Peyla. “Light control of the flow of phototactic microswimmer suspensions”. In: *Physical review letters* 110.13 (2013), p. 138106.

[135] Howard C Berg. “Chemotaxis in bacteria”. In: *Annual review of biophysics and bioengineering* 4.1 (1975), pp. 119–136.

[136] Pramod A. Pullarkat, Pablo A. Fernandez, and Albrecht Ott. “Rheological properties of the Eukaryotic cell cytoskeleton”. In: *Physics Reports* 449.1 (2007), pp. 29–53.

[137] Benedikt Sabass et al. “Force generation by groups of migrating bacteria”. In: *Proceedings of the National Academy of Sciences* 114.28 (2017), pp. 7266–7271.

[138] Chun-Min Lo et al. “Cell Movement Is Guided by the Rigidity of the Substrate”. In: *Biophysical Journal* 79.1 (2000), pp. 144–152.

[139] Sabyasachi Rakshit and Sanjeevi Sivasankar. “Biomechanics of cell adhesion: how force regulates the lifetime of adhesive bonds at the single molecule level”. In: *Physical Chemistry Chemical Physics* 16.6 (2014), pp. 2211–2223.

[140] Sabyasachi Rakshit et al. “Ideal, catch, and slip bonds in cadherin adhesion”. In: *Proceedings of the National Academy of Sciences* 109.46 (2012), pp. 18815–18820.

[141] Stephane Douezan et al. “Spreading dynamics and wetting transition of cellular aggregates”. In: *Proceedings of the National Academy of Sciences* 108.18 (2011), pp. 7315–7320.

[142] Oliver Lieleg et al. “Mechanical robustness of Pseudomonas aeruginosa biofilms”. In: *Soft matter* 7.7 (2011), pp. 3307–3314.

[143] Xavier Trepat et al. “Universal physical responses to stretch in the living cell”. In: *Nature* 447 (2007), p. 592.

[144] K. E. Kasza et al. “The cell as a material”. In: *Curr Opin Cell Biol* 19.1 (2007), pp. 101–7.

[145] D. R. Myers et al. “Single-platelet nanomechanics measured by high-throughput cytometry”. In: *Nature Materials* 16.2 (2017), pp. 230–235.

[146] Xavier Trepat et al. “Physical forces during collective cell migration”. In: *Nature Physics* 5.6 (2009), pp. 426–430.

[147] Kyogo Kawaguchi, Ryoichiro Kageyama, and Masaki Sano. “Topological defects control collective dynamics in neural progenitor cell cultures”. In: *Nature* 545.7654 (2017), p. 327.

[148] Thuan Beng Saw et al. “Topological defects in epithelia govern cell death and extrusion”. In: *Nature* 544.7649 (2017), p. 212.

[149] William Bialek et al. “Statistical mechanics for natural flocks of birds”. In: *Proceedings of the National Academy of Sciences* 109.13 (2012), pp. 4786–4791.

[150] Tiziana Bartolini et al. “Zebrafish response to 3D printed shoals of conspecifics: the effect of body size”. In: *Bioinspiration & biomimetics* 11.2 (2016), p. 026003.

[151] Roger L. Hughes. “The flow Of human crowds”. In: *Annual Review of Fluid Mechanics* 35.1 (2003), pp. 169–182.

[152] Skanda Vivek et al. “Collective behavior and emergent risks in a model of human- and autonomously-driven vehicles”. In: *ArXiv preprint* (2018).

[153] Douglas H. Kelley and Nicholas T. Ouellette. “Emergent dynamics of laboratory insect swarms”. In: *Scientific Reports* 3 (2013), p. 1073.

[154] Sara Bernardi, Annachiara Colombi, and Marco Scianna. “A discrete particle model reproducing collective dynamics of a bee swarm”. In: *Computers in biology and medicine* (2018).

[155] A. M. Reynolds et al. “Displaced honey bees perform optimal scale-free search flights”. In: *Ecology* 88.8 (2007), pp. 1955–61.

[156] A. M. Reynolds et al. “Honeybees perform optimal scale-free searching flights when attempting to locate a food source”. In: *J Exp Biol* 210.Pt 21 (2007), pp. 3763–70.

[157] V Fourcassie, D Coughlin, and JFA Traniello. “Fractal analysis of search behavior in ants”. In: *Naturwissenschaften* 79.2 (1992), pp. 87–89.

[158] Hugo Torres-Contreras and Mauricio Canals. “Effect of Colony, Patch Distance, And Trajectory Sense on Movement Complexity in Foraging Ants”. In: *Journal of Insect Behavior* 23.4 (2010), pp. 319–328.

[159] Edmund R. Hunt et al. “Ants show a leftward turning bias when exploring unknown nest sites”. In: *Biology letters* 10 (2014).

[160] M. Vela-Perez, M. A. Fontelos, and S. Garnier. “From individual to collective dynamics in Argentine ants (Linepithema humile)”. In: *Mathematical Biosciences* 262 (2015), pp. 56–64.

[161] J Aguilar et al. “Collective clog control: Optimizing traffic flow in confined biological and robophysical excavation”. In: *Science* 361.6403 (2018), pp. 672–677.

[162] Deby L. Cassill et al. “Polyphasic Wake/Sleep Episodes in the Fire Ant, Solenopsis Invicta”. In: *Journal of Insect Behavior* 22.4 (2009), pp. 313–323.

[163] Blaine J Cole. “Short-term activity cycles in ants: generation of periodicity by worker interaction”. In: *American Naturalist* (1991), pp. 244–259.

[164] Walter Reinhart Tschinkel. “Sociometry and sociogenesis of colonies of the fire ant Solenopsis invicta during one annual cycle”. In: *Ecological Monographs* 63.4 (1993), pp. 425–457.

[165] Walter Reinhart Tschinkel. *The fire ants*. Harvard University Press, 2006. ISBN: 0674022076.

[166] Bert Holldobler. *The ants*. Harvard University Press, 1990. ISBN: 0674040759.

[167] Theodore Christian Schneirla. *Army ants: a study in social organization*. W. H. Freeman & Co Ltd, 1971, p. 349.

[168] Theodore Christian Schneirla. *A unique case of circular milling in ants, considered in relation to trail following and the general problem of orientation*. Citeseer, 1944.

[169] I. D. Couzin and N. R. Franks. “Self-organized lane formation and optimized traffic flow in army ants”. In: *Proceedings. Biological sciences* 270.1511 (2003), pp. 139–146.

[170] Chris R. Reid et al. “Army ants dynamically adjust living bridges in response to a cost–benefit trade-off”. In: *Proceedings of the National Academy of Sciences (PNAS)* 112.49 (2015), 15113–15118.

[171] N. J. Mlot, C. A. Tovey, and D. L. Hu. “Fire ants self-assemble into waterproof rafts to survive floods”. In: *Proceedings of the National Academy of Sciences* 108.19 (2011), pp. 7669–7673.

[172] N. J. Mlot, C. Tovey, and D. L. Hu. “Dynamics and shape of large fire ant rafts”. In: *Commun Integr Biol* 5.6 (2012), pp. 590–7.

[173] Paul C Foster et al. “Fire ants actively control spacing and orientation within self-assemblages”. In: *The Journal of experimental biology* 217.12 (2014), pp. 2089–2100.

[174] Deby Lee Cassill et al. “What can ants tell us about collective behavior during a natural catastrophe?” In: *Journal of Bioeconomics* (2015).

[175] Sulisay Phonekeo et al. “Fire ants perpetually rebuild sinking towers”. In: *Royal Society open science* 4.7 (2017), p. 170475.

[176] M. S. Ascunce et al. “Global invasion history of the fire ant Solenopsis invicta”. In: *Science* 331.6020 (2011), pp. 1066–8.

[177] Benjamin J Adams, Linda M Hooper-Bùi, and Rachel M Strecker. “Raft formation by the red imported fire ant, Solenopsis invicta”. In: *Journal of Insect Science* 11.1 (2011).

[178] Deby L Cassill and Devon Singh. “Ambidextrous Mandibles in the Fire Ant Solenopsis invicta”. In: *Annals of the Entomological Society of America* 102.4 (2009), pp. 713–716.

[179] T. Nishino, R. Matsui, and K. Nakamae. “Elastic modulus of the crystalline regions of chitin and chitosan”. In: *Journal of Polymer Science Part B-Polymer Physics* 37.11 (1999), pp. 1191–1196.

[180] D. Raabe et al. “Preferred crystallographic texture of alpha-chitin as a microscopic and macroscopic design principle of the exoskeleton of the lobster Homarus americanus”. In: *Acta Biomater* 3.6 (2007), pp. 882–95.

[181] William Alden Banks et al. *Techniques for collecting, rearing, and handling imported fire ants*. Agricultural Research (Southern Region), Science and Education Administration, US Department of Agriculture, 1981.

[182] Hans M Wyss. *Rheology of soft materials*. John Wiley & Sons, Inc.: Hoboken, NJ, USA, 2016.

[183] Ronald G Larson. *The structure and rheology of complex fluids*. Vol. 150. Oxford university press New York, 1999.

[184] C.W. Macosko. *Rheology: principles, measurements, and applications*. VCH, 1994.

[185] Faith A Morrison. *Understanding rheology*. Oxford University Press, 2001. ISBN: 0195141660.

[186] Roger I. Tanner. *Rheology an historical perspective*. Amsterdam New York: Amsterdam New York : Elsevier, 1998.

[187] Kyu Hyun et al. “A review of nonlinear oscillatory shear tests: Analysis and application of large amplitude oscillatory shear (LAOS)”. In: *Progress in Polymer Science* 36.12 (2011), pp. 1697–1753.

[188] P. Sollich et al. “Rheology of soft glassy materials”. In: *Physical Review Letters* 78.10 (1997), pp. 2020–2023.

[189] Randy H Ewoldt, AE Hosoi, and Gareth H McKinley. “New measures for characterizing nonlinear viscoelasticity in large amplitude oscillatory shear”. In: *Journal of Rheology (1978-present)* 52.6 (2008), pp. 1427–1458.

[190] N. Ashwin Bharadwaj and Randy H. Ewoldt. “Single-point parallel disk correction for asymptotically nonlinear oscillatory shear”. In: *Rheologica Acta* 54.3 (2015), pp. 223–233.

[191] R. H. Colby. “Official symbols and nomenclature of The Society of Rheology”. In: *Journal of Rheology* 57.4 (2013), pp. 1047–1055.

[192] J. Lauger, K. Wollny, and S. Huck. “Direct Strain Oscillation: a new oscillatory method enabling measurements at very small shear stresses and strains”. In: *Rheologica Acta* 41.4 (2002), pp. 356–361.

[193] Jorg Lauger and Heiko Stettin. “Differences between stress and strain control in the non-linear behavior of complex fluids”. In: *Rheologica acta* 49.9 (2010), pp. 909–930.

[194] R Byron Bird, Robert C Armstrong, and Ole Hassager. *Dynamics of polymeric liquids. Vol. 1: Fluid mechanics*. 1987. ISBN: 047107375X, 9780471073758.

[195] Eric Lauga, Michael Brenner, and Howard Stone. “Microfluidics: The No-Slip Boundary Condition”. In: *Springer Handbook of Experimental Fluid Mechanics*. Ed. by Cameron Tropea, Alexander L. Yarin, and John F. Foss. Berlin, Heidelberg: Springer Berlin Heidelberg, 2007, pp. 1219–1240. ISBN: 978-3-540-30299-5.

[196] Heinrich M Jaeger and Sidney R Nagel. “Physics of the granular state”. In: *Science* 255.5051 (1992), pp. 1523–1531.

[197] Iain D. Couzin and Jens Krause. “Self-Organization and Collective Behavior in Vertebrates”. In: *Advances in the Study of Behavior*. Vol. Volume 32. Academic Press, 2003, pp. 1–75. ISBN: 0065-3454.

[198] D. J. Sumpter. “The principles of collective animal behaviour”. In: *Philos Trans R Soc Lond B Biol Sci* 361.1465 (2006), pp. 5–22.

[199] Jordi Alcaraz et al. “Microrheology of human lung epithelial cells measured by atomic force microscopy”. In: *Biophysical journal* 84.3 (2003), pp. 2071–2079.

[200] Thomas Gisler and David A Weitz. “Scaling of the microrheology of semidilute F-actin solutions”. In: *Physical review letters* 82.7 (1999), p. 1606.

[201] M. C. Marchetti. “Active matter: Spontaneous flows and self-propelled drops”. In: *Nature* 491.7424 (2012), pp. 340–1.

[202] Rui Zhang et al. “Interplay of structure, elasticity, and dynamics in actin-based nematic materials”. In: *Proceedings of the National Academy of Sciences* 115.2 (2018), E124–E133.

[203] F. Chambon and H. H. Winter. “Linear Viscoelasticity at the Gel Point of a Cross-Linking Pdms with Imbalanced Stoichiometry”. In: *Journal of Rheology* 31.8 (1987), pp. 683–697.

[204] H.A. Kramers. “La diffusion de la lumiere par les atomes”. In: *Atti Cong. Intern. Fisici, (Transactions of Volta Centenary Congress) Como 2: 545–557.* (1927).

[205] R de Kronig. “On the theory of dispersion of x-rays”. In: *JOSA* 12.6 (1926), pp. 547–556.

[206] Michael Stone and Paul Goldbart. *Mathematics for physics: a guided tour for graduate students*. Cambridge University Press, 2009. ISBN: 1139480618.

[207] HC Booij and GPJM Thoone. “Generalization of Kramers-Kronig transforms and some approximations of relations between viscoelastic quantities”. In: *Rheologica Acta* 21.1 (1982), pp. 15–24.

[208] A. H. Krall and D. A. Weitz. “Internal dynamics and elasticity of fractal colloidal gels”. In: *Physical Review Letters* 80.4 (1998), pp. 778–781.

[209] Trevor S. K. Ng and Gareth H. McKinley. “Power law gels at finite strains: The nonlinear rheology of gluten gels”. In: *Journal of Rheology* 52.2 (2008), p. 417.

[210] Veronique Trappe and Peter Sandkuhler. “Colloidal gels—low-density disordered solid-like states”. In: *Current Opinion in Colloid & Interface Science* 8.6 (2004), pp. 494–500.

[211] Horst Henning Winter and Marian Mours. “Rheology of polymers near liquid-solid transitions”. In: *Neutron spin echo spectroscopy viscoelasticity rheology*. Springer, 1997, pp. 165–234. ISBN: 3540627138.

[212] D. Charbonneau, N. Hillis, and A. Dornhaus. “‘Lazy’ in nature: ant colony time budgets show high ‘inactivity’ in the field as well as in the lab”. In: *Insectes Sociaux* 62.1 (2015), pp. 31–35.

[213] Daniel Charbonneau and Anna Dornhaus. “Workers ‘specialized’ on inactivity: Behavioral consistency of inactive workers and their role in task allocation”. In: *Behavioral Ecology and Sociobiology* 69.9 (2015), pp. 1459–1472.

[214] Daria Monaenkova et al. “Behavioral and mechanical determinants of collective subsurface nest excavation”. In: *Journal of Experimental Biology* 218.9 (2015), pp. 1295–1305.

[215] T. Mason, J. Bibette, and D. Weitz. “Elasticity of Compressed Emulsions”. In: *Physical Review Letters* 75.10 (1995), pp. 2051–2054.

[216] V. G. Mir et al. “Direct compression properties of chitin and chitosan”. In: *Eur J Pharm Biopharm* 69.3 (2008), pp. 964–8.

[217] Ludovic Berthier. “Nonequilibrium Glassy Dynamics of Self-Propelled Hard Disks”. In: *Physical Review Letters* 112.22 (2014).

[218] David Gonzalez-Rodriguez et al. “Soft matter models of developing tissues and tumors”. In: *Science* 338.6109 (2012), pp. 910–917.

[219] R. Ni, M. A. Cohen Stuart, and M. Dijkstra. “Pushing the glass transition towards random close packing using self-propelled hard spheres”. In: *Nat Commun* 4 (2013), p. 2704.

[220] Karine Guevorkian et al. “Aspiration of biological viscoelastic drops”. In: *Physical review letters* 104.21 (2010), p. 218101.

[221] D.L. Hu et al. “Entangled active matter: From cells to ants”. In: *The European Physical Journal Special Topics* 225.4 (2016), pp. 629–649.

[222] George Keith Batchelor. *An introduction to fluid dynamics*. Cambridge university press, 2000. ISBN: 0521663962.

[223] Guillaume P. Citerne, Pierre J Carreau, and Michael Moan. “Rheological properties off peanut butter”. In: *Rheologica Acta* 40 (2001), pp. 86–96.

[224] S Yanniotis, S Skaltsi, and S Karaburnioti. “Effect of moisture content on the viscosity of honey at different temperatures”. In: *Journal of Food Engineering* 72.4 (2006), pp. 372–377.

[225] Jeremie Gachelin et al. “Non-Newtonian Viscosity of Escherichia coli Suspensions”. In: *Physical Review Letters* 110.26 (2013).

[226] N. Huang et al. “Flow of Wet Granular Materials”. In: *Physical Review Letters* 94.2 (2005).

[227] Sasha N Zill et al. “Directional specificity and encoding of muscle forces and loads by stick insect tibial campaniform sensilla, including receptors with round cuticular caps”. In: *Arthropod structure & development* 42.6 (2013), pp. 455–467.

[228] A. Lipp, H. Wolf, and F. O. Lehmann. “Walking on inclines: energetics of locomotion in the ant Camponotus”. In: *J Exp Biol* 208.Pt 4 (2005), pp. 707–19.

[229] Franck J Vernerey, Rong Long, and Roberto Brighenti. “A Statistically-Based Continuum Theory for Polymers with Transient Networks”. In: *Journal of the Mechanics and Physics of Solids* (2017).

[230] Franck J Vernerey et al. “How do fire ants control the rheology of their aggregations? A statistical mechanics approach”. In: *Journal of The Royal Society Interface* 15.147 (2018), p. 20180642.

[231] WP Cox and EH Merz. “Correlation of dynamic and steady flow viscosities”. In: *Journal of Polymer Science* 28.118 (1958), pp. 619–622.

[232] T. S. R. Al-Hadithi, H. A. Barnes, and K. Walters. “The relationship between the linear (oscillatory) and nonlinear (steady-state) flow properties of a series of polymer and colloidal systems”. In: *Colloid and Polymer Science* 270.1 (1992), pp. 40–46.

[233] Kyounghee Shin et al. “Structurally Stable Attractive Nanoscale Emulsions with Dipole-Dipole Interaction-Driven Interdrop Percolation”. In: *Chemistry–A European Journal* 23.18 (2017), pp. 4292–4297.

[234] Anand Yethiraj and Alfons van Blaaderen. “A colloidal model system with an interaction tunable from hard sphere to soft and dipolar”. In: *Nature* 421.6922 (2003), p. 513.

[235] Raymond R Dagastine et al. “Dynamic forces between two deformable oil droplets in water”. In: *Science* 313.5784 (2006), pp. 210–213.

[236] Ivane Jorjadze et al. “Attractive emulsion droplets probe the phase diagram of jammed granular matter”. In: *Proceedings of the National Academy of Sciences* 108.11 (2011), pp. 4286–4291.

[237] Bum Jun Park and Eric M Furst. “Attractive interactions between colloids at the oil–water interface”. In: *Soft Matter* 7.17 (2011), pp. 7676–7682.

[238] F. J. Vernerey et al. “Biological active matter aggregates: Inspiration for smart colloidal materials”. In: *Advances in Colloid and Interface Science* 263 (2019), pp. 38–51.

VITA

Michael J. Tennenbaum grew up in Davis, California. He was a part of the third incoming class at the University of California, Merced where he graduated in 2011 with a Bachelors degree in Physics. In 2012 he joined the Georgia Tech School of Physics and in 2013 began working with Dr. Fernandez-Nieves. In addition to working with ants he was also a fellow of the Sam Nunn Security Program looking at the role of science in national security policy.

When not in the lab Michael enjoys working with bicycles. He was president of Starter Bikes, the Georgia Tech bicycle cooperative, and chair of the Bicycle Infrastructure Improvement Committee at Georgia Tech. At time of writing he owns five cycles, totaling six seats and nine wheels.